Mechanical Properties of Materials for Fusion Power Plants

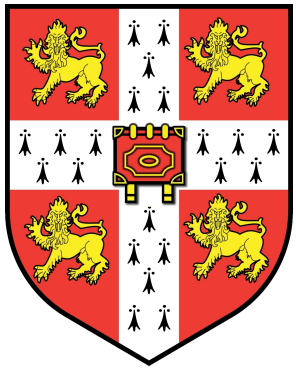

Stéphane Alexis Jacques Forsik

Darwin College, Cambridge

University of Cambridge

A thesis submitted for the degree of

Doctor of Philosophy

May 2009

Preface

This dissertation is submitted for the degree of Doctor of Philosophy at the University of Cambridge. The research described herein was conducted under the supervision of Professor H.K.D.H. Bhadeshia in the Department of Materials Science and Metallurgy, University of Cambridge, between October 2005 and April 2009.

To the best of my knowledge, this work is original, except where suitable references are made to previous work or work done in collaboration. Neither this, nor any substantially similar dissertation, has been submitted for any other degree, diploma, or other qualification at any other university. This dissertation does not exceed 60,000 words in length.

Some of the work described herein has been published:

- S. Forsik and H.K.D.H. Bhadeshia. Elongation of irradiated steels. *Material and Manufacturing Processes*, 24:1–8, 2009.
- H.K.D.H. Bhadeshia, R.C. Dimitriu, S. Forsik, J.H. Pak, and J.H. Ryu. On performance of neural networks in materials science. *Materials Science and Technology*, 25(4):504–510, 2009.

Stéphane Alexis Jacques Forsik
August 10, 2009

Acknowledgements

First of all, I would like to thank my supervisor, Professor Harry Bhadeshia, for welcoming me in his group five years ago when I was still a Master student and for giving me the opportunity to pursue with a Ph.D. His help, guidance and constant enthusiasm have been very much appreciated during the past years.

I am grateful to Professor David J.C. MacKay and Oliver Stegle from the Cavendish Laboratory, University of Cambridge, for useful discussions about Bayesian modelling and Gaussian processes and for providing their computer programs, and to Professor Steve Roberts from the Department of Materials, University of Oxford, for his help and advice.

I am indebted to Richard Kemp, Matthew Peet and Mohamed Sherif from the phase–transformation group who were so helpful at the start of my project. I thank them for their availability, for sharing their experience with MTDATA, neural networks, Model Manager and for their help with all my computer–related problems. I cannot forget all the other members of the group and, in no particular order, I would like to thank Radu, Amir, Saurabh K., Sourabh C., Saurabh D., Jiaven, Gonzalo, Hamilton, Yan Pei, Arijit, Pepe, Luz, Lucia, Hallah, Aseel, Zhu and Mehran as well as all the other present and past members and visiting scientists for making the last three years such an enriching experience. I will certainly miss the endless discussions in the laboratory, the traditionnal coffee and tea breaks, the Friday pub lunch and the group barbecues.

I would also like to express my gratitude to the Engineering and Physical Sciences Research Council for financial support.

My stay in Cambridge would not have been so pleasant without my housemate and travelling buddy Rebecca and my friends Sebastian and Claudia. I would like to have a thought for my other friends and all the

people, students, fellows and academics I have had the chance to meet in Darwin College or in the Darwin College Boat Club.

Pour finir, je souhaiterais remercier ma famille et surtout mes parents, Catherine et Roman, pour leur présence et leur soutien, tant moral que financier, mon frère Christophe pour m'avoir supporté pendant ces 25 dernières années ainsi que Thomas pour ses encouragements et sa patience en toute circonstance.

Abstract

Fusion power is the production of electricity from a hot plasma of deuterium and tritium, reacting to produce α particles and 14 MeV neutrons, which are collected by a cooling system. Their kinetic energy is transformed into heat and electricity via steam turbines. The constant flux of neutrons on the first wall of the reactor produces atomic displacement damage through collisions with nuclei, and gas bubbles as a result of transmutation reactions. This leads eventually to hardening and embrittlement. Designing a material able to withstand such intensity of damage is one of the main aim of research in the field of controlled fusion.

In the past decades, many experiments have been carried out to understand the formation of radiation–induced damage and quantify the changes in mechanical properties of irradiated steels, but the lack of facilities prevents us from testing candidate materials in a fusion–like environment. Modelling techniques are utilised here to extract information and principles which can help estimate changes in steels due to damage.

The elongation and yield strength of various low–activation ferritic/ martensitic steels were modelled by neural networks and Gaussian processes. These models were used to make predictions which were compared to experimental values. Combined with other techniques and thermodynamic tools, it was possible to understand the evolution of the mechanical properties of irradiated steel, with a particular focus on the role of chromium and the roles of irradiation temperature and irradiation dose. They were also used to extrapolate data related to fission and attempt to make predictions in fusion conditions.

A set of general recommendations concerning the database used to train the neural networks were made and the usage of such a modelling technique in materials science is discussed.

An attempt to optimise the performance of neural networks by suppressing some random aspects of the training is presented. Models of the elongation, yield strength and ductile–to–brittle transition temperature trained following this procedure were created and compared to classical models.

Abbreviations

AISI	American Iron and Steel Institute
ANN	Artificial neural network
appm	Atomic parts–per–million
bcc	Body–centred cubic
CTE	Combined test error
DBTT	Ductile–to–brittle transition temperature
DEMO	DEMOnstration power plant
dpa	Displacements–per–atom
EBR	Experimental Breeder Reactor
fcc	Face–centred cubic
GA	Genetic algorithm
Gen. I	First generation of fission reactors
Gen. IV	Fourth generation of fission reactors
GP	Gaussian process
HFIR	High Flux Isotope Reactor
HFR	High Flux Reactor
IFMIF	International Fusion Materials Irradiation Facility
ITER	International Thermonuclear Experimental Reactor
JAEA	Japanese Atomic Energy Agency
JAERI	Japan Atomic Energy Research Institute
JMTR	Japan Materials Test Reactor
JRR	Japanese Research Reactor
KMC	Kinetic Monte Carlo
LAFM	Low–activation ferritic/martensitic
LPE	Logarithmic predictive error
MD	Molecular dynamics
MTData	Metallurgical and Thermochemical Databank

NAg	Numerical Algorithms Group
NN	Neural network
NPL	National Physical Laboratory
ODS	Oxide dispersion strengthened (steel)
ORNL	Oak Ridge National Laboratory
PFM	Plasma–facing material
pka	Primary knock–on atom
RAFM	Reduced–activation ferritic/martensitic
SIA	Self–interstitial atom
SiC	Silicon carbide
SiC_f	Silicon carbide fibre
SGTE	Scientific Group Thermodata Europe
TE	Test error
TRIP	Transformation–induced plasticity
wppm	Weight parts–per–million

Nomenclature

Chapter 2

at%	Atomic percentage
D	Deuterieum
eV	Electron–volt
${}^{Z}_{A}M$	Metallic atom with a mass number Z and an atomic number A
n	Neutron
T	Tritium
wt%	Weight percentage
α	Alpha particle (helium ion)

Chapter 3

C	Covariance function
C_N	Covariance matrix
C_{ij}	Element of matrix C_N
D	Dataset made of input vectors X_N and a corresponding output vector t_N
E_D	Overall error
E_w	Training regulariser
h_i	Hidden unit of the network
l	Model used to obtain the prediction $y^{(l)}$
L	Number of models in the committee
M	Objective function
M_s	Martensite–start temperature
N	Number of inputs
$P(A)$	Prior probability of event A
$P(A\|B)$	Conditional probability (or likelihood) of event A, given event B
$P(A, B)$	Joint probability of event A and B (also written P(A $\cap$ B)
t_N	Output vector $\{t_1, t_2, ..., t_N\}$

$\hat{t}$	Mean value
w_j	Weight j of the network
x_j	Input j of the network
x	Un–normalised value in the database
x_n	Normalised value in the database
x_{max}	Maximum value in the database for the variable x_j
x_{min}	Minimum value in the database for the variable x_j
X_N	Input vector $\{\vec{x}_1, \vec{x}_2, ..., \vec{x}_N\}$
y	Output of the neural network
$y^{(l)}$	Prediction obtained with the model l
$\bar{y}$	Average prediction of a committee of sub–models
Z	Constant
α, β	Control parameters
$\theta, \theta_{(1)}, \theta_{(2)}$	Constant of the network
δ_{ij}	Delta function
μ	Mean value
$\sigma_{\hat{t}}$	Standard deviation
σ_n	Variance of the noise
σ_y	Modelling uncertainty
σ_w	Significance
Θ	Hyperparameter
$\theta, \theta_1, \theta_2$	Constants
θ'_1, θ'_2	Hyperparameters

Chapter 4

k_A, n	Constants
t	Time
T_t	Test temperature
T_{irr}	Irradiation temperature
T_γ	Normalising temperature
T_T	Tempering temperature
t_γ	Normalising time
t_T	Tempering time
V_γ	Volume fraction of retained austenite in cast iron
$\Delta\sigma$	Variation in yield strength
σ	Yield strength

σ'	Transformed yield strength
σ_{min}	Minimum value of the yield strength in the database
σ_{max}	Maximum value of the yield strength in the database

Chapters 6 and **7**

E_{bar}	Average size of error bars
N	Number of predictions
O_i	Calculated value
R_{test}	Root mean square residual (RMS)
T_i	Experimental value
T_{irr}	Irradiation temperature
T_{test}	Test temperature
$\Delta\sigma$	Variation in yield strength
$\sigma_{Carbides}$	Contribution to the yield strength from carbides
$\sigma_{Ferrite}$	Yield strength of pure ferrite
σ_{Irr}	Contribution to the yield strength from radiation–induced hardening
$\sigma_{irradiated}$	Yield strength after irradiation
$\sigma_{unirradiated}$	Yield strength before irradiation
σ_{SS}	Contribution to the yield strength from solid solution strengthening

Contents

Chapter 1

Introduction

The aim of the work presented in this thesis is to continue to explore the possibilities offered by various modelling techniques to understand and calculate the mechanical properties of steels for fusion power plants.

Fusion power is the production of electricity from a plasma of deuterium and tritium and is expected to be one of the major sources of energy in the next 50 to 100 years. However, fusion reactions yield 14 MeV neutrons which represent one of the greatest technical challenges to the success of a fusion power plant. Displaced atoms and gas bubbles induced by irradiation cause hardening and embrittlement of materials in the first wall. Therefore, in the last decades, research has focused on designing an ideal material able to stand such level of damage without jeopardising its engineering properties.

Due to the lack of understanding of hardening and embrittlement mechanisms at high irradiation doses and the lack of facilities, modelling plays a major role here by creating mathematical expressions that can be implemented with little physical knowledge of the system. Neural networks are a popular and well–established method to model complex properties in materials science. They have been used already for irradiated steels and, combined with genetic algorithms, have helped making some guidance for new alloys for fusion power plants.

In this work, general recommendations concerning databases are established and neural–network models of the elongation and yield strength are created

and tested. Gaussian process models are introduced and compared with neural networks. Finally, a method to optimise the training of neural networks is implemented.

Chapter 2 gives an overview of the fusion power and materials involved in the fusion programme, focusing on alloys for the first wall. The basic physics of a fusion reaction and its effects on steel are presented. Candidate alloys developed over the past 30 years are reviewed and their mechanical properties and responses to irradiation outlined.

The theory behind neural networks, the training and the importance of uncertainties, is described in **Chapter 3**. The general usage of neural networks in materials science and the first examples of models of irradiated alloys are reviewed. The theory of Gaussian process modelling is also presented.

Chapter 4 details the databases utilised for the models presented in this thesis. The principal differences with previous effort are explained and a set of recommendations are established.

In **Chapters 5** and **6**, various models of the elongation and the yield strength of irradiated steels steels are created. They are combined with thermodynamic tools and other modelling techniques to discuss some aspects of the mechanical properties of irradiated steels. Predictions and extrapolations are carried out and commented on. For the yield strength, the Gaussian process and neural–network methods are compared.

An optimised method for training neural networks is experienced in **Chapter 7**. Models of the elongation, the yield strength and the ductile–to–brittle transition temperature are designed with the main objective of improving their performance and reducing modelling uncertainties in extrapolation mode.

Finally, **Chapter 8** contains the overall summary of the work and establishes the future axis of research.

Chapter 2

Fusion power and materials – literature survey

Fusion power plants are a potential replacement for fission power and a promising clean source of energy for the "near future" but the design of a commercial fusion reactor represents a great scientific, technical and industrial challenge. Levels of irradiation reached in plasma–facing materials (PFM) designed to absorb heat and provide neutron shielding will be a lot more intense than those reached during fission. Materials directly exposed to radiation will therefore be expected to undergo dramatic modifications of their mechanical properties, in addition to becoming radioactive through transmutation. Because the replacement of irradiated components would be expensive and time consuming, the ideal material should be able to meet the design life of 20 years under severe operating conditions.

Several materials, such as steel, vanadium alloys and silicon carbide fibre–reinforced silicon carbide (SiC_f/SiC) composites have been considered candidates and tested; so–called low–activation ferritic/martensitic steels (LAFM), developed since the 1970s, are in the most advanced stage. They are able to resist high levels of irradiation, and are considered the best candidates for fusion power.

Steels in fission reactors typically experience a dose of 20 displacements–per–atom (dpa) but levels of damage will be as high as 200 dpa in a fusion reactor [1]. This will cause modifications of the microstructure and production of gas via transmutation. Such harsh conditions will only be achieved

experimentally in three prototype facilities to be constructed in the near future: the International Fusion Materials Irradiation Facility (IFMIF), the International Thermonuclear Experimental Reactor (ITER), currently being built, and the DEMOnstration reactor (DEMO) whose realisation will depend on results provided by the IFMIF and ITER. The time scale for these experiments is in the range 15–30 years ahead.

This literature survey describes the basics of fusion energy and the effects of irradiation on metals. It reviews alloys likely to be chosen for fusion power plants and briefly presents current problems and future materials.

2.1 Plasma and fusion energy

Nuclear power plants are nowadays a reliable source of electricity. They are all based on fission reactions and the technology is well advanced. Fusion power is expected to be a promising replacement source of energy in the future but the technology to sustain a reaction has not yet been mastered and the deployment of fusion power is not expected before 2050 [2]. The theoretical basis for a fusion reaction was originally postulated in the 1920s and the first Tokamak, a machine confining a plasma using a toroidal magnetic field, was realised in the 1950s by Kurchatov [3]. Since then, research into controlled fusion has been continuously carried out but the longest burns in experimental reactors only lasted for a couple of seconds, whereas a full–scale commercial reactor would have to sustain the plasma for much longer periods. Large–scale international research programmes such as the IFMIF, ITER (Figure 2.1) and DEMO aim at proving the scientific and technological feasibility and the economic viability of fusion energy [4].

One major concern about fusion remains the production of radioactive waste through activation of structural components and the severe life conditions of materials exposed directly to the plasma: high temperature (peak operating temperatures range from room temperature to 500–700°C), high radiation flux (the high–energy neutron wall loading is expected to be around 1 MW m^{-2} [5]) and high displacement damage over the life of the reactor (200 dpa) [6].

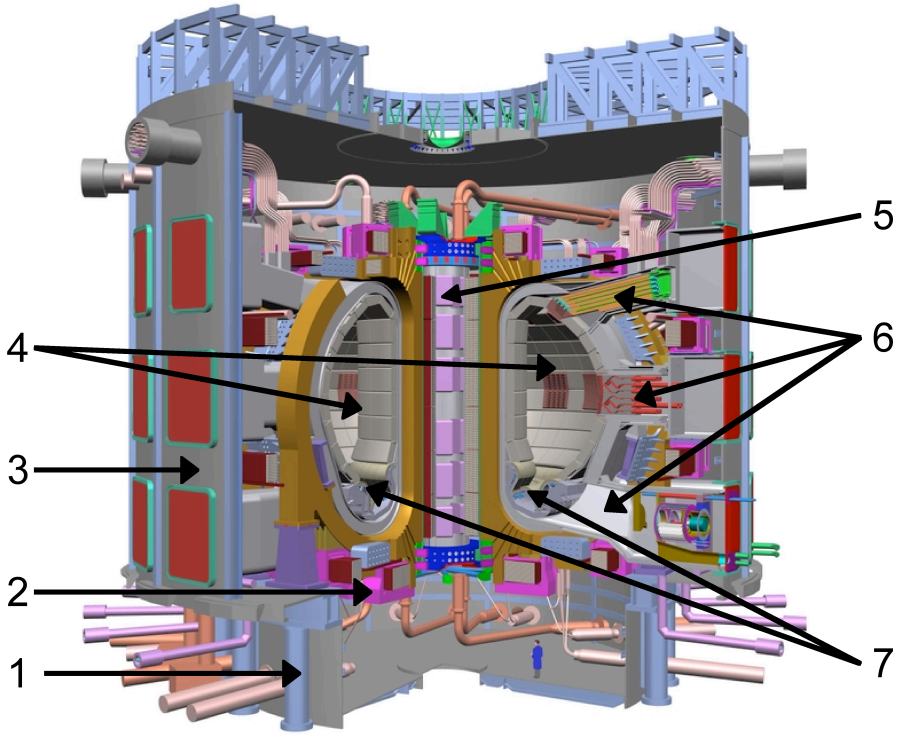

Figure 2.1: Scheme of the experimental fusion reactor ITER. 1: gravity supports; 2: cryostat; 3: bioshield; 4: Tokamak containing the plasma chamber; 5: central solenoid; 6: port plugs providing access to the plasma; 7: divertor cassettes. Blanket modules composing the plasma chamber of the Tokamak are detailed in Figure 2.3. Picture from [7].

2.1.1 Fusion reaction and fusion power

Nuclear energy is based on fission reactions, which consist of splitting heavy nuclei into smaller ones in an extremely exothermic reaction. In a fusion reaction, two small elements, usually deuterium (D), tritium (T) or helium, fuse to form a heavier atom. Amongst several possible reactions (D–D, D–T or T–He), that between deuterium and tritium (D–T) is the easiest one to initiate [8]. A plasma of deuterium (^{2}H) and tritium (^{3}H) is heated to about 100 million Kelvin. ^{2}H and ^{3}H fuse to form an unstable ^{5}H which bursts into a ^{4}He (helium ion or α particle) with 3.5 MeV of kinetic energy and a neutron (n) with a recoil energy of 14.1 MeV [9, 10]:

$$^2\mathrm{H} + {}^3\mathrm{H} \rightarrow {}^5\mathrm{H} \rightarrow \alpha \text{ (helium ion)} + 3.5 \text{ MeV} + \mathrm{n} + 14.1 \text{ MeV} \qquad (2.1)$$

α particles produced during the reaction are confined in the reactor by the magnetic field. However, neutrons are not affected and are able to escape the plasma. They move through the first wall of the vacuum chamber and, by collision, exchange energy with a coolant system (usually liquid lithium). The heat released can be used to produce steam, which generates electricity via turbines.

The initial energy of neutrons created during the deuterium–tritium fusion reaction is equivalent to 14.1 MeV (large peak in Figure 2.2) but there is also a significant flux at lower energies.

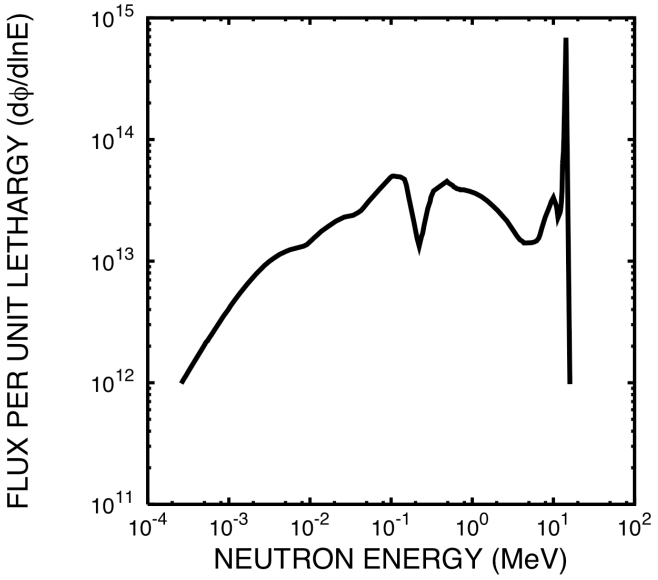

Figure 2.2: Calculated neutron energy spectrum for a fusion reactor. Graph from [11]. Calculation after [12].

The constant flux of neutrons on the first wall has three main consequences: displacement of atoms, activation of elements and generation of gas. Neutrons directly hit atoms composing the first–wall blanket of the reactor (Figure 2.3) and produce interstitials and vacancies. The material becomes radioactive and radiation–induced gas (helium, hydrogen) is produced through

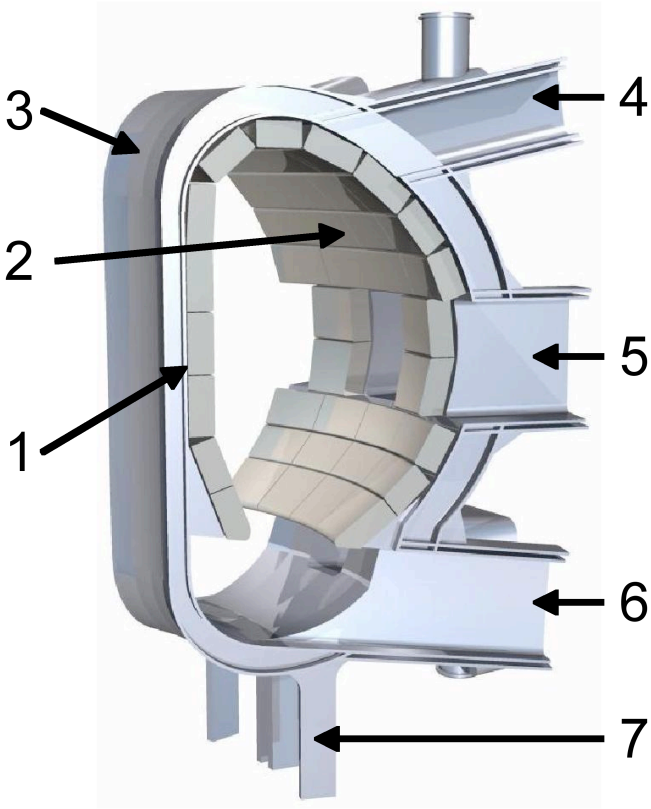

Figure 2.3: Scheme of a blanket module. 1: blankets absorbing heat and providing neutron shielding; 2: first wall; 3: toroidal field coil; 4–5–6: port plugs providing the main access to the plasma; 7: gravity support. Picture from [7].

transmutation. Such changes in the structure dramatically modify the mechanical properties of the material.

Many steps will be necessary to test materials and validate predictions before the first commercial fusion power plant produces electricity. For that purpose, several large–scale facilities are being built.

The IFMIF will be used for testing candidates in conditions similar to those found in a fusion reactor. It will use a source based on the deuteron–lithium stripping reaction (D–Li source) to accelerate deuterons on a liquid lithium target, producing a large flux of neutrons with an energy close to 14 MeV. The irradiation doses will be around 50 dpa per year, permitting the achievement of the expected critical dose of ≈200 dpa within a few years

[13, 14]. The only limiting factor is the small irradiation volume (≈0.5 L).

In parallel with the IFMIF, ITER will be an experimental full–scale fusion reactor based on a plasma torus that should produce plasma burns for 500 s and generate 400–500 MW [15]. It is being developed to prove the economic sustainability of fusion reactions as a viable energy source and will also serve as testbeds for the blanket modules [16] that will be used as structural materials in DEMO.

DEMO is a larger scale prototype designed to produce electricity and demonstrate the fusion power viability [15]. It is an intermediary step between ITER and a commercial reactor, required to satisfy all the basic functions of a power plant.

The size scales, energies involved, temperatures and levels of irradiation are constantly increasing with the development of new fission reactors and soon fusion reactors. Table 2.1 gives a comparison the targeted performances for ITER, DEMO and a commercial reactor. Table 2.2 gives an order of magnitude of some parameters for different nuclear reactors. The increasing operation temperature, irradiation dose and helium level imply that irradiation–induced changes in the material will become the main problem in structural materials. Overcoming these difficulties will be the key to a successful power plant.

Table 2.1: General performance goals for fusion devices (ITER, DEMO and a future commercial fusion reactor) [17–20].

	ITER	DEMO	Commercial reactor
Fusion Power (GW)	0.5–1	2–4	3–4
Irradiation dose (dpa)	3	30–80 (5 years)	100–150 (5 years)
Operational mode	Pulses	Quasi–continuous	Continuous

2.1.2 Irradiation damage

Fast neutrons escaping from the plasma are not deflected by repulsive forces near the nuclei of atoms and directly hit and displace them into interstitial positions, leaving trailing vacancies. If the primary knock–on atom (pka)

Table 2.2: Comparison of irradiation environments between existing, proposed fission reactors and a fusion reactor. Generation I (Gen. I) refers to the first generation of fission reactors produced in the 50–60s. Generation IV (Gen. IV) refers to the next generation of fission reactors not available available before 2030 [21].

	Fission (Gen. I)	Fission (Gen. IV)	Fission liquid metal breeder	Fusion
Max. temperature (°C)	< 300	600–1000	600	550–700
Irradiation dose (dpa)	≈ 1	$\approx$ 30–100	≈ 150	≈ 150
Helium (appm)	≈ 0.1	$\approx$ 3–10	≈ 30	≈ 1550

energy is greater than 1 keV, a sequence of collisions is initiated with other atoms (Figure 2.4) within the material [22]. Neutrons keep displacing atoms and perturbing the crystallographic lattice as long as their energy exceeds the displacement threshold (some 10 eV for metals), introducing further defects and producing more gas bubbles. Defects and bubbles both modify the mechanical properties of the material.

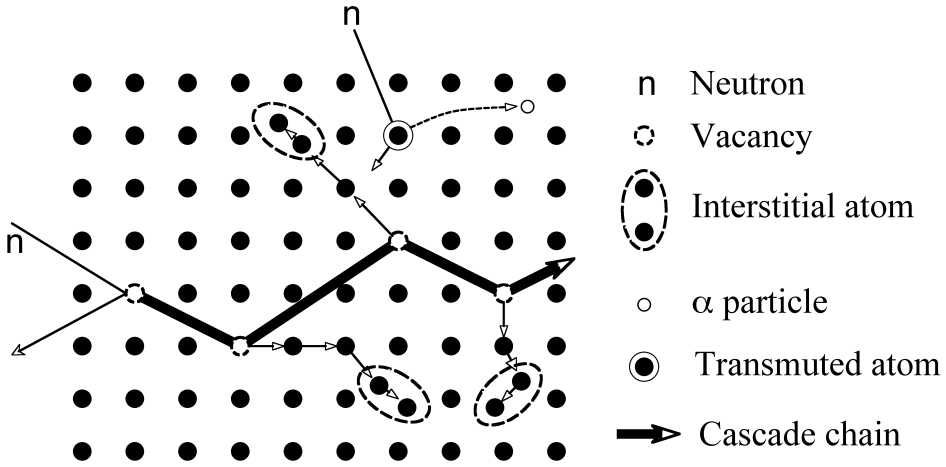

Figure 2.4: Interaction between a high–energy neutron (n) and the nuclei of a solid lattice that can lead to displaced atoms (interstitials and vacancies), transmutation products and α particles [23].

The number of displaced atoms can reach into the hundreds with corre-

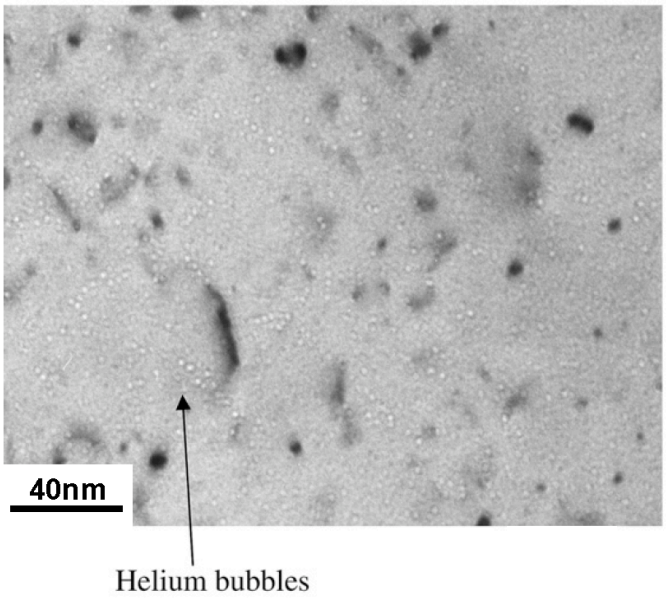

Figure 2.5: Transmission electron micrographs of 9Cr implanted with 0.25 at% He at 250°C showing helium bubbles [26].

sponding numbers of interstitials and vacancies created during the cascade. Under a given set of temperature and irradiation parameters, numerous defects immediately annihilate but others can agglomerate to create clusters and the concentration of those remaining free is a steady state between appearing and disappearing defects [10]. The new structure, consisting of interstitials, vacancies, dislocation loops, gas bubbles and radiation–induced precipitates (Figure 2.5 and 2.6), determines the intensity of the hardening [24, 25].

The accumulation of defects in the matrix leads to a slow down of the motion of dislocations which eventually causes hardening and embrittlement, characterised by an increase in the strength, a loss in the ductility and a shift in the ductile–to–brittle transition temperature. After reaching an extremum, the effects of irradiation tend to saturate [5] [27]. Besides displacement damage caused by fast neutrons, transmutation reactions lead to large helium generation rates [25].

Thermal neutrons (n) react with metallic atoms (M) to produce lighter atoms (M') and helium:

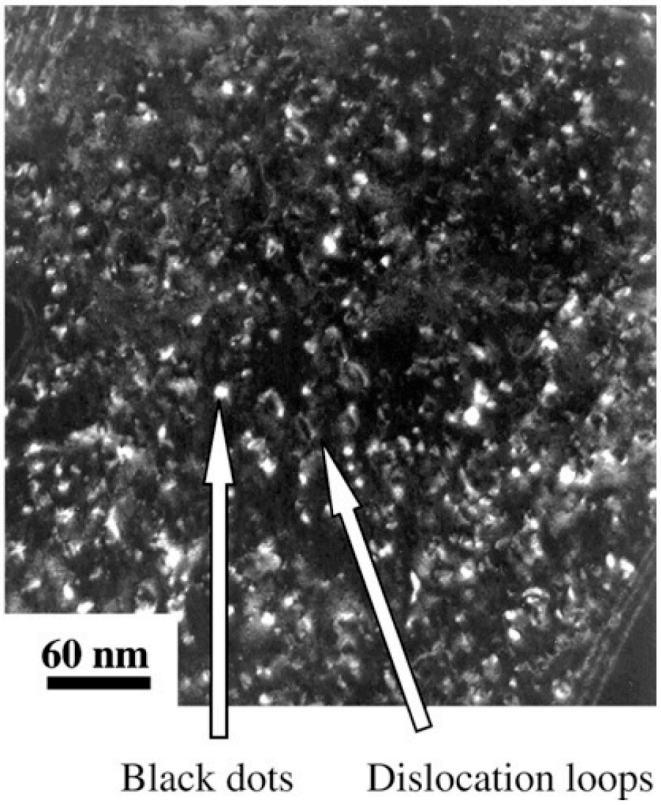

Figure 2.6: Transmission electron micrographs of 9Cr implanted with 0.25 at% He at 250°C showing dislocation loops and small defect clusters (black dots) [26].

$$ {}^{Z}_{A}\mathrm{M} + \mathrm{n} \rightarrow {}^{Z-3}_{A-2}\mathrm{M'} + {}^{4}_{2}\,\mathrm{He} \tag{2.2} $$

Elements such as nickel and boron are the most likely to produce helium:

$$ {}^{58}\mathrm{Ni} + \mathrm{n} \rightarrow {}^{59}\,\mathrm{Ni} \qquad\qquad {}^{59}\mathrm{Ni} + \mathrm{n} \rightarrow {}^{56}\,\mathrm{Fe} + {}^{4}\,\mathrm{He} \tag{2.3} $$

$$ {}^{10}\mathrm{B} + \mathrm{n} \rightarrow {}^{7}\,\mathrm{Li} + {}^{4}\,\mathrm{He} \tag{2.4} $$

Helium atoms cannot dissolve in metal and generally agglomerate in clusters to form microvoids, which lead to a swelling of the material, embrittlement and hardening. Helium–induced hardening is added to that of displaced atoms and presents a major concern especially at low temperature.

Table 2.3: Effects of the addition of 2 wt% Ni on ΔDBTT in 9Cr–1MoVNb and 12Cr–1MoVNb [28].

Temperature (Kelvin)	Alloy	Irradiation (dpa)	Helium (appm)	DBTT (Kelvin)
573	9Cr–1MoVNb	20–34	16–27	167
	9Cr–1MoVN-2Ni	21–31	184–284	218
	12Cr–1MoVNb	20-34	51–90	105
	12Cr–1MoVNb–2Ni	20–31	184–284	162
673	9Cr–1MoVNb	37–42	30–34	204
	9Cr–1MoVN–2Ni	38–42	353–391	348
	12Cr–1MoVNb	38–42	99–111	242
	12Cr–1MoVNb–2Ni	38–42	353–391	348

Until the first 14 MeV neutron source is available, nickel– or boron–doped alloys are used to simulate large quantities of helium as these elements easily transmute. Nickel has no direct effect on hardening or embrittlement but it is estimated that the irradiation of a 2 wt% Ni steel gives a helium–to–dpa ratio similar to what is expected in a fusion reactor [5] (estimated at about 10 appm/dpa [9]). Variations of the ΔDBTT in 9Cr–1MoVNb[1], 9Cr–1MoVNb–2Ni[2], 12Cr–1MoVNb[3] and 12Cr–1MoVNb[4] are summed up in Table 2.3. Variations of up to 150 K are observed.

Compared with fission reactors, transmutation rates in a fusion environment are expected to be ten times higher and will create approximately 10 appm He and 100 appm H per dpa, reaching 1000 appm He in walls exposed to loads of 10 MW yr/m^2 (100 dpa), which might make the construction of

[1] C 0.09, Mn 0.36, P 0.008, S 0.004, Si 0.08, Ni 0.11, Cr 8.62, Mo 0.98, V 0.209, Nb 0.063, Ti 0.002, Co 0.013, Cu 0.03, Al 0.013, W 0.01, Sn 0.003, N 0.050, O 0.007 in wt%, normalised 30 min at 1040°C and tempered 1 h at 760°C

[2] C 0.064, Mn 0.36, P 0.008, S 0.004, Si 0.08, Ni 2.17, Cr 8.57, Mo 0.98, V 0.222, Nb 0.066, Ti 0.002, Co 0.015, Cu 0.04, Al 0.015, W 0.01, Sn 0.003, N 0.053, O 0.006 in wt%, normalised 30 min at 1040°C and tempered 5 h at 700°C

[3] C 0.09, Mn 0.50, P 0.011, S 0.004, Si 0.18, Ni 0.43, Cr 11.99, Mo 0.93, V 0.27, Nb 0.018, Ti 0.003, Co 0.017, Cu 0.05, Al 0.030, W 0.54, Sn 0.02, N 0.020, O 0.005 in wt%, normalised 30 min at 1050°C and tempered 2.5 h at 780°C

[4] C 0.2, Mn 0.49, P 0.011, S 0.004, Si 0.14, Ni 2.27, Cr 11.71, Mo 1.02, V 0.31, Nb 0.015, Ti 0.003, Co 0.021, Cu 0.05, Al 0.028, W 0.54, Sn 0.002, N 0.017, O 0.007 in wt%, normalised 30 min at 1050°C and tempered 5 h at 700°C

a commercial fusion power plant based on present concepts unlikely [29, 30].

2.2 Alloys for power generation industry

Power generation has always been in need of new steels, especially in the Cr–Mo family, able to satisfy higher steam temperatures associated with greater thermodynamic efficiency [31]. Since the first alloys used in power generation, new steels have been developed to meet the criteria for fusion, with the radiological requirement of low–activation characteristics to avoid long–lived radioactive waste and the mechanical requirement of long lifetime (upper operating temperature of 550–600°C with an estimated operating stress of $\approx$ 50 MPa [32]) under neutron bombardment. As seen in the next section, austenitic and ferritic steels were first considered candidates as well as vanadium alloys and silicon carbides [33] but low–activation ferritic/martensitic alloys are today in the most advanced stage of development in the context of fusion.

2.2.1 Austenitic steels

In the early 1970s, austenitic stainless steels were the favourite candidates for liquid metal–cooled reactors because of their good properties and corrosion resistance at high temperature and their weldability [33]. The main candidate AISI 316 was in the 17 wt% Cr range with 13 wt% Ni and 2 wt% Mo. However, the observation of swelling due to high–nickel concentrations in neutron–irradiated AISI 316 led to the search for a replacement and efforts were made to find a substitute that would have a reduced tendency to swell but also better mechanical properties (creep, rupture strength, post–irradiation tensile strength) and ferritic alloys were then considered.

Austenitic steels are not suitable for use at high fluences because they are life–limited by high–temperature embrittlement [34] which reduces the upper operating temperature and because they do not exist in low–activation versions as attempts to replace nickel by niobium have not been successful [35]. However, they will be used in ITER as its principal structural material because they are well qualified for moderate upper temperatures and limited neutron fluences, and are available for immediate construction [34].

2.2.2 Ferritic steels

In the late 1970s, ferritic steels were introduced in the fusion materials programme [36] and were considered the first candidates for fusion power plants because they were found to be more swelling–resistant than austenitic stainless steels. They also had a higher thermal conductivity and a lower thermal expansion, which gave them a better resistance to thermal stress in a pulsed mode [37].

One of the concerns about ferritic steels is that they are ferromagnetic and hence may interfere with the magnetic field in the reactor (field perturbation of the plasma or magnetostatic forces on the structures) [38] but calculations have proved that this problem can be handled by a careful design of the reactor [30].

2.2.3 Low–activation ferritic/martensitic steels

Low–activation ferritic/martensitic (LAFM) or reduced–activation ferritic/martensitic (RAFM) are now the main candidates for DEMO and future fusion reactors [34] as they are the most advanced amongst the three candidates [39] and have achieved the greatest maturity in production, welding technology and industrial experience. They have acceptable radiological performance and long term radiation levels following neutron irradiation [16]. RAFM are based on conventional Fe–(8–12)Cr–(1–2)Mo steels with slight modifications in the composition.

The idea of low–activation or reduced–activation steels was first introduced in the international fusion programme in the middle of the 1980s when it was noticed that replacing elements likely to transmute would not affect their mechanical properties and would allow a control on activation levels in reactor structural materials [40].

True low activation alloys do not exist because of the transmutation of iron itself and because undesirable elements cannot be totally removed. However low– or reduced–activation alloys are such that radioactivity decays rapidly once the nuclear exposure stops and allow land burial to dispose of radioactive wastes instead of deep geological storage. The activation level is

reduced by suppressing elements from the composition and keeping others with longlived radioactive isotopes to minimal concentrations (Table 2.5).

Calculations were first carried out to determine which elements needed to be reduced to minimise the activation and obtain a quick decay of induced radioactivity levels after irradiation [5]. Molybdenum was replaced by tungsten to produce Cr–W steels as an alternative to Cr-Mo steels and niobium was replaced by tantalum [37]. Elements such as B, Nb, Cu and N were kept to a minimum [37, 41]. Low–activation steels now show mechanical properties which are as good as or better than that of commercial steels [21].

2.2.4 International collaboration

At an International Energy Agency workshop in 1992 in Tokyo, a programme was brought forward to determine the feasibility of using ferritic/martensitic steels for fusion. Japan offered to make large heats of low–activation ferritic/martensitic steel to be used in collaboration [32]. Now, Japan, Europe and the USA work on three different candidates.

The Japanese fusion programme focuses on two types of RAFM: F82H, from the Japanese Atomic Energy Agency and JLF–I, from Japanese universities (Table 2.4). Two 5–tonne heats of F82H were produced in 1993 and 1995 and used for physical and mechanical characterisation in irradiation experiments in the High Flux Isotope Reactor (HFIR) in the US, the Japan Research Reactor (JRR–4), the Japan Materials Test Reactor (JMTR) in Japan, and the High Flux Reactor (HFR) in The Netherlands. A 1–tonne batch of JLF–I was produced for the Japanese Universities Fusion Materials Programme and tested mainly in Japanese universities [30].

The European fusion programme focuses on Eurofer'97, a 9CrWVTa reduced–action ferritic/martensitic steel based on the Japanese F82H and JLF–I whose composition (Table 2.4) was defined in 1997 [35]. Two batches of Eurofer'97 were produced in 1999 and 2004 [42] and a large campaign of irradiation and characterisation was carried out, demonstrating that the European candidate had a good hardening, tempering and transformation behaviour compared with other RAFMs. The next step in the programme

Table 2.4: Composition in wt% of JLF–1 [44], F82H [45], Eurofer'97 [32], HT9 [46] and 9Cr–2WVTa (ORNL) [47].

Element	JLF–1	F82H	Eurofer'97	HT9	9Cr-2WVTa
C	0.1	0.097	0.109	0.21	0.1
Si	0.24	0.09	0.003	0.18	0.2
Mn	0.48	0.07	0.49	0.5	0.45
P	0.002	0.002	0.011	0.011	-
S	0.003	0.003	0.003	-	-
Cr	8.87	7.49	9.04	11.99	8.5–9
V	0.19	0.18	0.19	0.27	0.25
W	1.9	2.1	1.04	0.54	2.0
Mo	-	-	-	0.93	-
Ta	0.084	0.03	0.140	-	0.07
Nb	-	-	-	0.018	-
N	0.024	0.002	0.023	0.020	-
Cu	-	-	0.04	0.05	-
Ni	-	-	0.06	0.43	-
Al	-	-	-	0.03	-
Sn	-	-	-	0.002	-

is the development of Eurofer–II with improved post irradiation mechanical properties and then Eurofer–III with a control of levels of impurities for real low–activation with recycling times below 100 years [35]. The production of experimental heats is well advanced but the control of impurities in large batches is more delicate.

In the USA, Sandvik HT9 (Table 2.4), which had been developed in Europe for fast reactors, was the first alloy considered for the fusion programme. At the beginning of the 80s, the US Department of Energy called for development of low–activation materials and several other alloys were designed [40]. The US fusion programme now mainly focuses on 9Cr–2WVTa (Table 2.4), developed by the Oak Ridge National Laboratories in the mid–1980s [43] and F82H, produced as a part of the US Department of Energy / Japan Atomic Energy Research Institute (JAERI) collaboration [39].

Table 2.5: Level of impurities in several low–activation steels [48]. Concentration are given in wppm.

Element	F82H	JLF–1	9Cr–2WVTa	9Cr–1Mo	HT9
Ag	<0.1	0.21	0.16	0.23	1.3
Bi	<0.05	<0.1	<0.05	<0.1	<0.1
Cd	<0.05	<0.05	<0.05	3.3	5.1
Co	16	7.6	34	58	393
Ir	<0.05	<0.05	<0.05	<0.05	<0.05
Mo	19	20	70	-	-
Nb	2.4	4.3	4	-	23
Ni	474	13	402	1251	5692
Os	<0.05	<0.05	<0.02	<0.02	<0.05
Pd	<0.05	<0.05	0.18	0.27	0.4
Dy	<0.05	<0.05	<0.05	<0.05	<0.05
Er	<0.05	<0.05	<0.05	<0.05	<0.05
Eu	<0.05	<0.05	<0.05	<0.05	<0.05
Ho	<0.05	<0.05	<0.05	<0.05	<0.05
Tb	-	<0.05	-	<0.05	<0.05
U	<0.05	<0.05	0.6	0.12	<0.05
Al	14	26	170	<0.1	44
Cu	100	100	300	300	1000

2.2.5 Concerns and future options

Reduced activation ferritic/martensitic steels are the most developed and characterised alloys for DEMO but still present some unacceptable properties. Their upper operational temperature is limited by a drop in mechanical strength at 500–550°C [16] and their lower temperature is limited to 350°C by radiation–induced embrittlement. Further research is needed to investigate enhanced creep and hardening resistance, as well as a better quantification of the loss of ductility, shift in the ductile–to–brittle transition temperature and decrease in fracture toughness. No conclusive answer can be given on actual performance in a fusion reactor before a dedicated 14 MeV neutron source exists but modelling can contribute [42]. A short review of work on models of irradiated steels is given in Section 3.1.3. However, the main concern remaining is the effect of helium and hydrogen on fracture properties.

Research now mainly focuses on creating advanced low–activation ferritic/ martensitic steels with improved elevated–temperature properties in order to increase the upper temperature operating limit. Alloys with an increased tungsten concentration (up to 3 wt%) have shown interesting properties in the sense that the creep strength is enhanced by tungsten in solution [30].

Ferritic or ferritic/martensitic steels strengthened with a fine dispersion of oxide (ODS) have also been considered as they have been shown to have improved mechanical properties at high temperature compared with conventional ferritic or ferritic/martensitic steels (Figure 2.7). The numerous interfaces between oxides and the matrix represent sinks for defects. The high density of defects act as nucleation sites for helium bubbles [16, 39]. Work is being carried out in Europe, the USA and Japan on ODS versions of existing RAFMs (Eurofer ODS, 9 and 12Cr–Y_2O_3) [30]. ODS reduced–activation alloys have presented superior high temperature creep properties. However, even if ODS show promising results at low irradiation doses [49], homogeneity of microstructure and isotropy of properties resulting from the way they are fabricated remain a problem and still very little is known about their response to higher irradiation doses and about their welding potential [39].

2.3 Mechanical properties of irradiated steels

Vacancies, interstitials and helium atoms introduced during irradiation block the motion of dislocation leading to hardening and embrittlement.

During irradiation, the strength of the steel increases with the irradiation dose and the defect concentration. Figure 2.8 shows the yield strength for a 316L stainless steel[1] irradiated with neutrons at different doses, highlighting a direct relationship between the strength and the extent of irradiation, measured in displacements–per–atom (dpa).

Figure 2.9 shows the variation in strength and Figure 2.10 the shift in the ductile–to–brittle transition temperature of several ferritic/martensitic

[1] C 18.55, Ni 11.16, Mo 2.01, Mn 1.7, Cu 0.026, Si 0.15, C 0.028 in wt%

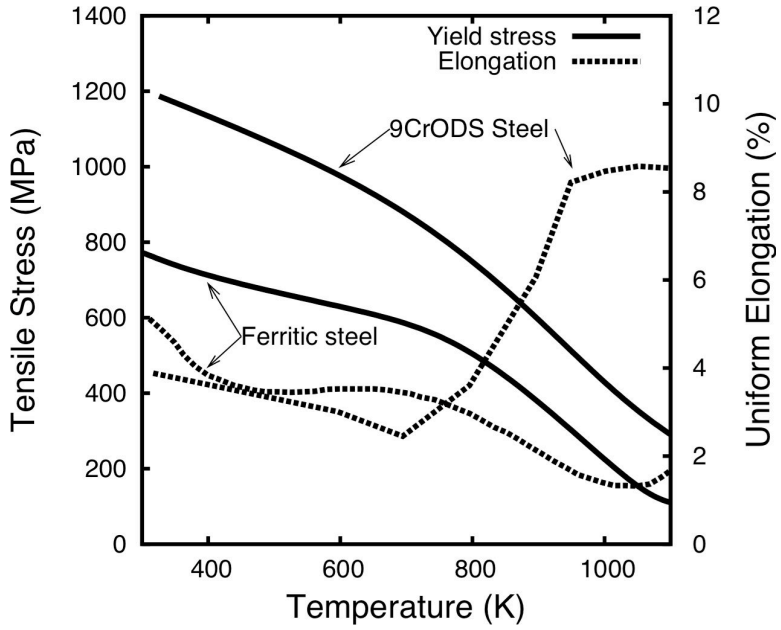

Figure 2.7: Properties of oxide–dispersion strengthened alloys compared to conventional ferritic steels [50].

steels as function of fluence.

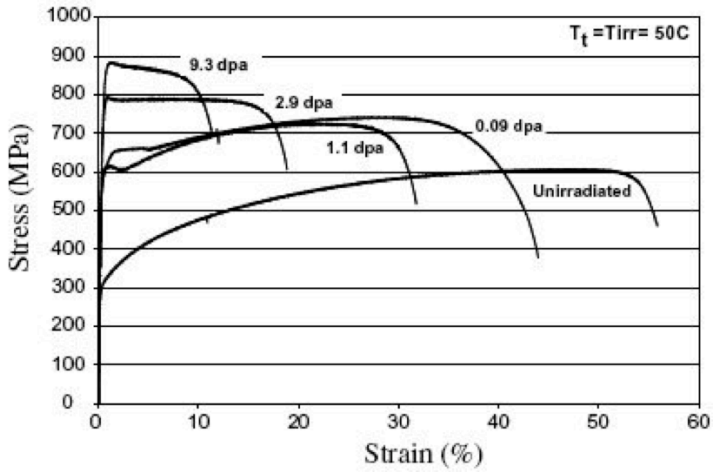

Figure 2.8: Stress/strain curves from annealed 316L stainless steel irradiated with neutrons at different doses [51]. Test temperature (T_t) and irradiation temperature (T_{irr}) were both 50°C. The yield strength increases from 300 MPa in the unirradiated state to 900 MPa at 9.3 dpa.

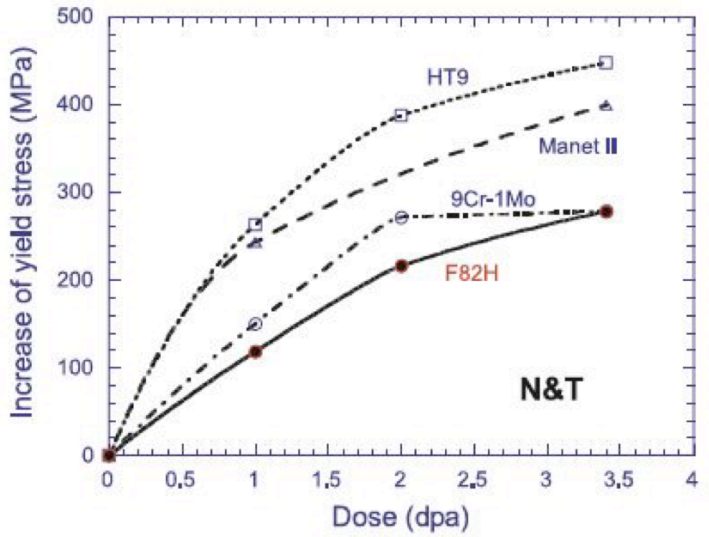

Figure 2.9: Variations in yield stress ($\Delta\sigma$) with irradiation dose for different normalised and tempered reduced-activation steels [52]. Compositions are given in Table 2.6.

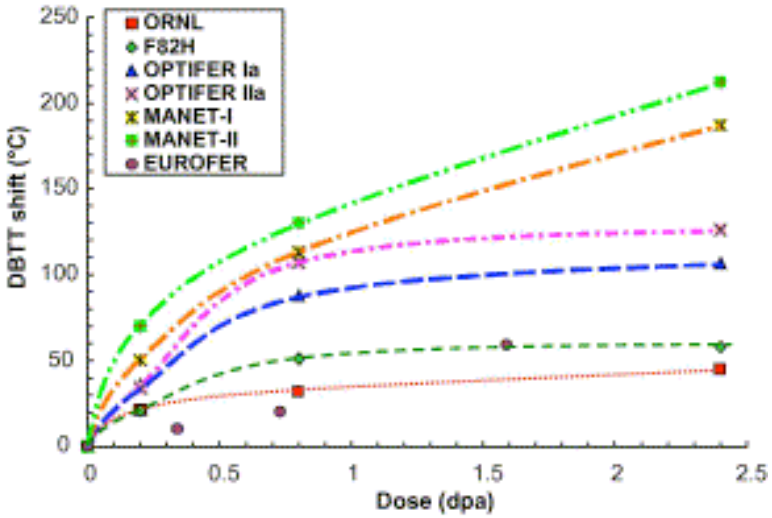

Figure 2.10: Shift in the ductile–to–brittle transition temperature (ΔDBTT) with irradiation dose for Eurofer'97 and different normalised and tempered reduced–activation steels [53]. Compositions are given in Table 2.6.

Table 2.6: Chemical composition in wt% of MANET I and II [54], OPTIFER-Ia and -II [55], F82H [56]

Alloy	C	Cr	Ni	Mo	V	Nb	
MANET I	0.13	10.6	0.87	0.77	0.22	0.16	
MANET II	0.1	10.3	0.65	0.57	0.19	0.14	
OPTIFER-Ia	0.11	9.3	-	-	0.26	-	
OPTIFER-II	0.13	9.5	-	-	0.28	-	
F82H	0.09	7.46	-	30 wppm	0.15	1 wppm	
Alloy	Si	Mn	B	N	Ta	W	Ge
MANET I	0.37	0.82	0.08	0.02	-	-	-
MANET II	0.14	0.75	0.08	0.03	-	-	-
OPTIFER-Ia	-	0.5	0.006	0.016	0.07	0.96	-
OPTIFER-II	-	0.49	0.006	-	-	-	-
F82H	0.10	0.21	-	0.006	0.023	1.96	-

During irradiation, cascades created by neutrons cause point and cluster defects that can relax and diffuse. Interstitials and vacancies created as near neighbours can recombine and annihilate and others can be trapped by sinks, such as grain boundaries or dislocations, or can aggregate to preexisting defects to create bigger defect clusters, contributing to the hardening [23].

Two mechanisms have been proposed to explain hardening. At low doses, hardening is produced mainly by point defects or small clusters whereas at higher doses, it is caused by dislocation loops and networks. These obstacles are barriers to dislocation motion and give rise to the strengthening [5].

The saturation in hardening is attributed to a limit in the concentration of dislocation loops formed by self–interstitials [5]. Klueh and Vitek [10] assumed that in ferritic steels, hardening is first due both to displacement damage and helium production. Then, strengthening due to the dislocation loops begins to saturate and a transition from loop nucleation to growth appears. Loops no longer nucleate but existing ones keep growing and are sinks for new vacancies. The production of helium also continues with increasing irradiation dose. This explains why the rate of increase in strength

diminishes significantly. Further hardening can be explained by the production of helium. Irradiation hardening saturates with fluence when hardening is due to displacement damage alone, as it is the case in the Experimental Breeder Reactor–II (EBR–II), where little helium is produced [5]. Irradiation hardening saturates at a higher strength level in a high flux isotope reactor, where both displacement damage and helium are produced [5].

The saturation value and the transition from loop nucleation to growth depends on the steel composition and the irradiation parameters, particularly the irradiation temperature. That change in regime has been observed at doses ranging from 0.05 dpa in a 9Cr–1MoVNb steel irradiated at 60–100°C [57] and 10 dpa in a 9Cr–2W alloy irradiated at room temperature [58] .

Chapter 3

Modelling properties with artificial models

There are many properties of a material that can be modelled by simple empirical equations but this implies that a relationship between inputs and outputs has to be chosen before analysis. In some cases, such choice tends to be too simple to capture the complexity of the problem. Artificial neural networks (ANN) and Gaussian processes (GP) are ideal substitutes as there is no need to select a particular mathematical function before designing the model and the network is able to capture complex phenomena. ANN and GP are used widely in materials science [59], from online monitoring for welding [60] to the discovery of new microstructures with the design of the δ–TRIP steels [61]. To a lesser extent, Gaussian processes have also been used in various domains [62] and in metallurgy [63–66].

3.1 Neural network

Linear or pseudo–linear mathematical functions are commonly used to describe physical phenomena. The output parameter y is given as a function of a set of input parameters x_j on which y depends. Every term x_j is multiplied by a weight w_j, specifically chosen for the predicted value to fit experimental data. A constant θ is added to the sum of every term $x_j \times w_j$ to give an expression for y as follows:

$$y = \theta + \sum_j x_j \ \times \ w_j \tag{3.1}$$

Such expressions have been used to predict properties which depend on a limited set of inputs, like the martensite–start temperature M_s of an alloy as a function of its chemical composition for example [67]:

$$\begin{aligned} M_s(K) = {} & 767.7 - 305.4 \times \text{wt\%C} - 30.6 \times \text{wt\%Mn} - 14.5 \times \text{wt\%Si} \\ & - 8.9 \times \text{wt\%Cr} - 16.6 \times \text{wt\%Ni} + 2.4 \times \text{wt\%Mo} + 5.3 \times \text{wt\%V} \\ & + 8.58 \times \text{wt\%Co} + 40.4 \times \text{wt\%Al} + 7.4 \times \text{wt\%W} - 11.3 \times \ \text{wt\%Cu} \\ & + 510.4 \times \text{wt\%Nb} \end{aligned} \tag{3.2}$$

This simple method gives reliable results but has several disadvantages, because a specific relation has to be chosen before the analysis and can only be applied on a limited range of values. This can be overcome by using an artificial neural network, for which there is no need to choose a precise relationship before analysis.

An artificial neural network is a regression method which aims at fitting a function to experimental data. Just like a classical regression method, an artificial neural network uses input parameters, which define the input nodes and gives an output parameter, which defines the output node. The relationship between inputs and the output is non–linear and can be extremely complex. Details on the method can be found in the literature [68, 69].

In a neural network, the input parameters x_j are combined to form hidden units h_i also called neurons, which are then combined to form the output y. Figure 3.1 shows the structure of a simple neural network with 3 input parameters (x_1, x_2, x_3), 2 hidden units (h_1, h_2) and the output (y):
Input parameters are multiplied by a weight $w_{ij}^{(1)}$ and combined with a constant $\theta_i^{(1)}$ to form the argument of an hyperbolic tangent transfer function, which represents the hidden unit h_i (Equation 3.3). $\theta_i^{(1)}$ is analogous to the constant that appears in a linear regression:

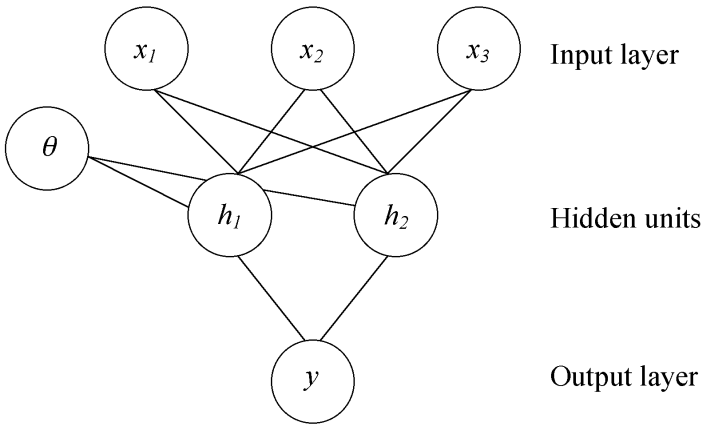

Figure 3.1: Structure of a simple neural network

$$h_i = \tanh\Big(\sum_j w_{ij}^{(1)} x_j + \theta_i^{(1)}\Big) \quad \text{(hidden unit)} \tag{3.3}$$

The hyperbolic tangent function is chosen because of its great flexibility. By selecting the appropriate weights and constant, it can have any complex shape. If the function needed requires greater flexibility and if a one hidden–unit model is not flexible enough, several hyperbolic tangents can be added to form the output y (Equation 3.4). Another set of parameters ($w_i^{(2)}$ and $\theta^{(2)}$) is then chosen to best fit the experimental data. Figure 3.2 gives an example of the flexibility of a hyperbolic tangent.

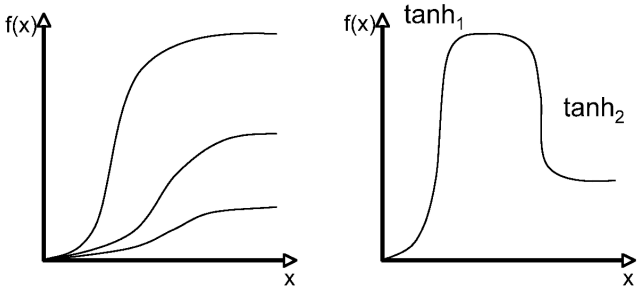

Figure 3.2: Complexity of an hyperbolic tangent function. A model with one hidden unit (left) may not be flexible enough. The combination of two hyperbolic tangent functions $\tanh_1$ and $\tanh_2$ can form a more complex model (right).

$$y = \sum_i w_i^{(2)} h_i + \theta^{(2)} \tag{3.4}$$

3.1.1 Training of a neural network

Neural networks used in this thesis were trained with BIGBACK, a program written by David MacKay [70], in a Bayesian framework. The benefits of such a property are described later.

Before the training, every input parameter is *normalised* between -0.5 and +0.5:

$$x_n = \frac{x - x_{min}}{x_{max} - x_{min}} - 0.5 \tag{3.5}$$

where x is the original value, x_n the normalised value, x_{max} and x_{min} the maximum and minimum values in the database for that variable.

This simplifies the calculations and allows to compare the relative significance of an input on the output, without biasing the comparison with the absolute value of the variable as, in some cases, input parameters vary over a large range. For example, in irradiated steel, the carbon concentration varies between ≈ 0 and some tenths of a wt% whereas the helium concentration varies between 0 and 5000 appm.

The training is carried out on pre–existing experimental data. An initial set of weights and seeds (prior value to begin the model) are randomly chosen and weights are successively adjusted for the output parameter to fit experimental data. This optimisation is done by minimising an objective function M:

$$\left.\begin{array}{l} M(w) = \alpha E_w + \beta E_D \\ E_D = \frac{1}{2}\sum_j (t_j - y_j)^2 \\ E_W = \frac{1}{2}\sum_{ij} {w_{ij}}^2 \end{array}\right\} \tag{3.6}$$

E_D, the *sum squared error* between the target and the prediction for a given choice of weights represents the overall error and E_w is the regulariser that encourages the network to use small weights. α and β are regularisation constants that influence the complexity of the model, y_j is the predicted and t_j the measured value.

The method used here, based on the Bayesian probability theory, treats the training as an inference problem. The algorithm does not calculate the best set of weights but gives a probability distribution of weights. The performance of various models created is evaluated by using the logarithmic predictive error (LPE) (Equation 3.7) for which the penalty for making a wild prediction is reduced if it is accompanied by appropriately large error bars:

$$LPE = \sum_i \left(\frac{1}{2} \left[\frac{t^{(i)} - y^{(i)}}{\sigma_{y_i}} \right]^2 + \log \left(\sqrt{2\pi} \sigma_{y_i} \right) \right) \tag{3.7}$$

where σ_{y_i} is related to the uncertainty of fitting for the set of inputs x_i and t and y is as defined in Equation 3.6. The best models have the highest LPE value.

Overfitting

A problem which might happen because of the flexibility of neural networks is the possibility of overfitting. Combinations of hyperbolic tangents are so flexible that a model can overfit the experimental data, *i.e.* the function may even fit noise in the data to an unrealistic level of accuracy. Figure 3.3 gives an example of a complex function that passes through every training point (black dots) but not through testing points (crosses). In other words, it generalises badly on data not used in creating the model.

To avoid this, the database is divided into two sets called *training* and *testing set*. The neural network is trained on the first set then tested on the latter. Figure 3.4 shows an example of a model that was trained on the seen dataset (black spots) and then tested on the unseen dataset (white spots). In this case, all experimental data are reasonably estimated, avoiding the overfitting observed in Figure 3.3.

The ability of a model to catch every non–linear relationship depends on its complexity (number of hidden units). In the event of overfitting, the weights and constant of the model are adapted to minimise the test error (TE). A model which is too simple will not be able to catch complex variations whereas one which is too complex might overfit experimental data. Usually the TE decreases with increasing complexity of the model and then increases again. The complexity is optimised when the TE reaches its min-

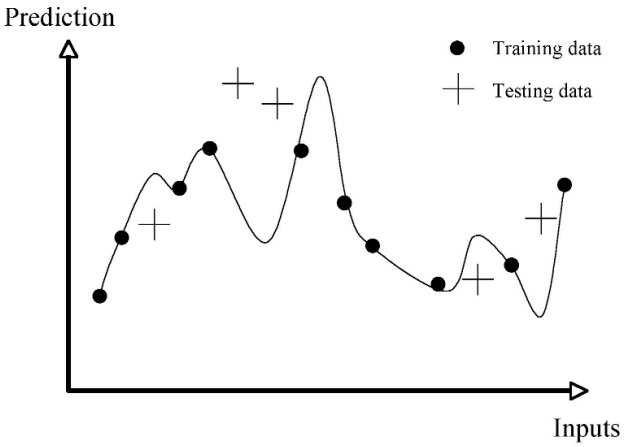

Figure 3.3: Overfitting of experimental data. The model fits on training data but generalises poorly on unseen data

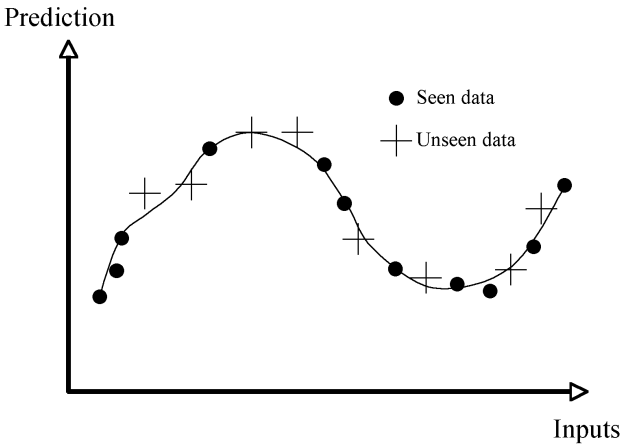

Figure 3.4: Example of a good generalisation of the model. The fitting is maximised on both data seen and unseen by the model during the training.

imum value (Figure 3.5).

Models with different hidden units and initial seeds do not give identical predictions. The performance of a combination of models is usually better than with the best single model. Such combination is called a *committee*. The committee which gives the lowest overall test error is selected and retrained on the database for a final adjustment of the weights without

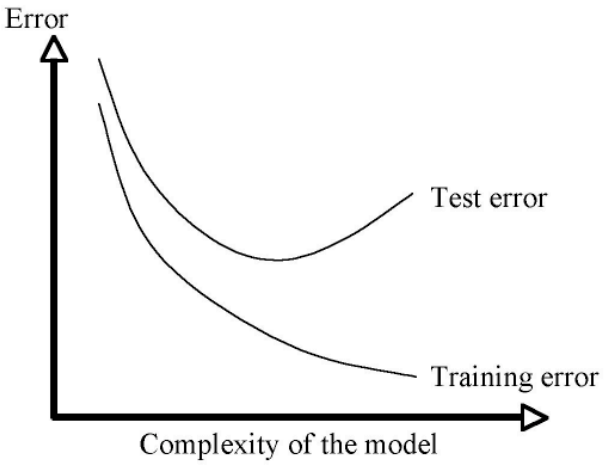

Figure 3.5: Testing error and training error as a function of the model complexity

changing its architecture.

Uncertainties

When using neural networks, attention must be given to modelling errors. It is important to distinguish between two kinds of errors: one representing the perceived level of *noise* in the output and the other representing the *uncertainty* in fitting the data.

The first one, noise, reflects fluctuations in the output when an experiment is repeated a number of times because some parameters cannot be controlled.

The second component comes from the Bayesian framework and allows the estimation of the extent to which the same data may reasonably be represented by a variety of different mathematical formulations without unduly compromising the fit in the region where experiments exist.

The Bayesian environment assesses the relative probabilities of models of different complexity. The individual formulations may then extrapolate differently, giving an indication both of the dangers of extrapolation and also identifying domains where further experiments are needed. It allows quantitative error bars to be obtained which vary with the position in the input space depending on the uncertainty of fitting the function in that

region of the space. For example, many models that reasonably fit the same data might extrapolate differently in domains where knowledge is sparse. If several functions can represent the trend between two populated areas (Figure 3.6), the model will then be accompanied with large error bars, reflecting the uncertainty of the prediction.

It is possible to evaluate the uncertainty of modelling, σ_y:

$$\left.\begin{array}{l} {\sigma_y}^2 = \frac{1}{L}\sum_l {\sigma_y^{(l)}}^2 + \frac{1}{L}\sum_l \left(y^{(l)} - \overline{y}\right)^2 \\ \overline{y} = \frac{1}{L}\sum_l y^{(l)} \end{array}\right\} \tag{3.8}$$

where $\overline{y}$ is the prediction of a committee of networks, L the number of models in the committee, l refers to the model used to make the corresponding prediction $y^{(l)}$. Modelling uncertainties are often given for 1 σ and are presented as error bars.

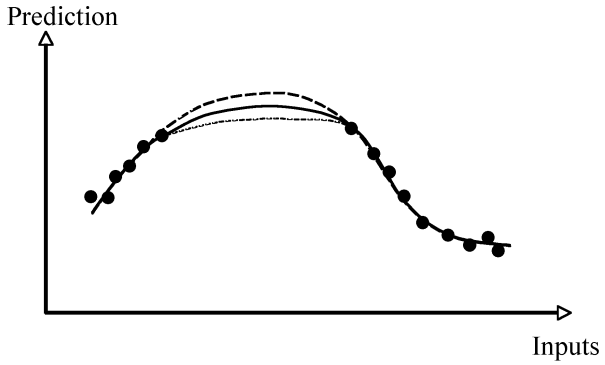

Figure 3.6: Example of modelling uncertainty on sparse data. Several mathematical models reasonably fit experimental values but give different solutions in less–populated areas.

Furthermore, it is also possible to calculate a significance (σ_w) associated with each input, which is a measure similar to a partial correlation coefficient, and expresses the extent of the influence of the given input on the output. Analysing σ_w is a good way to determine which parameters particularly affect the output and require more attention.

The model is completely defined by the weights but it is not easy to interpret them individually. The usual way to find interactions between inputs and the output is to vary one of the input parameters while keeping the other fixed and monitor the response of the output.

3.1.2 Usage of neural networks

Neural networks are commonly used in materials science [59] and also in a variety of fields such as hydrological science [71], atmospheric science [72], civil engineering [73], process engineering [74] and structural engineering [75] but in the vast majority of cases, the exploration of the models is incomplete and the models themselves are not systematically made available to other researchers. A method to evaluate the use of neural networks and their dissemination is discussed here.

Two important features of neural networks are their ability to extrapolate and their capacity to produce predictions accompanied with modelling uncertainties. Both are intimately related as uncertainties increase when calculations are realised in domains where no data exist.

The role of uncertainties in neural–network modelling has been discussed in [76]. It is a precious tool to evaluate the noise in the data, which is due to fluctuations in parameters that cannot be controlled, and modelling uncertainties (Figure 3.6), which are due to the different behaviour of mathematical functions in domains where no experimental data exist. Predictions given without uncertainties cannot be satisfactorily interpreted. Large error bars are also an indication that experimental data are lacking and that more experiments should be carried out.

After the training, it is necessary to explore the behaviour of the model by making predictions. It is necessary to be able to explain predicted trends physically and check that they are in reasonable agreement with experimental values, to ensure that physical mechanisms have been captured correctly. This also includes the possibility to extrapolate to perhaps lead to the discovery of new phenomenon.

A relevant scientific publication must detail the method, the procedure and the outcomes and give enough details to allow other researchers to reproduce the work. In papers dealing with neural networks, results are given but details about the structure of the database and the training of the model itself are often lacking, preventing the reproducibility of the work.

An assessment of publications about neural networks has been realised to evaluate the use of models and their dissemination. A marking system (Table 3.1) has been established to rank the papers:

- Data were collected, compiled and the model was created (one point).
- The model was used for predictions which were interpreted. *Prediction* must be understood as *extrapolation* as this does not only include calculations for input values inside the database but also beyond that range (two points).
- Modelling uncertainties were calculated and the level of confidence in predictions discussed (two points).
- Predictions and modelling uncertainties were calculated and the predictions experimentally validated (two points).
- The model (or all the information necessary to recreate it, *i.e.* the database, the references of the program used and the details of the training) was made available to the community of researchers (three points).

The scheme is summed up in Table 3.1 and 95 articles published between 2005 and 2007 (the complete list can be found in [77]) were marked accordingly.

Characteristics	Mark
Model or data disseminated	3
Prediction investigated experimentally	2
Modelling uncertainties	2
Predictions made and interpreted	2
Model created	1

Table 3.1: Marking scheme for module [76].

The result of that assessment is given in Figure 3.2. Surprisingly, for the vast majority of publications, authors make a minimal use of the models, ignore modelling uncertainties and do not evaluate predictions. Moreover, models are often never diffused and the reproducibility of the work is compromised.

Publications about neural networks should always provide a comprehensive description of the database and model and authors should make them easily available to the community.

Mark	Number of papers
10	1
8	1
7	1
6	1
5	5
4	0
3	20
1	66

Table 3.2: Ranking of the papers [76].

3.1.3 Neural–network models of irradiated steels

Mechanisms of radiation–induced hardening and embrittlement cannot lead to quantitative predictions but several methods have been used to model interactions between the defect density, the irradiation dose, the microstructure of steel and the mechanical response of an alloy. Elementary interactions have been modelled by molecular dynamics [78], kinetic Monte–Carlo [79] and *ab–initio* methods [80]. Empirical formulae have often been fitted to experimental data to model the macroscopic properties of irradiated steels [81, 82].

Large quantities of experimental data from irradiation experiments in fission reactors have been used to create neural–network models of the yield strength (Figure 3.7) [83] and the ductile–to–brittle transition temperature (Figure 3.8) [84] showing results in good agreement with experimental values.

The ability of an ANN to extrapolate to domains where no experimental data are available was used to estimate the yield strength of two different steels at irradiation doses as high as 200 dpa, corresponding to a fusion environment (Figure 3.9). In both cases, the error bars become very large and no clear conclusion could be drawn. The possibility to know modelling uncertainties due to the lack of experimental data is a major asst when using neural networks since they constitute a rigourous measure of the extent of extrapolation.

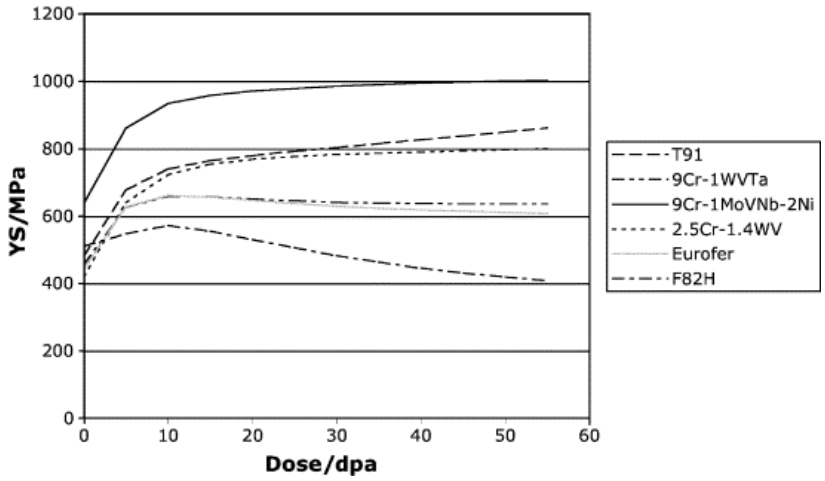

Figure 3.7: Neural–network calculation for variations in yield strength for 6 different alloys as a function of the irradiation dose. Modelling uncertainties were removed for clarity [83]. The steep increase in yield strength is observed for doses below 10 dpa, followed by a slower hardening rate for T91, 9Cr–1WVTa and 9Cr–1WVTa–2Ni and by a recovery for 2.5Cr–1.4WV, Eurofer'97 and F82H.

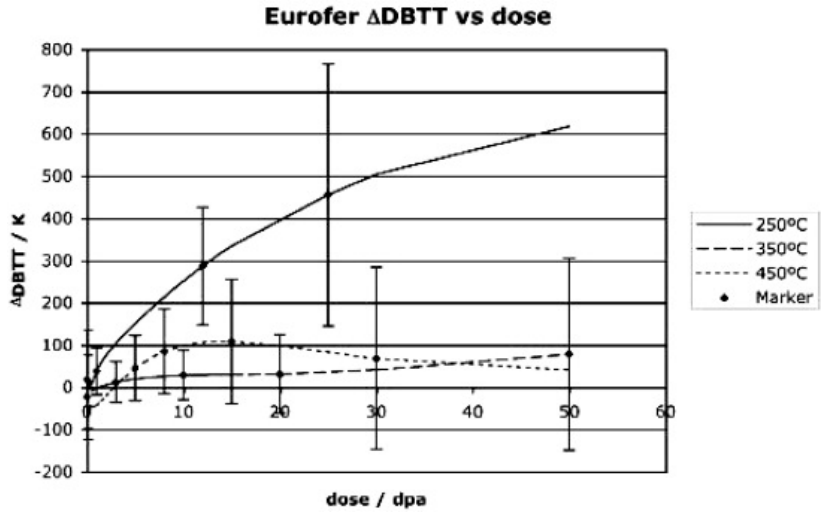

Figure 3.8: Neural–network calculation for variations of the ductile–to–brittle transition temperature as a function of the irradiation dose [84]. The dependency of ΔDBTT on the irradiation dose and temperature is shown.

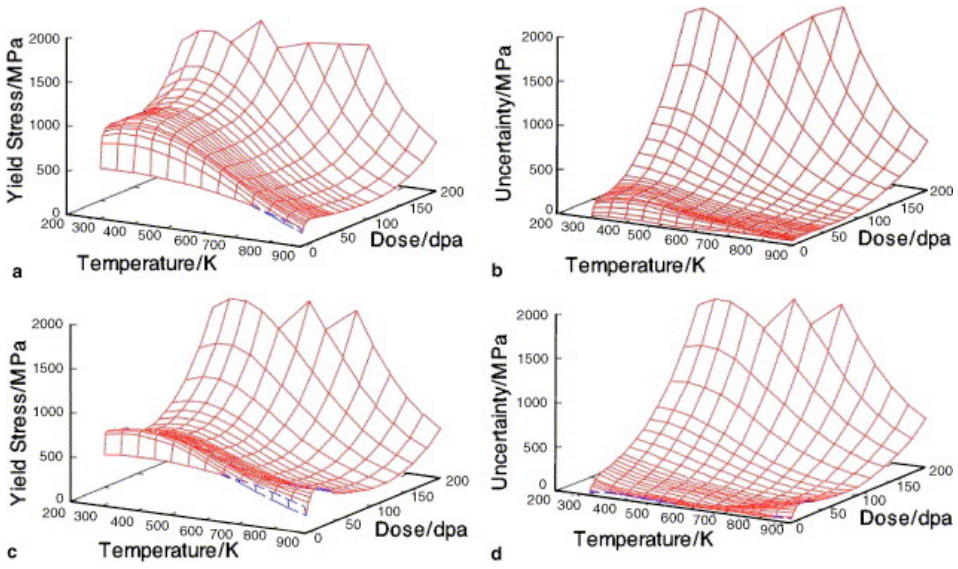

Figure 3.9: Neural–networks predictions for variations of the yield strength as a function of the irradiation dose and irradiation temperature for two reduced–activation ferritic/martensitic steels: prediction (a) and modelling uncertainties (b) for Eurofer'97, prediction (c) and modelling uncertainties (d) for F82H [83].

3.2 Gaussian process

Gaussian process models have an approach similar to that in neural networks. They are a regression tool that can discover relationships in large sets of data but when neural networks parametrise a relationship between inputs and an output by inferring a set of weights, GP rather parametrise a probability distribution over the whole dataset. GP models can be considered a generalisation of neural networks for which all possible values of the weights have been integrated.

Similarly to neural networks, the *inputs–output* relationship in GP is characterised by hyperparameters Θ, which completely define the model. Training a Gaussian process consists in finding the optimum values of the hyperparameters, which are inferred from the data.

Unlike neural networks, a Gaussian process does not require training and testing and does not need to create unnecessary submodels. Details of the Gaussian process method can be found elsewhere [85] but a brief description is given here.

Notation

The notation used in the following demonstration needs to be explained beforehand:

- $P(A)$ is the "prior probability" of event A.
- $P(A|B)$, also called likelihood, is the "conditional probability" of event A, given event B.
- $P(A, B)$ or P(A $\cap$ B) is the "joint probability" of event A and B.
- Bold characters $\mathbf{X_N}$ represent vectors.
- $\mathbf{C_N}$ represents a matrix, $\mathbf{C_N^T}$ the transpose and $\mathbf{C_N^{-1}}$ the inverse matrix.

Bayes' theorem

Two rules of probability that will be used later are useful to state. First the basic rule of conditional probability, which gives the probability of obtaining

both events A and B is the product of one of the event times the conditional probability of obtaining the other event, given the first event has occurred:

$$P(A, B) = P(A|B)P(B) \tag{3.9}$$

Bayes' theorem gives the probability of a condition, given by the product of the prior probability and the likelihood:

$$P(A|B) = \frac{P(B|A)P(A)}{P(B)} \tag{3.10}$$

These two relationships will be used later in the demonstration.

Theory of Gaussian process

For a set of data $D = \{\mathbf{t_N}, \mathbf{X_N}\}$ made of input vectors $\mathbf{X_N} = \{\mathbf{x_1}, \mathbf{x_2}, ..., \mathbf{x_N}\}$ and a vector of the corresponding output $\mathbf{t_N} = \{t_1, t_2, ..., t_N\}$, a Gaussian process is defined by an N $\times$ N dimensional covariance matrix $\mathbf{C_N}$. Each element C_{ij} of the covariance matrix is a function of the input vectors and the hyperparameters given under the form:

$$C_{ij} = f(\mathbf{x_i}, \mathbf{x_j}, \mathbf{\Theta}) \quad \forall\ \mathbf{x_i} \tag{3.11}$$

The training of the Gaussian process consists in finding the hyperparameters Θ so that, for a known set of data $D = \{\mathbf{t_N}, \mathbf{X_N}\}$, it is possible to calculate the new output $\mathbf{t_{N+1}}$ for every new input $\mathbf{t_N}$. The prediction is given under the form of a mean value $\hat{t}$ and a standard deviation $\sigma_{\hat{t}}$.

The joint probability distribution of the N outputs in the database $D = \{\mathbf{t_N}, \mathbf{X_N}\}$ given the N inputs is:

$$P\left(\mathbf{t_N}|\mathbf{X_N}\right) \tag{3.12}$$

For the new value $\mathbf{t_{N+1}} = (\mathbf{t_N}, t_{N+1})$, whose corresponding input is $\mathbf{x_{N+1}}$, the joint probability distribution of both the N data points and the single new point is:

$$P(t_{N+1}, \mathbf{t_N}|\mathbf{x_{N+1}}, \mathbf{X_N}) \tag{3.13}$$

Given that we know the corresponding input vector $\mathbf{x_{N+1}}$ and the data

$D = \{\mathbf{t_N}, \mathbf{X_N}\}$, the probability distribution over the predicted point is:

$$P\left(\mathbf{t_{N+1}}|\mathbf{x_{N+1}}, D\right) \tag{3.14}$$

It can be shown from the definition of the conditional probability (3.9) and from [86] that the relationship between (3.12), (3.13) and (3.14) is given by:

$$P(t_{N+1}|\mathbf{x_{N+1}}, D) = \frac{P(t_{N+1}, \mathbf{t_N}|\mathbf{x_{N+1}}, \mathbf{X_N})}{P\left(\mathbf{t_N}|\mathbf{X_N}\right)} \tag{3.15}$$

To evaluate $P(t_{N+1}|\mathbf{x_{N+1}}, D)$, a form of joint probability distribution must be chosen beforehand and the Gaussian process specifies that it is a multivariate Gaussian [87–89]:

$$P(t_N|\mathbf{X_N}, \boldsymbol{\Theta}) \propto \exp\left[-\frac{1}{2}\left(\mathbf{t_N} - \boldsymbol{\mu}\right)'\left(\mathbf{C_N}\right)^{-1}\left(\mathbf{t_N} - \boldsymbol{\mu}\right)\right] \tag{3.16}$$

where $\boldsymbol{\mu}$ is the mean value, $\mathbf{C_N}$ the covariance matrix defined by (3.11) and $\boldsymbol{\Theta}$ the hyperparameters.

For N+1 variables, (3.15) can be rewritten:

$$P(t_{N+1}|\mathbf{x_{N+1}}, D) = \frac{1}{Z}\exp\left[-\frac{\left(t_{N+1} - \hat{t}_{N+1}\right)^2}{2\ {\sigma_{\hat{t}_{N+1}}}^2}\right] \tag{3.17}$$

where Z is a constant and $\hat{t}$ and $\sigma_{\hat{t}}$ are defined as follows:

$$\hat{t}_{N+1} = \mathbf{k}_{\mathbf{N+1}}^{\mathrm{T}}\ {\mathbf{C_N}}^{-1}\ \mathbf{t_N} \tag{3.18}$$

$${\sigma_{\hat{t}}}^2 = \mathrm{k} - \mathbf{k}_{\mathbf{N+1}}^{\mathrm{T}}\ {\mathbf{C_N}}^{-1}\ \mathbf{k_{N+1}} \tag{3.19}$$

with $\mathbf{k} = [\mathbf{C}(\mathbf{x}_1, \mathbf{x_{N+1}}), C(\mathbf{x_2}, \mathbf{x_{N+1}}), ..., C(\mathbf{x_N}, \mathbf{x_{N+1}})]$ and $k = C(\mathbf{x_{N+1}}, \mathbf{x_{N+1}})$.

$\hat{t}_{N+1}$ represents the predictive mean and $\sigma_{\hat{t}_{N+1}}$ the error bar for the prediction. Both depend on the covariance matrix $\mathbf{C_N}$ of the GP model (Equation 3.16).

Covariance and hyperparameters

The hyperparameters are defined by maximising $P(\mathbf{\Theta}|D)$, the probability of the hyperparameters given the database D. $P(\mathbf{\Theta}|D)$ can be related to $P(\mathbf{t_N}|\mathbf{X_N}, \mathbf{\Theta})$ (3.16) by using Bayes' theorem (3.10):

$$P(\mathbf{\Theta}|\mathbf{D}) = \frac{P(\mathbf{t_N}|\mathbf{X_N}, \mathbf{\Theta})P(\mathbf{\Theta})}{P(\mathbf{t_N}|\mathbf{X_N})} \tag{3.20}$$

In this particular case, the covariance between any $\mathbf{x_i}$ and $\mathbf{x_j}$ is given by $\mathbf{C}$ and can be related to the hyperparameters.

Various forms of covariance exist depending on the mode of interpolation desired. The most common form is:

$$C_{ij} = \theta_1 \exp\left[-\frac{1}{2}\sum_{l=1}^{l=L}\frac{\left(x_i{}^{(l)} - x_j{}^{(l)}\right)^2}{{r_1}^2}\right] + \theta_2 + {\sigma_n}^2\,\delta_{ij} \tag{3.21}$$

where θ_2 is a constant which corresponds to the mean value, δ_{ij} the *delta function* whose value is always 0 except when $i = j$ and σ_n the variance of the noise. r, θ_1, θ_2 and σ_n are called hyperparameters. They are optimised by maximising $P(\theta|D)$, the probability of the hyperparameters given the training data, with respect to Θ. This last operation is done numerically in the Bayesian framework.

Once the covariance is chosen and the hyperparameters optimised, the model is completely defined.

Chapter 4

Database

Following the explanation of the neural–network and the Gaussian process methods in Chapter 3, this section describes the database used to train the variety of models presented in Chapters 5, 6 and 7 and details the method for selecting inputs. There are some interesting outcomes from a study of how the output on which the model was trained can influence the predictions.

4.1 Input parameters

In modelling problems involving a large number of parameters, the ability to capture complex relationships is strongly conditioned to a well–populated database with data uniformly distributed in the input space. A large number of inputs may give more physical foundation to the model but reports from experiments do not always include the required comprehensive information. The ideal database must then be a compromise.

Data were collected from the literature, which includes published articles, irradiation experiment reports directly communicated by their authors and mechanical testing reports provided by the National Institute for Materials Science in Japan [90]. Alloys used in the database include reduced–activation ferritic/martensitic candidates such as Eurofer'97, F82H, EM10 and T91 as well as conventional 2.25, 9 or 12 wt% Cr steels. All the sources used for the training of the neural–network and Gaussian process models are listed in Appendix A.

Input variables need to be chosen carefully and include those related to

the heat treatment, the irradiation and testing parameters and the chemical composition.

Surprisingly, previous efforts to model the yield strength of irradiated steels [83] did not include the heat treatment but it has been shown that the irradiation–induced hardening between 25 and 400°C depends strongly on the tempering conditions and that the control of the microstructure through the heat treatment is a key factor in determining the resistance to irradiation–induced hardening [91]. The heat treatment is also definitely known to be important in determining the physical properties of creep–resistant steels [92]. It is therefore necessary to take account of the full pre–irradiation heat treatment, which includes the normalising temperature and time (respectively T_γ in K and t_γ in min) and the tempering temperature and time (T_T and t_T) as an input in the analysis.

Variables associated with the irradiation parameters are those which are the most commonly reported. They include the irradiation dose in dpa, the helium concentration and the irradiation and tensile testing temperature temperatures in Kelvin. As a convention, the irradiation dose and helium concentration for unirradiated steels were set to zero and the irradiation temperature to 298 K. Other parameters like the irradiation time and the damage rate would be useful to include but are seldom reported.

Previous databases for neural network models of irradiated steels [83, 84] listed 31 solutes. In the present case, that number was reduced to 14. Major solutes or those whose effects are particularly studied are systematically reported but concentrations of tramp elements (Mg, Ce, Pb, Zr, *etc.*) or others considered impurities, or present at trace levels are not often measured nor reported in irradiation studies. By default, in [83] and [84], the concentration of a missing element was set to zero when it is a deliberately added element and to the average value of available data when considered an impurity.

Moreover, impurity elements significantly increase the computing time as models need to be more complex to cope with the extra parameters. Such elements are also often not relevant in explaining variations in the output and their influence has not explicitly been studied or explained. For all those reasons, the number of elements was limited to 14 (Table 4.1).

The case of boron is different and requires an explanation. Boron is

an element which readily transmutes into helium when exposed to neutrons (Equation 2.4). In a classical low–activation steel, boron is considered an impurity and is detrimental to the stability of the alloy and its concentration is kept as low as possible for obvious reasons. However, it is, alongside nickel, often used to artificially dope alloys and produce large quantities of helium and hydrogen in order to study the effects of gas–induced swelling. In that case, boron, whose concentration is typically only a few parts per million, does not itself have an influence on the mechanical properties but transmutes rapidly into helium. After 1.6 dpa, 99 % of the boron is likely to have been transmuted and hence has disappeared [93].

The boron concentration is reported only when it is used as a doping element but mostly ignored when it is not a deliberate addition. In that case, its contribution is taken into account by the model through the overall helium concentration which is a measure of the combined effect of the helium produced in the plasma and through transmutation.

It is also possible to use artificial input parameters in order to introduce more physics in the model. They can be a combination or a function (square root, logarithm, exponential, *etc.*) of pre–existing elements, based on some physical justification.

Such parameters can be Arrhenius expressions ($\exp\left[\frac{-Q}{k_B T}\right]$) in order to take account of any thermally activated relations during the heat treatment. k_B is the Boltzmann's constant, T the temperature in Kelvin and Q is the activation energy for self–diffusion of iron in γ–iron and α–iron, respectively 286 000 and 240 000 J mol^{-1} for the austenitisation and the tempering [94, p. 12] [95].

The logarithm of the normalising and tempering time ($\ln(t_{normalising})$ and $\ln(t_{tempering})$) can help the model realise that kinetic phenomena often vary logarithmically with time [96]. In some cases, it has been proven that including the logarithm of the time was the only way to create a model that captures correctly the dependancy of the amount of retained austenite on time [97].

Finally, the database includes the square root of the displacement–per–atom ($\sqrt{\text{dpa}}$) because this quantity is related to the nucleation rate of the helium bubbles [98].

Those extra parameters do not replace the original ones but are added to them. They can only help the model find new complex relationships but will not penalise it as they are given a low significance if they are not relevant.

The complete list of inputs can be found in Tables 4.1 and 4.2.

4.2 Output

In some cases, physics imposes a condition on the output but the mathematical function inferred during the regression can find relationships which do not respect that condition. For the elongation or yield strength of irradiated steels, the output can strictly only be positive but a neural network model is a mathematical function which is not bound by this condition. Here, two options which can limit the output to the positive domain of numbers are considered: a logarithmic and a double logarithmic function.

In previous work on the volume fraction of retained austenite (V_γ) in cast iron [99], a neural network was trained on a double logarithmic function of the volume fraction, *i.e.* the model was trained on $\ln(-\ln(V_\gamma))$, instead of V_γ directly. This assumption is theoretically justified for transformation kinetics and is consistent with Avrami theory for the kinetics of solid–state transformation [100–102] which establishes that the volume fraction V_γ varies with $1 - \exp(-k_A t^n)$ where k_A and n are constants and t is the time. In that case, $\ln[-\ln(1 - V_\gamma)]$ varies with $n \ln(t)$. The volume fraction is then confined between 0 and 1. In the case of yield strength for example, a similar expression would be:

$$\sigma' = \ln\left(-\ln\left(\frac{\sigma - \sigma_{min}}{\sigma_{max} - \sigma_{min}}\right)\right) \tag{4.1}$$

where σ is the original output, σ' is the modified output used for the training, σ_{max} the maximum value for the yield strength and σ_{min} equal to 0 MPa, the lowest value physically possible.

The only constraint for σ_{max} is that it must be superior to the maximum strength in the database but there is no justification to choose a particular

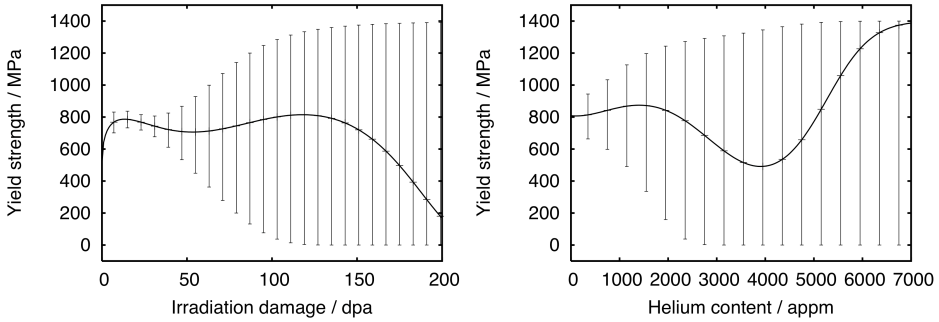

(a) Irradiation dose (b) Helium content

Figure 4.1: Predictions of the yield strength of as a function of the irradiation dose (a) and the helium content (b). The plotting of modelling uncertainties is restricted to 0 and 1400 MPa.

value. To prove that the choice of σ_{max} influences the calculation, two models were created with two different values of σ_{max}, 1400 and 1600 MPa. In each case, σ_{min} was set to 0 MPa.

Figures 4.1 and 4.2 show the calculated yield strength as a function of the irradiation dose and the helium concentration for the two models described above. The calculations have been deliberately extrapolated to explore areas where modelling uncertainties are very large.

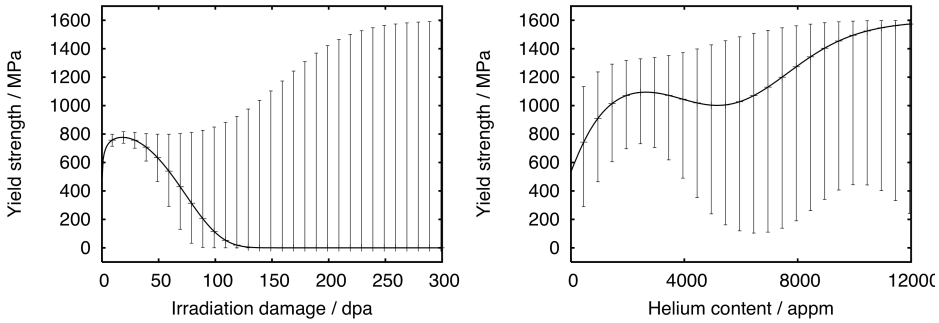

(a) Irradiation dose (b) Helium content

Figure 4.2: Predictions of the yield strength of as a function of the irradiation dose (a) and the helium content (b). The plotting of modelling uncertainties is restricted to 0 and 1600 MPa.

It appears that modelling uncertainties, and as a consequence the mean val-

ues, are confined to the interval 0–1400 MPa in the first case (Figure 4.1) and 0–1600 MPa in the second case (Figure 4.2), which correspond to the values chosen for σ_{min} and σ_{max}.

The use of a logarithm function and the arbitrary choice of σ_{min} and σ_{max} are the reason of that behaviour. The network is trained on σ' and the calculated σ' needs to be retransformed to give the real yield strength. Equation 4.1 is then equivalent to:

$$-\exp(\sigma') = \ln\left(\frac{\sigma - \sigma_{min}}{\sigma_{max} - \sigma_{min}}\right) \tag{4.2}$$

and the term on the left $-\exp(\sigma')$ being strictly negative implies that the argument of the logarithm is smaller than 1:

$$\left(\frac{\sigma - \sigma_{min}}{\sigma_{max} - \sigma_{min}}\right) < 1 \Longleftrightarrow \sigma_{min} < \sigma < \sigma_{max} \tag{4.3}$$

The final yield strength σ is thus bounded by σ_{min} and σ_{max}, which is chosen before training. Moreover, the model predicts a mean value σ' and error bars (σ' - error, σ' + error) which are symmetrical in the logarithmic space. After retransformation, those error bars become asymmetrical, forcing the mean value σ to converge towards one of the extrema, σ_{min} or σ_{max}.

Using the hypothesis postulated in [99] and training the model on a double logarithmic function of the output induces an upper and a lower limit for the predicted values and hence biases the model. This is particularly evident and problematic when extrapolating over long ranges, as it is the case when data relative to fission are extrapolated to fusion conditions.

A simple logarithm was used in other work. In [103], a model of the creep strength of austenitic stainless steels was trained on the logarithm of the rupture life instead of the rupture life itself. This assumption can be physically justified because the rupture life cannot be negative and tends to increase when the stress decreases, being in theory infinite when the stress tends to zero. These justifications are consistent with the use of a logarithmic function.

In a previous neural–network model of the yield strength of irradiated steel [83], the network was also trained on a logarithmic value in order to

avoid negative predictions for the yield strength, allow the simplification of some derived inputs and ease the capture of some power law dependancies. However, in that particular case, the use of a logarithmic function allows the yield strength to tend to an infinite value, which cannot be physically justified.

It appears that there is no justification for the use of a bounding function on the output in the database. In the next chapters, the models were only trained on raw values of the output.

4.3 Conclusions

In subsequent work, all models in Chapters 5, 6 and 7 are trained on the output directly and the complete list of parameters and artificial parameters selected for the database is given in Tables 4.1 and 4.2.

Parameter
Austenitisation temperature (T_γ) / K
Austenitisation time (t_γ) / min
Tempering temperature (T_T) / K
Tempering time (t_T) / min
C / wt%
Cr / wt%
W / wt%
Mo / wt%
Ta / wt%
V / wt%
Si / wt%
Mn / wt%
N / wt%
Cu / wt%
Nb / wt%
Ni / wt%
P / wt%
Ti / wt%
Irradiation temperature / K
Irradiation dose / dpa
Helium / appm
Test temperature / K

Table 4.1: List of parameters selected for database.

Parameter	Comment
$\exp\left(\frac{-Q}{k_B T}\right)$	Thermally activated processes during the normalising and tempering.
$\ln(t_{normalising})$	Logarithmic variation of kinetic phenomena with time (normalising and tempering).
$\sqrt{\text{dpa}}$	Quantity related to the nucleation rate of the helium bubbles

Table 4.2: List of artificial parameters.

Chapter 5

Elongation

Previous artificial neural networks of the yield strength [83] and the ductile–to–brittle transition temperature [84] have been published and were used to estimate the mechanical properties of irradiated steels in fusion conditions. They have highlighted the role of certain inputs such as the chromium concentration, the irradiation temperature and the helium–to–dpa ratio and have confirmed that 9 wt% Cr alloys show the best resistance to irradiation.

In this chapter, an attempt was made to develop an experience–based quantitative model of the elongation of neutron–irradiated steels using the neural network method. The design of the model is described and, to test its efficiency, predictions were compared to experimental values and were found to be in agreement. The model was extrapolated to fusion conditions, *i.e.* high irradiation doses (200 dpa) and temperatures (750°C). Because of the lack of experimental data at such doses and temperatures, predicted values were naturally accompanied with very large modelling uncertainties. The role of chromium, known to be a key element in low–activation steels, was evaluated and it appeared that, although being important in the control of the resistance to irradiation–induced hardening, no major effect can be observed when only the elongation is considered.

5.1 Elongation of irradiated steels

Tensile elongation is controlled by many factors, including details of the structure (atomic and microstructure, inclusions), plasticity (work–hardening

coefficient as a function of strain, homogeneity of deformation, strain rate, temperature) and size effects. Several mechanisms are activated to explain its evolution under irradiation.

When exposed to neutrons, irradiated samples accumulate defects and transmutation products (primarily helium but also hydrogen) which interact with dislocations pre-existing in the matrix. Neutron–irradiation at high temperature induces a high density of Franck loops in the matrix [104]. Interactions between defects and dislocation barriers lead to a loss of work hardening which results in an increase in the yield strength and a decrease in the elongation. An additional loss of work hardening is associated with dislocation channelling [104].

The irradiation dose and temperature directly influence the elongation, which usually decreases within the first moments of the irradiation as the concentration of defects increases. Above a certain dose, defects reorganise in dislocations, loops and dislocation networks. A saturation in hardening and in the reduction of the elongation appear during the transition from loop nucleation to loop growth; the elongation then reaches a minimum and remains at this value or slightly increases again, depending on the metallurgical and irradiation conditions [10] (Figure 5.1).

Since the late 1950s, empirical models have been proposed to more or less successfully model the effects of irradiation on the mechanical properties of steels [105–107] but none has been proposed for the elongation of irradiated steels. It is not possible to calculate elongation from first principles and yet such information is essential. Empirical [108] and neural–network [109] models of the elongation have already been published but only in the case of welding.

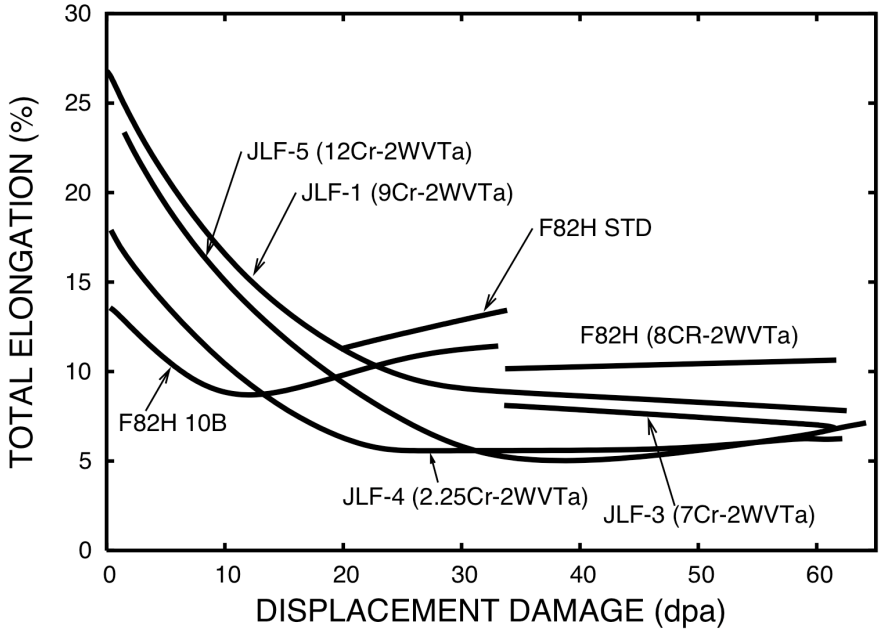

Figure 5.1: Examples of the response to irradiation of the elongation of different reduced–activation ferritic/martensitic steels to irradiation [31]. Irradiation was carried out at 683 K. The elongation of 7Cr–2WVTa, 9Cr–2WVTa and 12Cr–2WVTa continuously decreases as the irradiation dose increases whereas that of F82H 10B, 2.25Cr–2WVTa and 12Cr–2WVTa reaches a minimum at respectively 10, 25 and 40 dpa.

An attempt is made here to develop an experience–based quantitative model for the elongation of irradiated steel using the neural network method. The database needed to do this is discussed in the next section.

5.2 Database

The database was built according to the recommendations in Chapter 4 and elongation values from 408 irradiation experiments and 1155 tensile tests on unirradiated samples were compiled into an extensive set.

Table 5.1 gives the maximum, minimum, average and standard deviation for every input. Figures 5.2 and 5.3 presents the distribution in parame-

ters. They do not show any functional dependancies between inputs and the output but highlight the inhomogeneity in distribution and the existence of clusters. Some parameters are homogeneously distributed, such as phosphorus (Figure 5.3) while others, such as tungsten and chromium (Figure 5.2) are clustered. This is recognised by the Bayesian framework which associates large modelling uncertainties to domains with sparse or noisy data.

Parameter	Minimum	Maximum	Average	Standard Deviation
T_γ / K	1143	1323	1237	60
t_γ / min	10	540	67	99
T_T / K	898.15	1053	991	44
t_T / min	30	660	125	130
C / wt%	0.064	0.34	0.130	0.043
Cr / wt%	0.0001	13.6	5.5	4.2
W / wt%	0	2.17	0.44	0.74
Mo / wt%	0	1.59	0.47	0.38
Ta / wt%	0	0.14	0.02	0.04
V / wt%	0	0.31	0.09	0.12
Si / wt%	0	0.86	0.27	0.19
Mn / wt%	0	2.09	0.53	0.21
N / wt%	0	0.17	0.013	0.016
Cu / wt%	0	0.25	0.051	0.05
Nb / wt%	0	0.075	0.006	0.017
Ni / wt%	0	2.3	0.18	0.42
P / wt%	0	0.03	0.011	0.007
Ti / wt%	0	0.052	0.002	0.005
Irradiation temperature / K	293	1146	366	156
Irradiation dose / dpa	0	72	3.2	9.4
Helium / appm	0	5000	61	388
Test temperature / K	109	973	587	212
Elongation / %	0.04	105	22	15

Table 5.1: Properties of the database used to create the mathematical models. For each parameter, the minimum, maximum and average value is given with the standard deviation to give an indication of the scatter between experimental data.

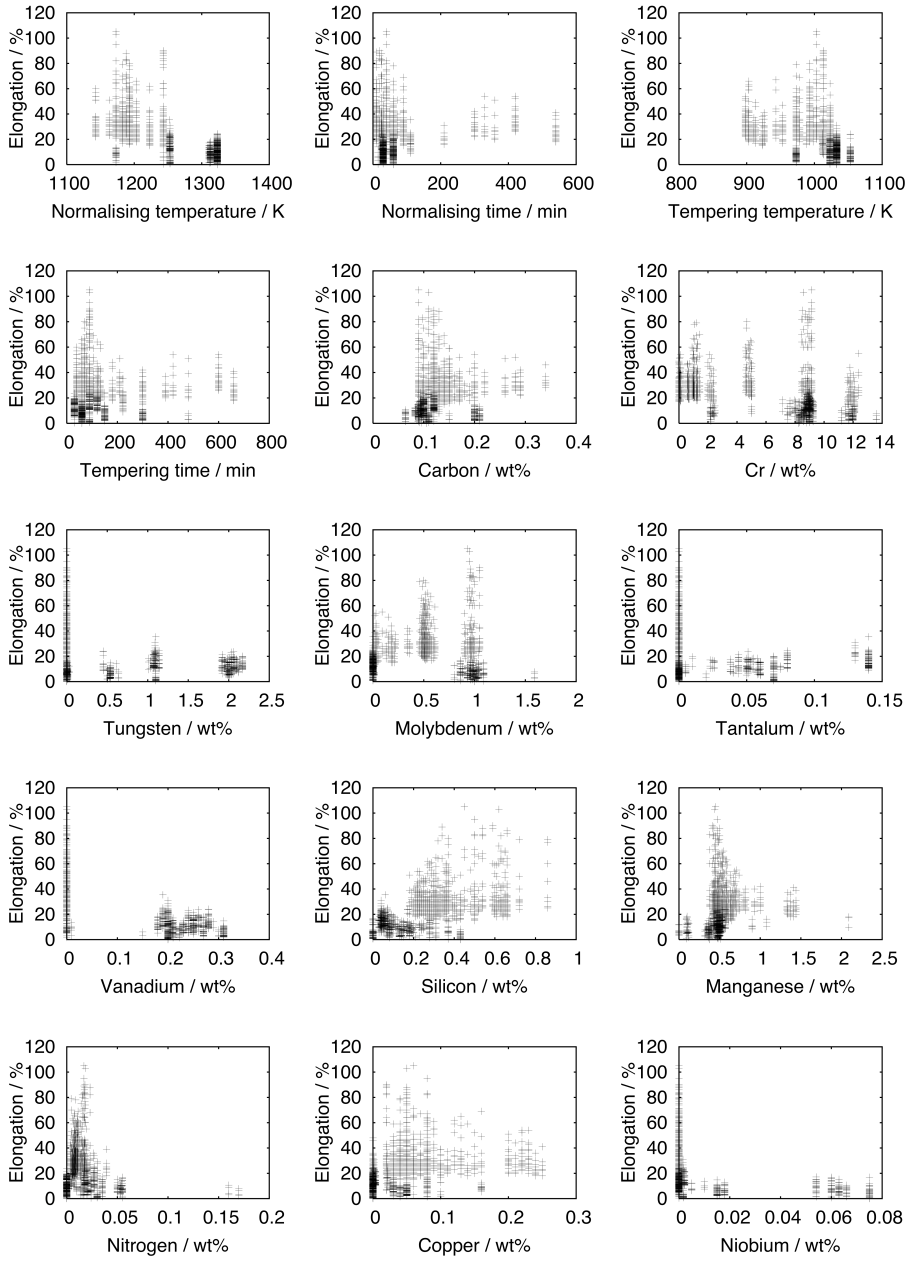

Figure 5.2: Input parameter distribution. For each specimen, the elongation is plotted as a function of the considered parameter.

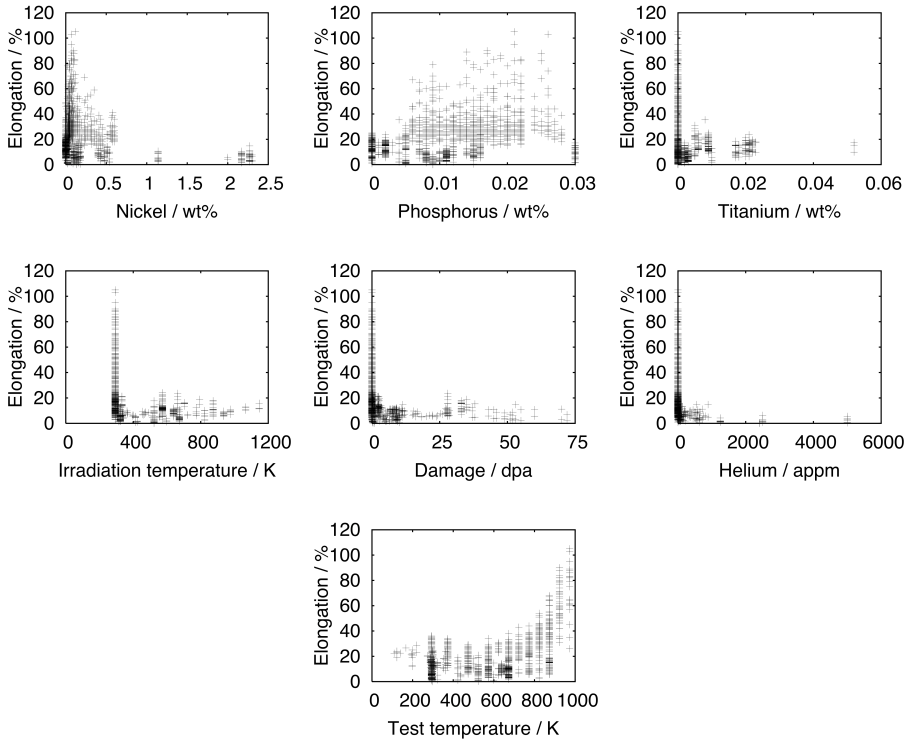

Figure 5.3: Input parameter distribution. For each specimen, the elongation is plotted as a function of the considered parameter.

5.3 Model and training

After compilation, the database was split into a training set and test set and normalised between -0.5 and +0.5. A hundred models with five different seeds and up to a hundred hidden units were created. Whereas the noise level from the training data decreases with increase complexity (Fig 5.4a), the error in predicting the test data is expected to go through a minimum when an optimum level of complexity is discovered which does not model noise, nor is it too simple to capture real trends (Figure 5.4b).

Predictions realised with the best sub–model are shown in Figure 5.4e for the testing set and Figure 5.4f for the training set. Noise and modelling uncertainties are indicated by error bars, which represent ± 1 σ. The different sub–models are ranked according to the logarithm predictive error

(Figure 5.4c) and the combined test error is calculated for committees with an increasing number of models (Figure 5.4d). The optimum committee is obtained when the combined test error is minimised. In the present case, a committee made of 19 models, has the best ability to extrapolate.

The resulting performance is illustrated in Figure 5.5 where the final committee is used to make predictions on the database itself. The correlation is good and there is a clear improvement compared to predictions by the best sub–models (Figures 5.4e and f) but there are a small number of outliers, *i.e.,* points which are are many $\pm\sigma$ away from the line of perfect fit.

For every input, it was possible to calculate a significance, which is a measure of the ability of an input to explain variations in the output, rather like a partial correlation coefficient. Figure 5.6 naturally shows that the temperature at which the tensile test is conducted is significant, but it is noteworthy that, amongst other elements, chromium is highlighted. Contrary to other models of the yield strength [83] or the ductile–to–brittle transition temperature [84], it is not possible to isolate a couple of inputs that have a major effect on the elongation.

The influence of chromium and its effect on the resistance of steels to irradiation hardening is explored in detail later in the text.

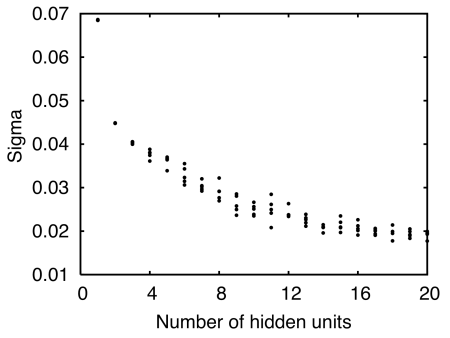

(a) Noise

(b) Test error

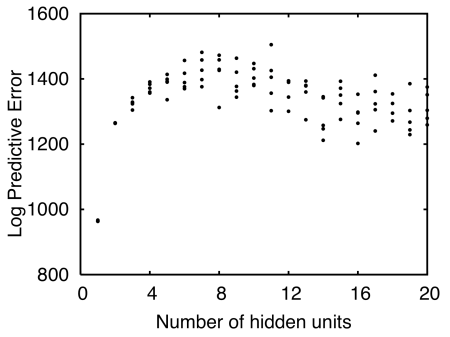

(c) Logarithmic predictive error

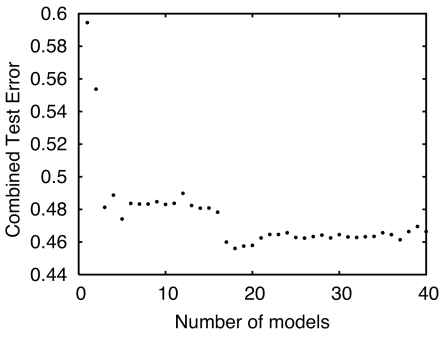

(d) Combined test error

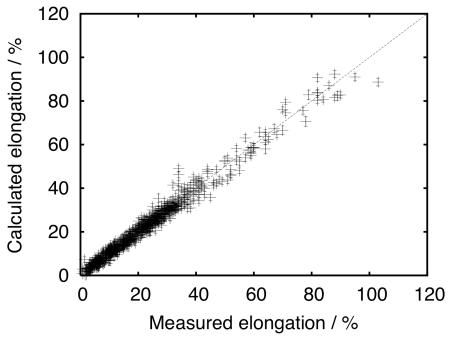

(e) Predictions for the training set

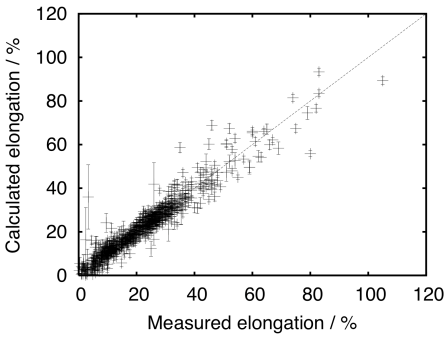

(f) Predictions for the testing set

Figure 5.4: Noise (a), test error (b) and logarithmic predictive error (c) as a function of the complexity of the model (number of hidden units). Combined test error (d) as a function of the number of models in the committee. Predictions of the best sub-model on the training (e) and testing sets (f).

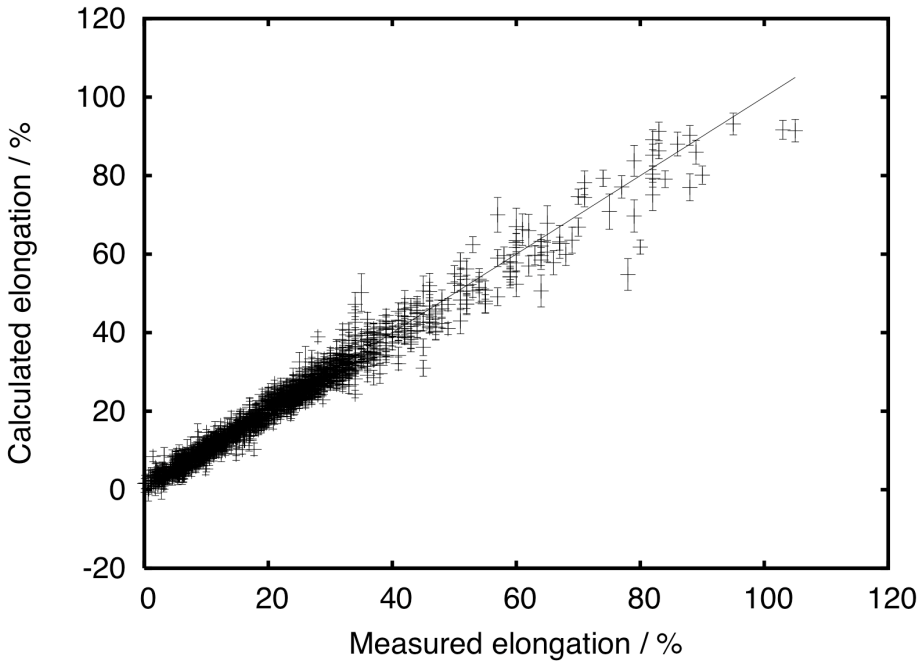

Figure 5.5: The confidence with which the optimum committee of models estimates the known data.

Figure 5.6: Significance of individual inputs. Since the committee of models contains eighteen members, there is a corresponding number of bars associated with each input. A: Normalising temperature, B: $\exp(\frac{-Q}{RT})$, C: normalising time, D: ln(normalising time) E: tempering temperature, F: $\exp(\frac{-Q}{RT})$ G: tempering time, H: ln(tempering time), I: carbon, J: chromium, K: tungsten, L: molybdenum, M: tantalum, N: vanadium, O: silicon, P: manganese, Q: nitrogen, R: copper, S: niobium, T: nickel, U: phosphorus, V: titanium, W: irradiation temperature, X: irradiation dose (dpa), Y: $\sqrt{\text{dpa}}$, Z: helium / appm, AA: test temperature (times are given in minutes, temperatures in K and composition in wt%).

5.4 Predictions

The ability of the network to model the elongation of irradiated steels was tested by making predictions for three parameters which are believed to be vital: the test temperature, the irradiation dose and the chromium concentration.

Chromium is of particular relevance because, for reasons which are not entirely clear, the extent of embrittlement of ferritic steels due to irradiation seems to go through a minimum at about 9 wt% Cr in one of the candidate steels (Eurofer'97) for the future fusion power plant project [84]. One possibility is that at large chromium concentrations irradiation leads to the precipitation of α–chromium but, as pointed out by Cottrell *et al.* [84], the situation for concentrations less than 9 wt% is not explained.

5.4.1 Test temperature

The elongation of three classical, creep–resistant chromium–containing alloys [110] with nominal concentrations: 2.25 wt% Cr, 9 wt% Cr and 12 wt% Cr was calculated in the absence of irradiation. These alloys are not reduced–activation steels but are nevertheless interesting to study because they are well–established. Their compositions and heat treatments are listed in Table 5.2.

Table 5.2: Chemical compositions in wt%. The W, Ta, V, Nb and Ti concentrations are zero.

Alloy	C	Cr	Mo	Si	Mn	N	Cu	Ni	P
2.25Cr	0.12	2.2	0.99	0.29	0.48	0.0095	0.07	0.05	0.015
9Cr	0.11	9.15	1.05	0.59	0.41	0.018	0.02	0.1	0.017
12Cr	0.12	12.38	0.09	0.48	0.71	0.0194	0.09	0.31	0.026

Alloy	T_γ / K	t_γ / min	T_T / K	t_T / min
2.25Cr	1203	60	993.15	180
9Cr	1243	20	1013.15	90
12Cr	1243	30	1023.15	60

The calculated values and associated uncertainties are plotted along-

side the measured values in Figure 5.7; the large increase in elongation at high temperatures is expected because the steels should all soften in those circumstances. This sharp change in the mechanical behaviour had been observed in [111] where a drop in the tensile strength was observed between 700 and 900 K in several creep–resistant ferritic steels and was attributed to an increased ability of dislocations to overcome obstacles with the help of thermal activation.

It is clear that the model has essentially captured the expected behaviour for temperatures below 700 K but there are discrepancies for higher temperatures. However, it is interesting to note that the elongation data themselves show that the 9Cr steel systematically has the highest elongation. To check whether this is due to the chromium concentration or other variables, the calculations were repeated by setting all the parameters other than Cr to be equal to those of the 9Cr alloy – the results then show an insignificant difference between the 9 and 12Cr steels, Figure 5.8. It is evident that the difference between the 12Cr and 9Cr alloys in Figure 5.7 cannot reasonably be attributed to their chromium concentrations alone.

The effect of irradiation at 20 and 100 dpa on the same alloys is illustrated in Figures 5.9 and 5.10. Even if there is some deterioration in elongation at 20 dpa, that at 100 dpa seems to increase, although it could be argued that the modelling uncertainties are too large to reach a confident conclusion. It is speculated that a large number of displacements per atom can cause the dissolution of precipitates introduced during the tempering heat–treatments [112], which could in principle lead to a greater elongation.

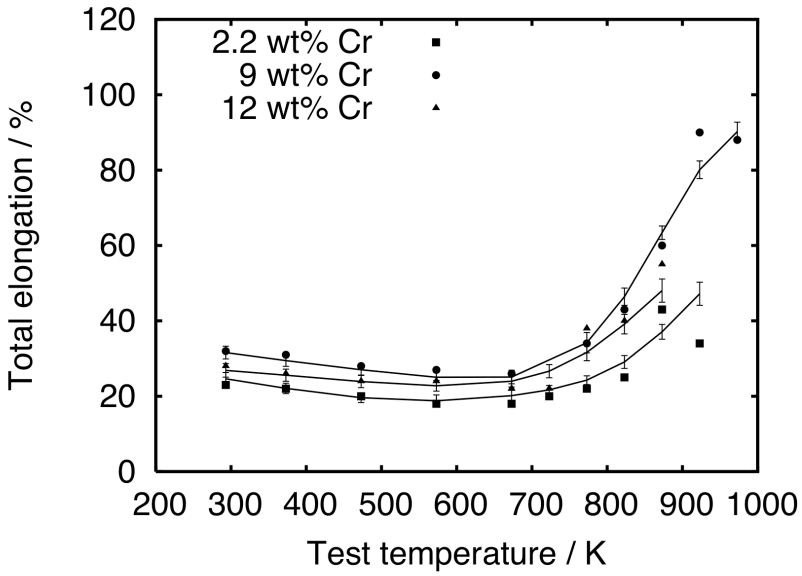

Figure 5.7: Unirradiated steels: Experimental and calculated values of elongation for steels whose parameters are listed in Table 5.2.

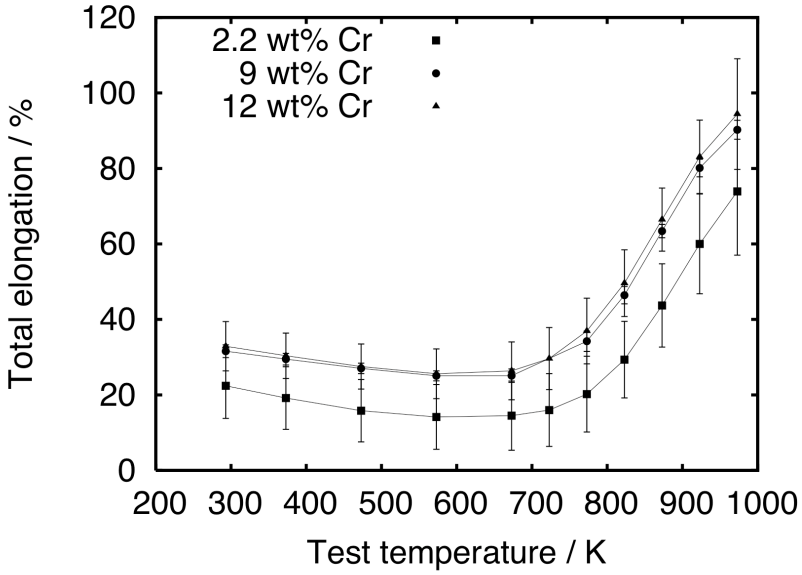

Figure 5.8: Unirradiated steels: As Figure 5.7 but with the exception of Cr, all other input parameters have been set equal to that of the 9Cr alloy.

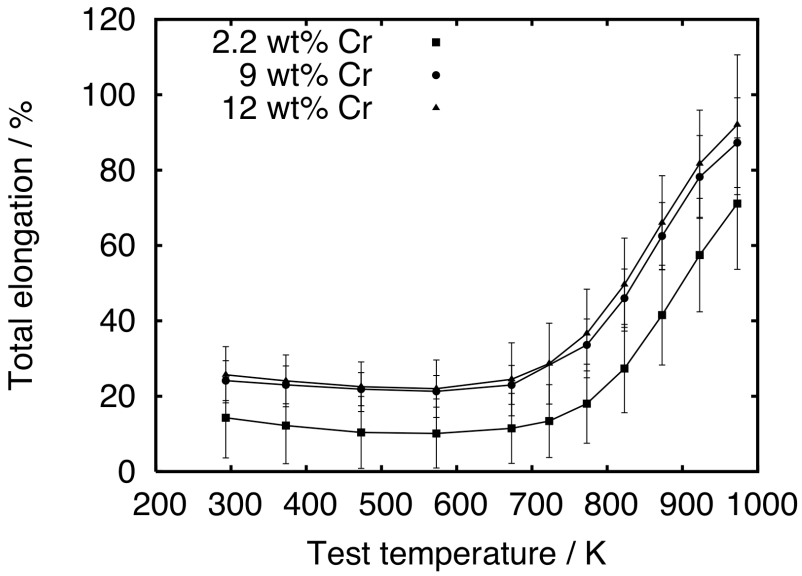

Figure 5.9: Input parameters as for Figure 5.7 but with irradiation at 20 dpa. Steels were irradiated and tested at the same temperature.

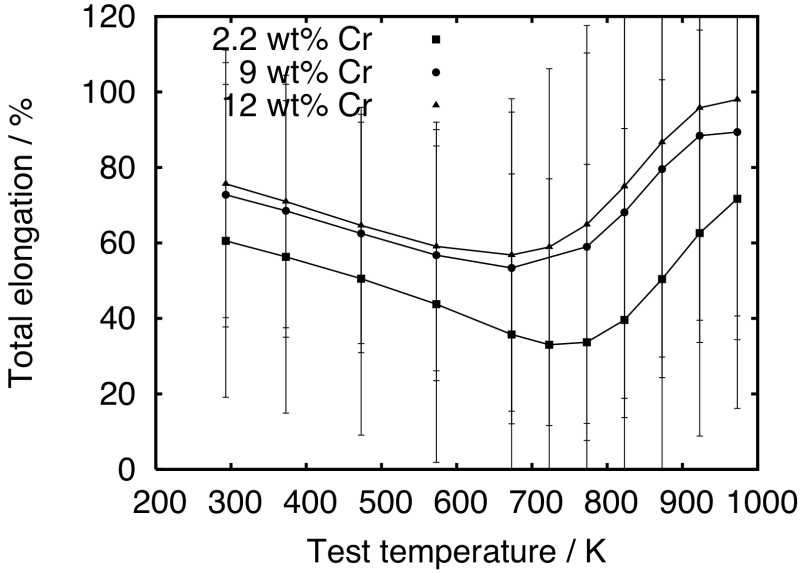

Figure 5.10: Input parameters as for Figure 5.7 but with irradiation at 100 dpa. Steels were irradiated and tested at the same temperature.

5.4.2 Irradiation dose

The calculated elongations and associated uncertainties, as a function of the displacements per atom (dpa), together with experimental data [10, 113] represented as points, are given in Figure 5.11a for three different alloys labelled 2.25Cr, 9Cr-2WVTa and 12Cr-1MoVW. The chemical compositions and heat treatments are given in Table 3.

Table 5.3: Chemical composition in wt%. The nitrogen concentration is zero.

Alloy	C	Cr	W	Mo	Ta	V	Si	Mn
2.25Cr	0.11	2.36	0	0.01	0.005	0.25	0.17	0.4
9Cr–2WVTa	0.1	8.72	2.09	0	0.075	0.23	0.23	0.43
12Cr–1MoVW	0.2	11.71	0.54	1.02	0	0.31	0.13	0.49

Alloy	Cu	Nb	Ni	P	Ti	T_γ / K
2.25Cr	0.02	0.005	0.01	0.015	0.005	1323
9Cr–2WVTa	0	0	0	0.015	0	1323
12Cr–1MoVW	0.05	0.015	2.27	0.011	0.003	1323

Alloy	t_γ / min	T_T / K	t_T / min
2.25Cr	60	973	60
9Cr–2WVTa	60	1023.15	60
12Cr–1MoVW	30	973	300

A minimum in the elongation is observed at 5–10 dpa for all the three alloys (only 2% at 10 dpa for the 12 wt% Cr alloy), followed by a recovery as the dose increases. This low elongation has previously been noted [10] and is attributed to the onset of channel deformation [24] in which dislocations sweep out defect–free channels so that subsequent deformation in these channels becomes easier, leading to heterogeneous deformation. The minimum in total elongation is explained by the growth of dislocation loops as the irradiation dose increases, making it more difficult to form channels and hence rendering deformation more homogeneous.

Figure 5.12 shows the same calculations as Figure 5.11, but with all the parameters set to be those of the 9C–2WVTa alloy with the exception of the

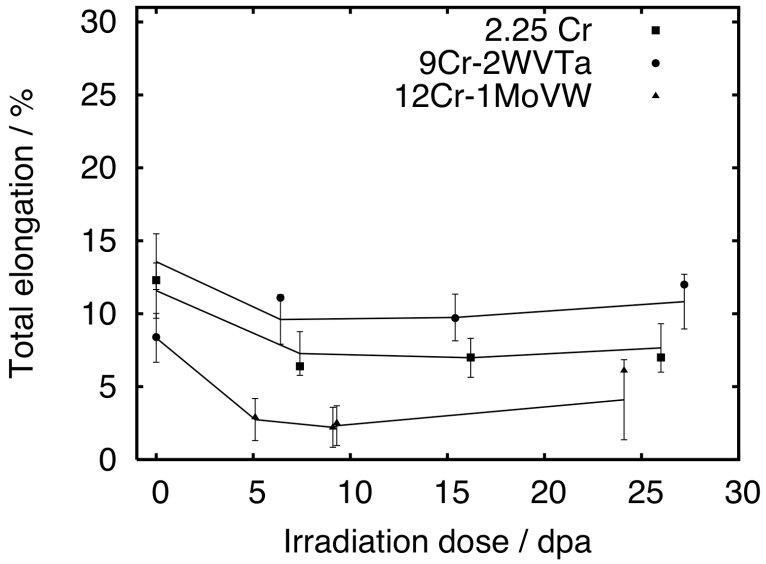

Figure 5.11: Elongation calculations for the alloys listed in Table 5.3.

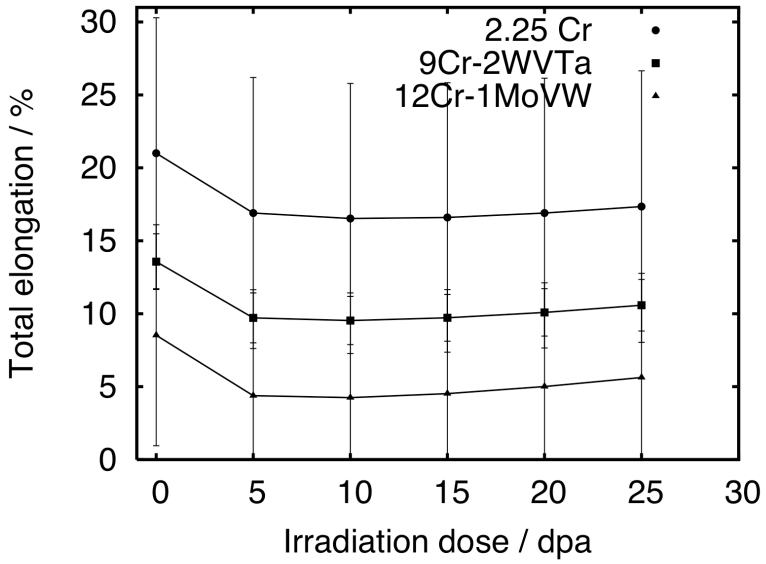

Figure 5.12: Elongation calculations for the alloys listed in Table 5.3, Cr concentrations as for Figure 5.11 but all other parameters set to be those of the 9C–2WVTa alloy.

chromium concentration which is set to the values stated in Table 3. These calculations were done to see whether the observed effects of chromium are intrinsic to that element or whether other factors play a role. It is evident that the difference between the 12 and 9Cr steels vanishes as the alloys present a minimum in elongation at 5–10 dpa for the three different chromium concentrations.

The calculation shows that the 2.25Cr alloy has a higher elongation than the 9Cr and 12Cr. This is consistent with previous work on low–chromium alloys where several chromium-tungsten steels with Cr concentrations of 2.25, 5, 9 and 12 wt% were tested and showed that when tempered at 700°C, the elongation of 2.25Cr–2W is higher than those of 9Cr–WV and 9Cr–2WVTa [114].

5.4.3 Chromium concentration

As mentioned previously, the literature suggests that 7–9 wt%Cr alloys show a lesser tendency to irradiation hardening and have a better resistance to radiation damage [31, 83]. However, here we do not find a clear optimum in chromium concentration with respect to ductility, particularly when the calculations are made with all the other variables kept constant.

Figures 5.13 and 5.14 show estimates for the Cr–2WVTa system based around the Eurofer'97 design, both for the unirradiated and irradiated states. There is no evidence to suggest that there is an advantage in keeping the chromium concentration in the range 7–9 wt%.

It is noteworthy that some of the reported observations are based on *differences* rather than absolute values, for example, ΔDBTT (the change in the ductile–brittle transition temperature relative to the unirradiated state). This may be misleading because a brittle material would be expected to have a smaller ΔDBTT even though an irradiated ductile material may have a better toughness.

5.5 Extrapolation

The work done here was primarily designed to make estimates of temperatures and irradiation doses where no experiments can be carried out for more

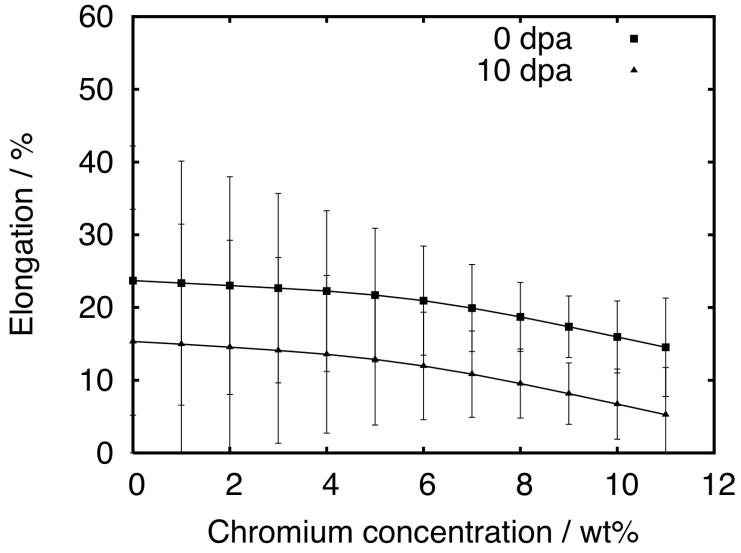

Figure 5.13: Calculated elongation for 9Cr2WVTa at two irradiation doses, 0 and 10 dpa, as a function of the chromium concentration.

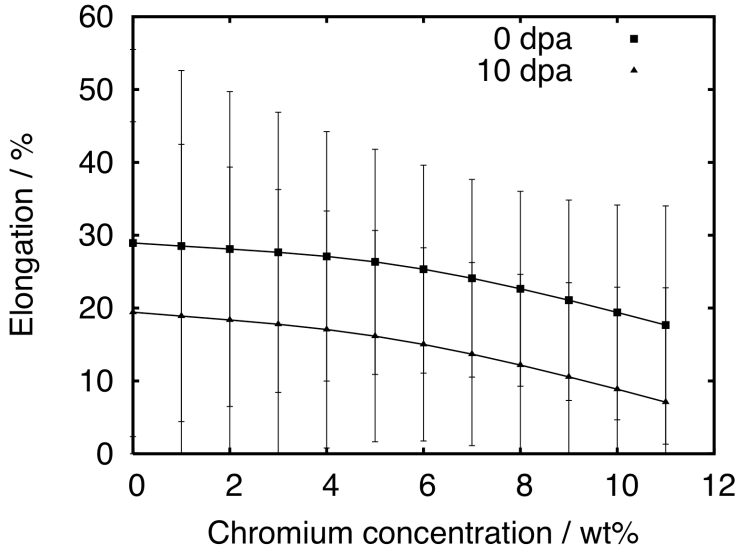

Figure 5.14: Calculated elongation for Eurofer'97 at two irradiation doses, 0 and 10 dpa, as a function of the chromium concentration.

than a decade whilst appropriate reactors are built, *i.e.* for high temperatures (900 K) and irradiation doses (200 dpa). The ability of the network to extrapolate and to indicate uncertainties is therefore important.

Elongation was calculated between 300 and 1000 K and 0 and 200 dpa for two low–activation steels: Eurofer'97 [115] and F82H [25]. The chemical compositions are given in Table 5.5; both steels had the same heat treatment: 1 h at 1323 K and 1 h at 1023 K. Figures 5.15 and 5.16 show the results.

Table 5.4: Chemical composition in wt%. The Nb and Mo concentrations are zero.

Alloy	C	Cr	W	Ta	V	Si
Eurofer'97	0.12	8.99	1.1	0.14	0.19	0.07
F82H	0.093	7.65	1.98	0.038	0.18	0.09
Alloy	Mn	N	Cu	Ni	P	Ti
Eurofer'97	0.44	0.017	0.022	0.007	0	0.009
F82H	0.49	0.002	0	0.05	0.001	0

The elongation reaches 140 and 120 % for Eurofer'97 and F82H at room temperature and 200 dpa. It reaches 60 and 32 % in fusion conditions (900 K, 200 dpa) but the associated uncertainties are large (Figures 5.15b and 5.16b).

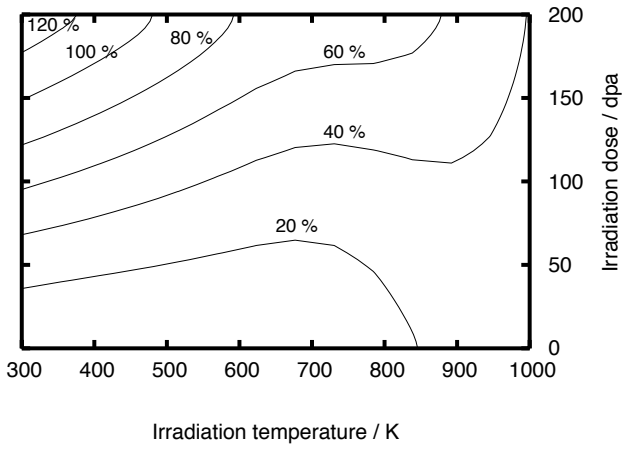

(a) Elongation

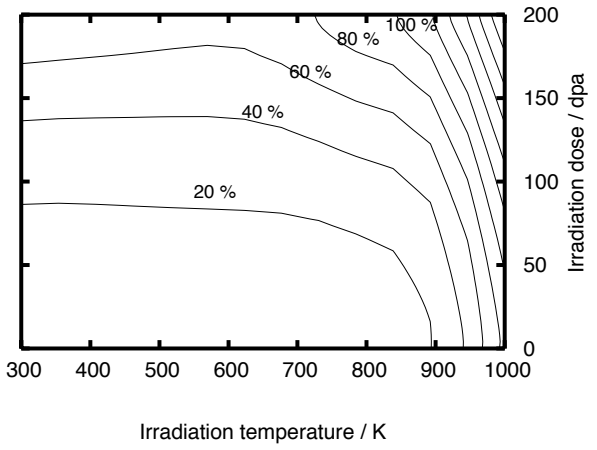

(b) Modelling uncertainties

Figure 5.15: (a) Predicted % elongation for Eurofer'97. (b) Corresponding uncertainties.

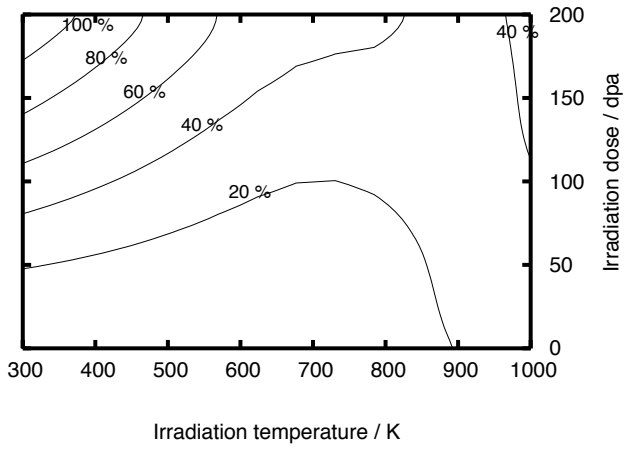

(a) Elongation

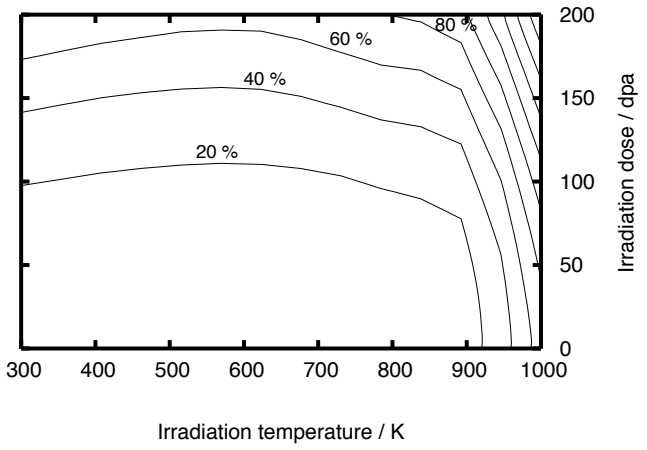

(b) Modelling uncertainties

Figure 5.16: (a) Predicted % elongation for F82H. (b) Corresponding uncertainties.

5.6 Conclusions and summary

A neural network was created to model the elongation of irradiation steels. Contrary to previous models, training the neural network on raw variables (and not a logarithmic function) does not induce an artificial bias.

The main suggestions to reduce modelling uncertainties and increase the reliability of the model in areas far from the domain of available knowledge must come from a better understanding of hardening mechanisms or the realisation of more irradiation experiments at high doses/temperatures. Better irradiation experiment reports which include parameters often neglected (such as irradiation time, flux, complete chemical composition, *etc.*) could also contribute to refining predictions. Finally, models should in normal circumstances be directly trained on the output itself rather than a bounding function of the output.

One important conclusion is that elongation *per se* is not necessarily optimised at a concentration of 9 wt% of chromium; other factors intervene to give that impression.

This neural–network model is freely available online on the Materials Algorithms Project: http://www.msm.cam.ac.uk/map/mapmain.html
Instructions for the program are given in the Appendix B.

Chapter 6

Yield strength

Neural–network models of the yield strength have been created previously [83, 116, 117] and have been used to make predictions that were in agreement with experimental measurements even if their ability to extrapolate data from fission regimes to fusion regimes was limited.

In this chapter, various models of the yield strength are presented and used to further explore the relations between irradiation and mechanical properties.

A new yield strength model that includes the heat treatment and takes account of the recommendations from Chapter 4 was created, tested and used to factorise the strength of an irradiated steel into different components, to permit the evolution of yield strength at high temperatures to be explored.

The variation in yield strength, as opposed to the yield strength itself, was modelled to highlight the role of chromium and the irradiation temperature and finally, Gaussian processes were compared to neural networks.

6.1 Yield strength model

6.1.1 Database

To create the model, 1916 experimental data were collected from the literature (Appendix A) and compiled into a database. Table 6.1 gives a list of the input parameters used in the database as well as the minimum, maximum, average value and the standard deviation for each of them. Figures 6.1 and 6.2 illustrate the spread of data.

Parameter	Minimum	Maximum	Average	Standard deviation
T_γ / K	1143	1373	1240	69
t_γ / min	4.8	540	62	92
T_T / K	898.15	1053	990	43
t_T / min	30	660	116	122
C / wt%	0.064	0.34	0.133	0.044
Cr / wt%	0.0001	13.6	5.4	4.2
W / wt%	0	2.93	0.47	0.80
Mo / wt%	0	1.59	0.46	0.40
Ta / wt%	0	0.14	0.02	0.04
V / wt%	0	0.39	0.09	0.12
Si / wt%	0	0.86	0.26	0.18
Mn / wt%	0	2.09	0.53	0.22
N / wt%	0	0.17	0.014	0.016
Cu / wt%	0	0.25	0.049	0.05
Nb / wt%	0	0.45	0.008	0.039
Ni / wt%	0	2.3	0.16	0.39
P / wt%	0	0.03	0.003	0.006
Ti / wt%	0	0.052	0.002	0.005
Irradiation temperature / K	293	1146	365	150
Irradiation dose / dpa	0	72	3.1	9.2
Helium / appm	0	5000	49	333
Test temperature / K	109	973	590	213
Yield strength / %	62	1357	434	268

Table 6.1: Properties of the database used to create the mathematical models. For each parameter, the minimum, maximum and average value is given with the standard deviation to give an indication of the scatter between experimental data.

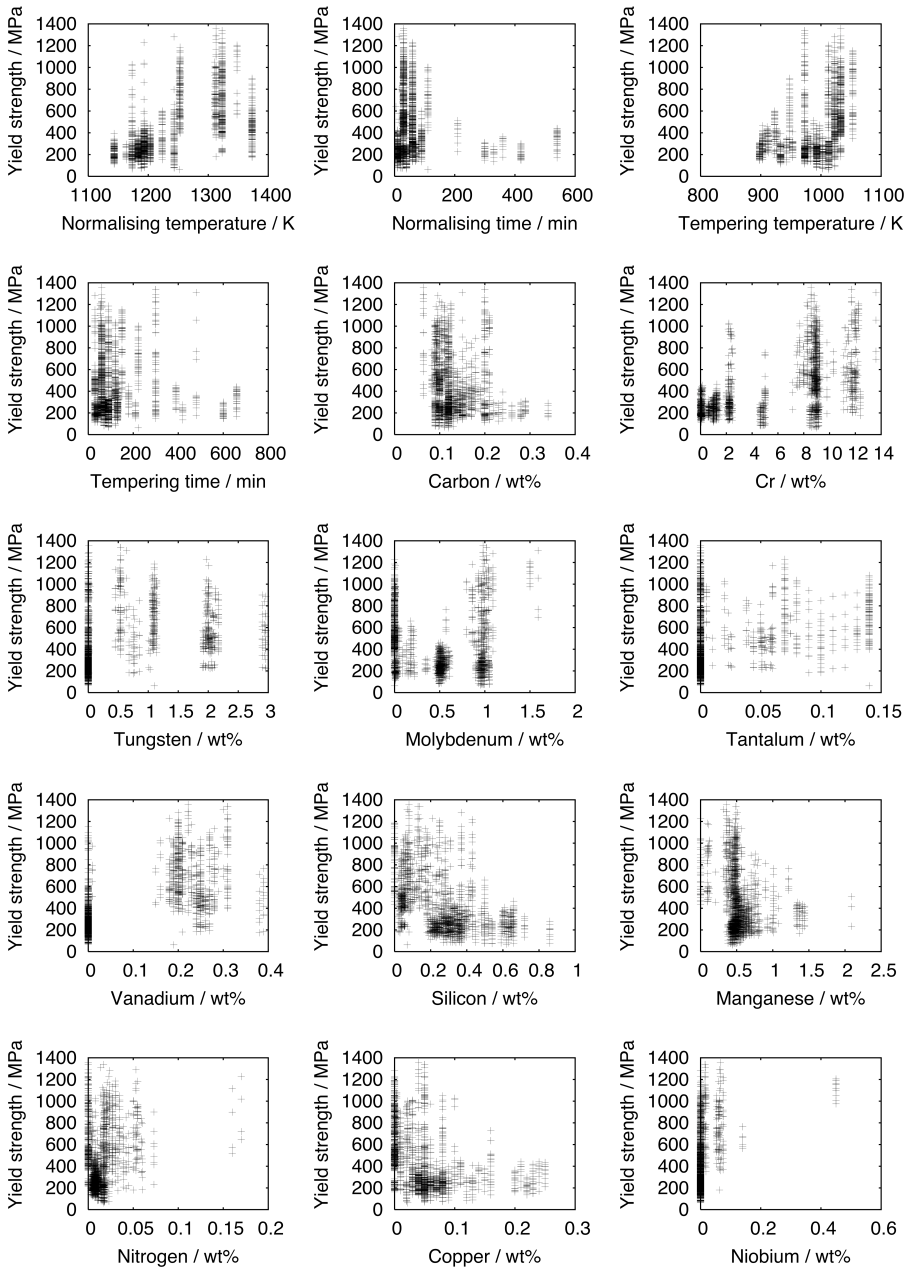

Figure 6.1: Input parameter distribution. The yield strength is plotted in each case as a function of the considered parameter.

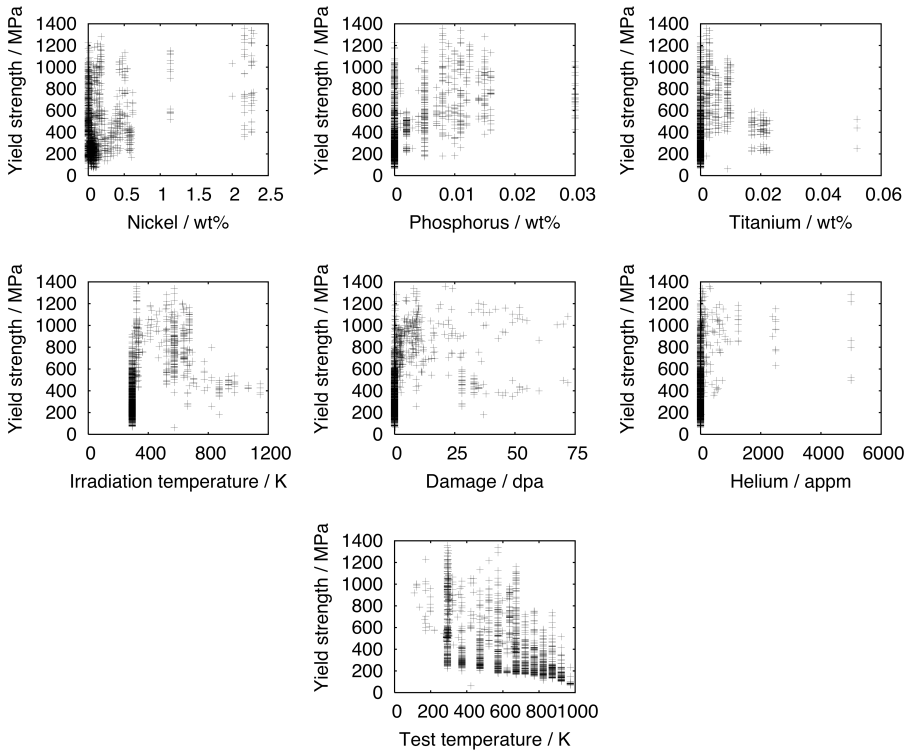

Figure 6.2: Input parameter distribution. The yield strength is plotted in each case as a function of the considered parameter.

6.1.2 Model and training

The theory underlying neural networks is given in Chapter 3 and the procedure followed is the same as in Chapter 5, taking account of recommendations from Chapter 4. The training is only briefly described here.

The database was partitioned into a training and a testing set. 100 models were trained on the first set and tested on the latter. The perceived level of noise decreases with complexity (Figure 6.3a) but the test errors reaches a minimum at 5 hidden units (Figure 6.3b). Models with the best performances were ranked according to their LPE (Figure 6.3c) and an optimum committee of 19 models was found by minimising the CTE (Figure 6.3d). After retraining, the final committee was tested by doing predictions on the database itself (Figure 6.5). Some outliers can be observed but the fit is generally good. The significance of each parameter is given in Figure 6.4.

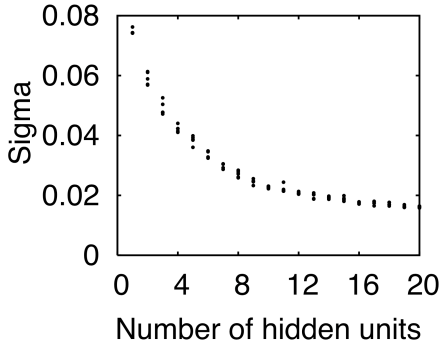

(a) Noise

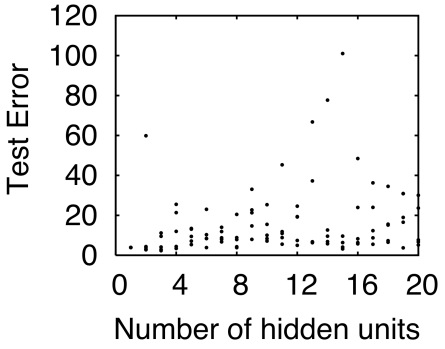

(b) Test error

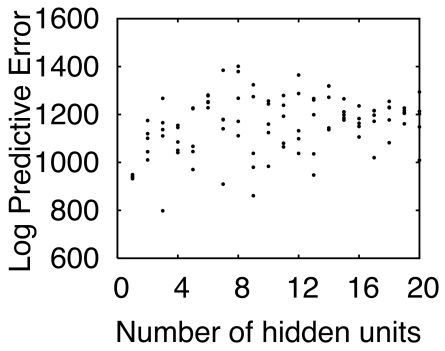

(c) Combined test error

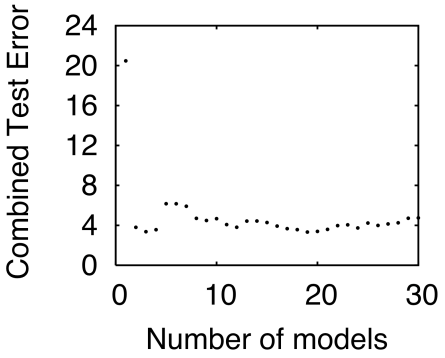

(d) Logarithmic predictive error

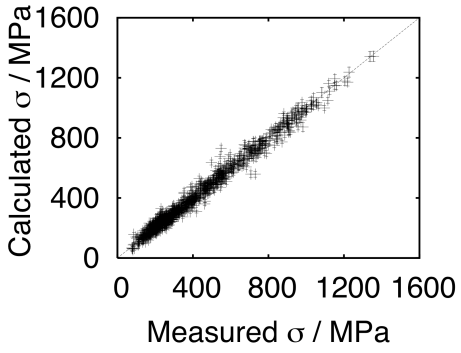

(e) Predictions for the training set

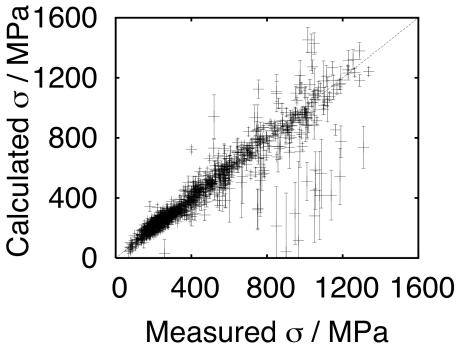

(f) Predictions for the testing set

Figure 6.3: Noise (a), test error (b) and logarithmic predictive error (c) as a function of the complexity of the model (number of hidden units). Combined test error (d) as a function of the number of models in the committee. Predictions of the best sub-model on the training (e) and testing sets (f).

Figure 6.4: Significance of individual inputs. Since the committee of models contains eighteen members, there is a corresponding number of bars associated with each input. Times are given in minutes, temperatures in K and composition in wt%. A: Normalising temperature, B: $\exp(\frac{-Q}{RT})$, C: normalising time, D: ln(normalising time) E: tempering temperature, F: $\exp(\frac{-Q}{RT})$ G: tempering time, H: ln(tempering time), I: carbon, J: chromium, K: tungsten, L: molybdenum, M: tantalum, N: vanadium, O: silicon, P: manganese, Q: nitrogen, R: copper, S: niobium, T: nickel, U: phosphorus, V: titanium, W: irradiation temperature, X: irradiation dose, Y: $\sqrt{\text{dpa}}$, Z: helium / appm, AA: test temperature.

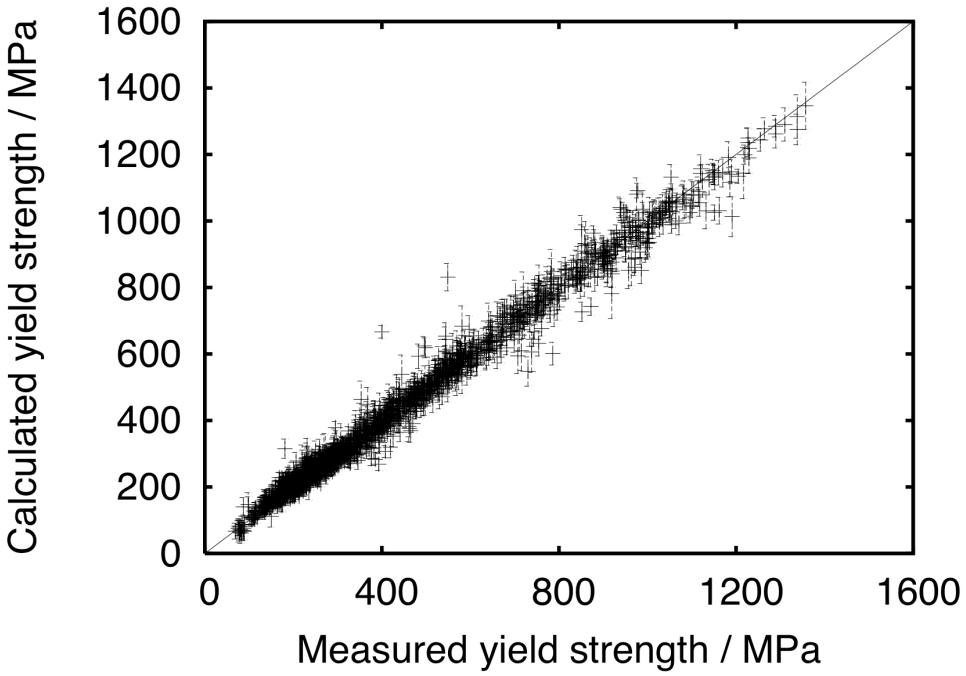

Figure 6.5: Test of the model on the database.

6.1.3 Prediction

Similarly to the elongation (Chapter 5), the model was tested for steels with three different chromium concentrations: 2.25, 9 and 12 wt% Cr. The composition and heat treatment are similar to the ones in Chapter 5 Section 5.4.2.

The behaviour of the alloys was captured by the model (Figure 6.6). Experimental values (included in the initial database) were correctly predicted by the network.

6.1.4 Extrapolation

The model described in the previous section was only explored in extrapolation mode here, with sets of inputs that simulate fusion conditions for two low-activation alloys: Eurofer'97 and F82H. For both alloys, the yield

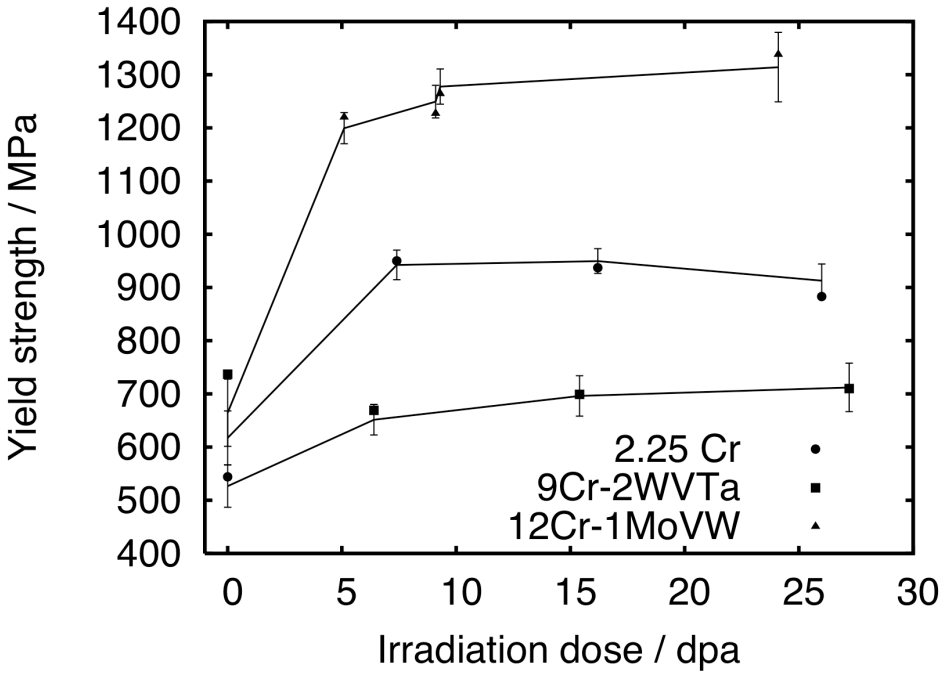

Figure 6.6: Calculated yield strength for alloys with three different chromium concentrations.

strength was calculated at irradiation doses and temperatures reaching respectively 200 dpa and 1000 K.

Eurofer'97 and F82H

The yield strength was predicted for Eurofer'97 and F82H for irradiation doses up to 200 dpa and irradiation at temperatures up to 1000 K. Predictions and modelling uncertainties are presented in Figures 6.7, 6.8, 6.9 and 6.10. Chemical compositions can be found in Tables **??** and **??**. Both alloys were normalised 1 h at 1323 K and tempered 1 h at 1023 K.

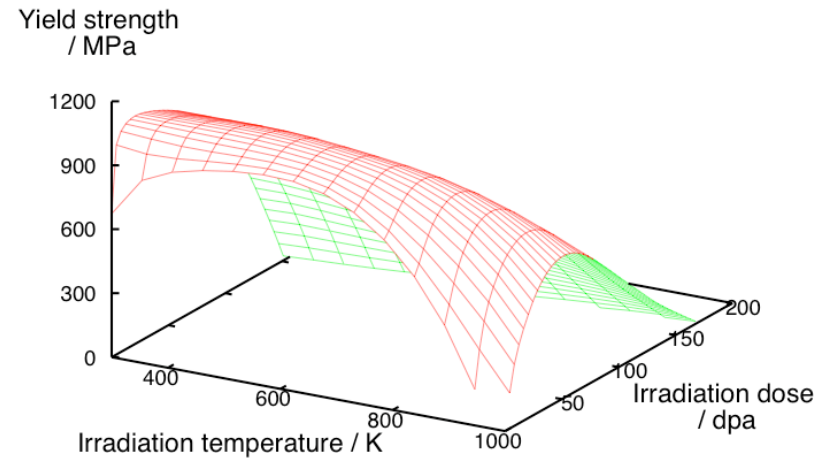

Figure 6.7: Predictions for Eurofer'97 in fission and fusion conditions.

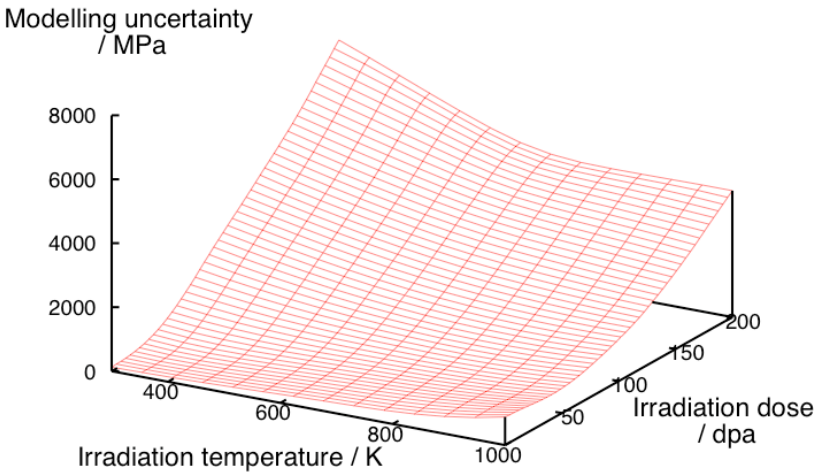

Figure 6.8: Modelling uncertainties for Eurofer'97 in fission and fusion conditions.

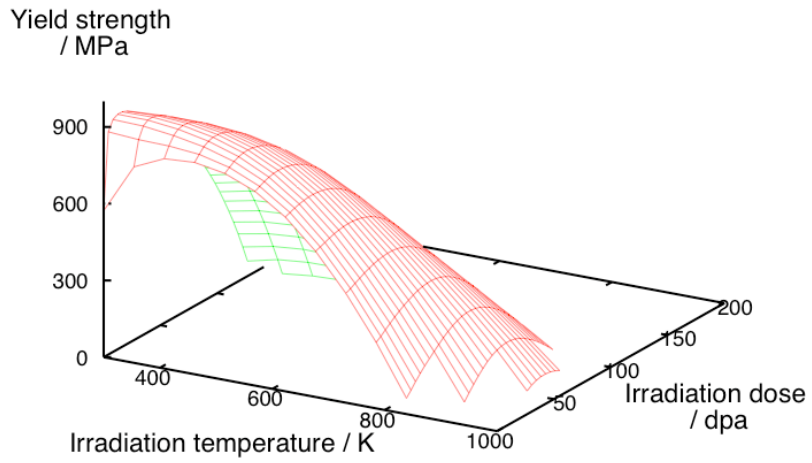

Figure 6.9: Predictions for F82H ranging in fission and fusion conditions.

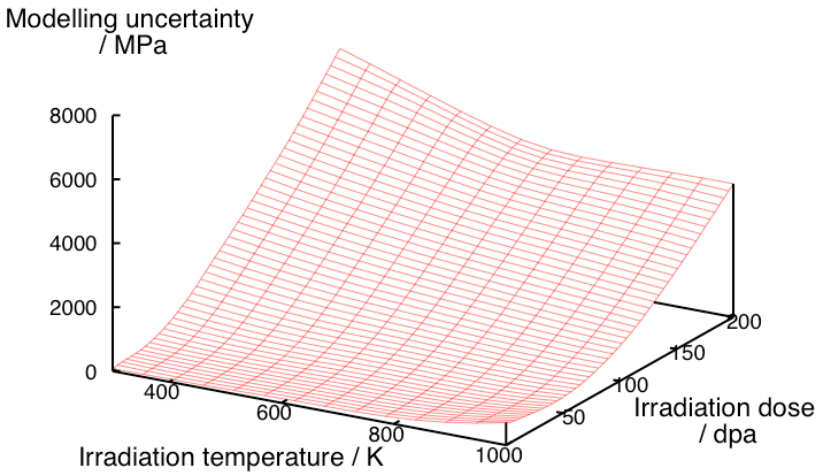

Figure 6.10: Modelling uncertainties for F82H in fission and fusion conditions.

Discussion

Bearing in mind the uncertainties, the estimation of strength seems reasonable for doses below 50 dpa and temperatures below 700–800 K, corresponding to domains of inputs where experimental data are available. When extrapolating beyond these domains, the modelling uncertainties naturally become larger.

For both alloys, the mean value of the prediction increases at a given temperature until a saturation level of stress is observed, which is consistent with experimental data. The strength then continuously decreases. This calculated trend is the opposite of the one predicted in the earlier model of the yield strength which did not contain the heat treatment as inputs [83].

Until hardening mechanisms at higher doses are better understood or irradiation experiments are carried out at doses above 100 dpa, it is not possible to reach a conclusion on the hypothetic value of the yield strength of an irradiated material in a fusion environment.

However, it is noteworthy that the trends for the yield strength are in agreement with the elongation model (Chapter 5) which predicted an increase in the ductility at high doses and temperatures.

6.2 Interpretation of the strength

The strength of a steel can be interpreted as the sum of different components: the strength of pure iron itself, the solid solution strengthening due to alloying elements and a contribution from carbides [118]. A contribution from the irradiation–induced hardening can also be added. This method and the neural network presented in the previous section were used to describe some aspects of the yield strength of steel irradiated at high temperature. The method was used for 9Cr-1Mo [119], a low–activation steel.

6.2.1 Method

It is common practice to decompose the strength σ of a steel as a function of contributions from its alloying elements:

$$\sigma = A + a \text{ wt\%Cr} + b \text{ wt\%W} + ... \tag{6.1}$$

where A is a constant and a and b are related to the influence of the considered elements [120–122]. However, this method does not take account of the microstructure, which is heavily dependant on the heat treatment.

Another approach was proposed by Sugden [123] to relate the strength to the microstructure and interpret it as the sum of contributions from ferrite ($\sigma_{Ferrite}$), solid solution strengthening (σ_{SS}) and carbides ($\sigma_{Carbides}$). This method is extended here to irradiated steels and includes a contribution from irradiation–induced hardening (σ_{Irr}):

$$\sigma = \sigma_{Ferrite} \ + \ \sigma_{SS} + \sigma_{Carbides} + \sigma_{Irr} \tag{6.2}$$

By combining thermodynamic calculations (MTDATA), calculations from Sugden's theory and experimental data, each component of the yield strength (Equation 6.2) was reconstructed.

In the present case, the contribution from ferrite and solid solution strengthening was calculated as one. It is however possible to calculate the strength of pure ferrite alone by using Leslie's equations [124] but this is of no interest in the present case. The method to calculate the ferrite composition and the various contributions is explained next.

6.2.2 Composition of ferrite

MTData (Metallurgical and Thermochemical Databank), created by the National Physical Laboratory, is a program that calculates phase and chemical equilibria in any multicomponent system, using thermodynamic databases [125]. Given that all elements present and phases allowed are known, it calculates equilibria by minimising the Gibbs free energy of each phase. It was used here to calculate the composition of ferrite, given the temperature and the concentration in alloying elements.

The thermodynamic databases "SGTE Solution Database Plus" and "SGTE Substance Database", from the Scientific Group Thermodata Europe, were used for the calculation. The elements included were Fe, Cr, Ni, Mo, Mn, C, Si, P, S, Cu, Ti, Al, V, Nb, Co, N and O and the phases allowed to exist were ferrite (bcc), cementite, M_3C_2, M_6C, M_7C_3 and $M_{23}C_6$ where 'M' represents a metallic atom.

Table 6.2: MTData calculation of the ferrite composition at various temperatures. Compositions are given in mass fraction.

Element	373 K	473 K	573 K	673 K
Fe	0.9015242	0.9012984	0.9006476	0.8993335
Cr	0.0847499	0.0844513	0.0836906	0.0823635
Ni	0.0016365	0.0016358	0.0016339	0.0016304
Mo	0.0000992	0.0006078	0.0019848	0.0045551
Mn	0.0048072	0.0048052	0.0047997	0.0047893
C	0.0000000	0.0000000	0.0000000	0.0000000
Si	0.0028639	0.0028626	0.0028594	0.0028533
P	0.0003068	0.0003067	0.0003064	0.0003057
S	0.0000614	0.0000613	0.0000613	0.0000611
Cu	0.0008182	0.0008179	0.0008170	0.0008152
Ti	0.0000205	0.0000204	0.0000204	0.0000204
Al	0.0000205	0.0000204	0.0000204	0.0000204
V	0.0019053	0.0019260	0.0019739	0.0020699
Nb	0.0005523	0.0005521	0.0005515	0.0005503
Co	0.0001943	0.0001943	0.0001940	0.0001936
N	0.0003580	0.0003578	0.0003574	0.0003567
O	0.0000818	0.0000818	0.0000817	0.0000815

The concentration of substitutional solutes in ferrite was calculated every 100 K from 373 to 673 K. Table 6.2 give the phase composition at each temperature. These data were used in the next section for the calculation of the strength.

6.2.3 Strength of ferrite

The contribution of interstitials in equilibrium with carbides were neglected because they are likely to be located at defects and do not contribute to the solid solution strengthening [126–129]. The strength of ferrite is assumed to be only the sum of pure ferrite and a contribution from alloying elements.

The FORTRAN model due to Sugden [123] uses libraries from the Numerical Algorithm Group (NAg) [130] to calculate the contribution of solid solution strengthening from every subsitutional solute in ferrite.

The contribution of pure iron and solid solution strengthening (Fe + SS)

and yield strength values for the unirradiated and irradiated states (2.9–3 dpa) [119] are plotted together as a function of the test temperature in Figure 6.11. The neural–network predictions were obtained with the model described in section 6.1.

6.2.4 Interpretation

The difference between the contribution from ferrite + solid solution strengthening and the unirradiated steel is assumed to be due to carbides and the microstructure.

The difference between the unirradiated state and the irradiated state is caused by the accumulation of defects, gas bubbles and dislocation networks.

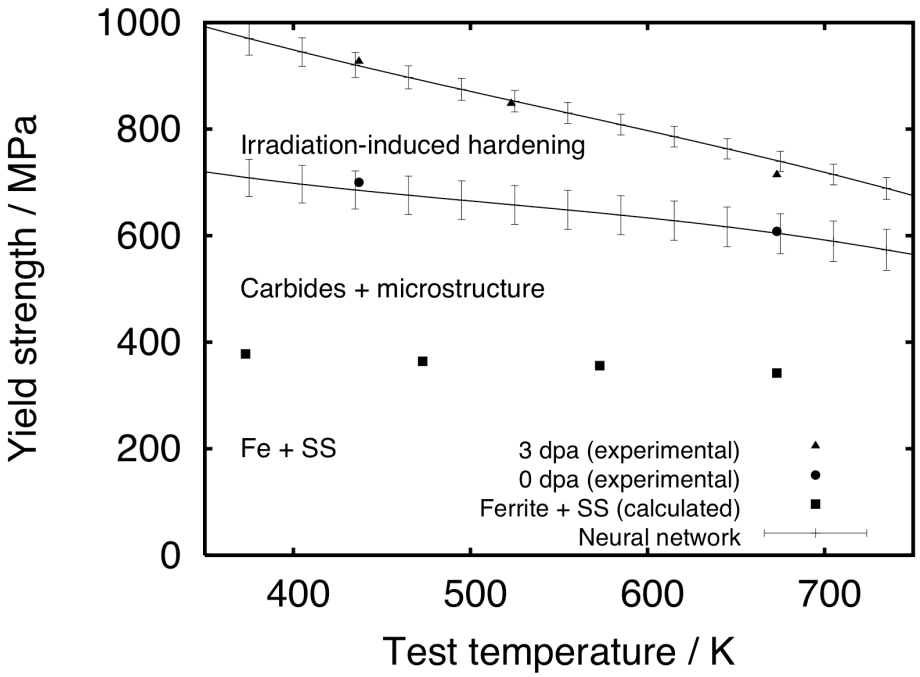

Figure 6.11: Decomposition of the strength of a steel. Black squares represent the calculated strength of ferrite + solid solution strengthening, black dots the measured strength of the unirradiated steel, black triangles the measured strength of the irradiated steel (2.9–3 dpa).

Between 300 and 700 K, the decrease in strength of the unirradiated steel is almost linear and monotonic and is consistent with the loss of strengthen-

ing due to ferrite, substitutional solutes (Fe + SS) and carbides, which can be explained by the thermal activation of dislocations and their ability to move more easily at high temperatures [119].

The diminishing of the total strength with temperature is explained mainly by the reduction of the contribution from the irradiation–induced hardening, which is expected as defects tend to recombine or annihilate.

6.2.5 Extrapolation

As strength measurements at temperatures above 700 K are often rare for irradiated steels, the model described in section 6.1 was used to predict the yield strength between 700 K and 1000 K (Figure 6.12).

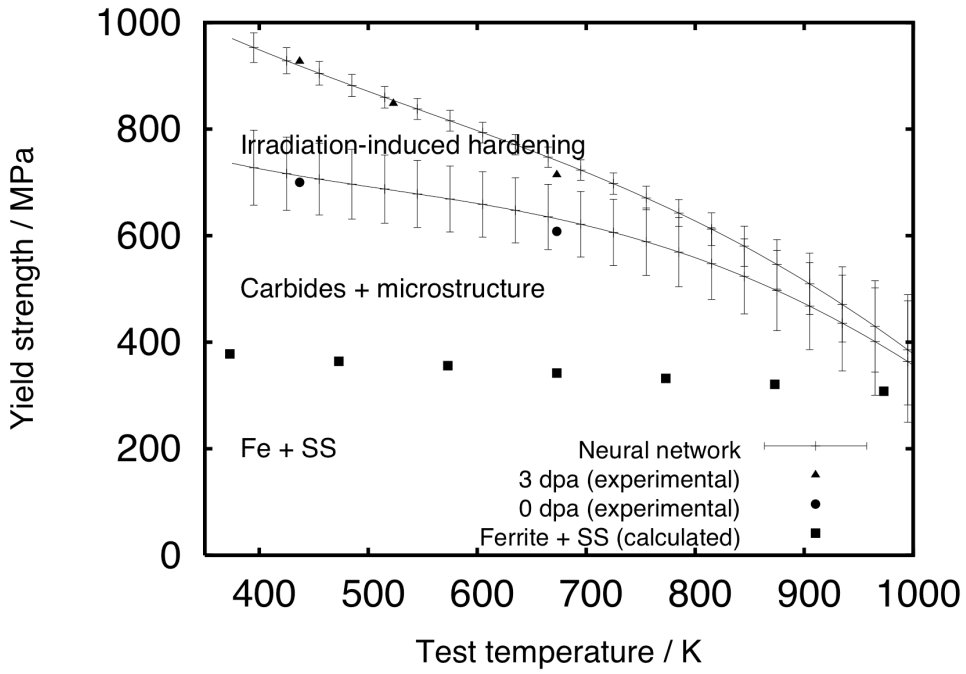

Figure 6.12: Calculation for the yield strength from 400 to 1000 K. Dots and triangles represent experimental measurements. Squares represent MT-DATA calculations and lines represent neural–network calculations.

The decrease in yield strength with the temperature is monotonic until 700 K. At these temperatures, error bars produced by the neural network are of reasonable sizes.

A change in regime can be observed after 700 K–800 K where the contribution from the original microstructure and the irradiation–induced microstructure suddenly drops. It is consistent with previous observations and calculations where the same variation was observed in ferritic creep–resistant steels [111]. The regime change cannot be attributed to a coarsening of the microstructure as the tempering temperature was 1033 K. It is postulated that it is due to the thermal activation of dislocations that can overcome obstacles. This drop in strength is in agreement with the sharp increase of the elongation described in Chapter 5 (Figure 5.7).

The contribution from irradiation hardening also diminishes above 700–800 K and tends to be almost negligible at 1000 K. At very high temperature, the strength of irradiated steels tends to be similar to that of the unirradiated states, as observed in various ferritic/martensitic steels where little damage was observed in the microstructure after irradiation at temperature above 700–725 K [131].

Several explanations were given for that softening: a high–temperature coarsening of the microstructure [132] (however in the present case, the tempering temperature is higher), a smaller size and a lower density of defects produced at high temperature [119], an instability of loops at high temperature [131], an enhanced precipitate coarsening due to irradiation-enhanced diffusion [133] and a decrease in the void swelling [113]. Interstitial atoms decomposed from loops become mobile at high temperature and can annihilate microvoids. The disappearance of microvoids is also connected with the softening at elevated temperatures [134].

However, the strength of the hardening ($\Delta\sigma$) does not depend solely on the temperature at which the irradiation (T_{irr}) and tensile tests (T_{test}) are conducted but also on the relative difference between T_{irr} and T_{test}.

Irradiation and tensile tests are often carried out at the same temperature because this is a reasonable representation of service in a fusion reactor [119]. However, because of limitations in experimental facilities, tensile tests have often been carried out at a different temperature compared to that of irradiation and this can influence $\Delta\sigma$. In some cases, tensile tests have been conducted at the irradiation temperature [25, 52], at room temperature [135, 136] or at a range of temperatures different from that at which

irradiation was experienced [137, 138]. Such difference influences the hardening.

Defects introduced at a temperature lower or equal to that of the tests ($T_{irr} \leq T_{test}$) create a large increase in yield strength but tend to anneal out quickly when the test temperature increases, leading to a rapid loss in hardening or to softening (as it is the case in Figure 6.12).

The situation is different when the irradiation takes place at the temperature which is higher than that of the test ($T_{irr} > T_{test}$). In that case, defects quickly redissolve or annihilate and cannot accumulate. The result is that irradiation contribute to a lesser extend to the hardening. However, as defects created at such temperature tend to be more thermally stable over the time scale of the test and do not anneal out easily, $\Delta\sigma$ do not diminish that much and a contribution from the irradiation–induced hardening persists. Defects introduced at high temperature cannot be dissolved during the tensile test. This is in agreement with experiments carried out on irradiated and aged steels [5].

6.3 Modelling the changes in yield strength

The absolute value of the yield strength does not always reflect the effects of irradiation or the ability of an alloy to resist irradiation–induced hardening. Differences in composition, heat treatment and test parameters can produce large variations in yield strength in the unirradiated state, and relative variations can be difficult to estimate.

In order to quantify the relationship between irradiation and hardening, it is a common practice to monitor $\Delta\sigma$:

$$\Delta\sigma = \sigma_{irradiated} - \sigma_{unirradiated} \tag{6.3}$$

A positive $\Delta\sigma$ indicates hardening whereas a negative value signifies softening. It should be noted that this is not a normalised parameter in the sense that $\Delta\sigma$ must to some extent scale with σ.

6.3.1 Model and training

To model $\Delta\sigma$, the database described in section 6.1.1 was used. For every alloy, the pre–irradiation strength was taken as a reference and $\Delta\sigma$ corresponds to the difference in strength at a given irradiation dose (Equation 6.3).

To create the database, 1659 data were collected, 417 for irradiated steels and 1242 for unirradiated steels. Details of the training are not repeated here. The final committee was tested on the database itself (Figure 6.13). Only a very limited number of outliers were observed.

The influence of chromium and irradiation temperature is particularly interesting, as will be described in the following sections.

6.3.2 Chromium concentration

Chromium is thought to be important in the resistance of alloys to hardening and 9Cr steels apparently have shown the most promising properties, especially when considering the ductile–to–brittle transition temperature (ΔDBTT) for which a clear minimum was observed at around 9 wt% Cr [84]. On the other hand, a similar optimum chromium concentration was not evident when only the elongation was taken into account [139]. It is interesting to see if such an effect is observed when the variation in yield

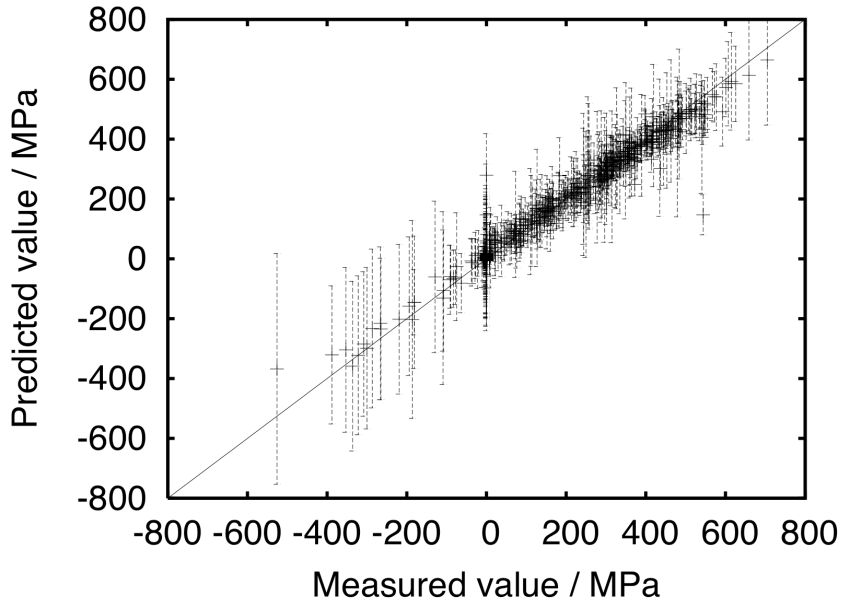

Figure 6.13: Calculated $\Delta\sigma$ as a function of the measured $\Delta\sigma$.

strength is considered.

The variation in strength as a function of the chromium concentration is plotted in Figure 6.14 for three low–activation steels (9Cr–1Mo, Eurofer'97 and F82H). The irradiation dose is 3 dpa for Eurofer'97 and F82H and 10 dpa for 9Cr–1Mo. In all cases, the irradiation temperature and the test temperature are equal to 300 K.

It appears that high–chromium concentrations are detrimental to the yield strength for all the cases studied, which is consistent with previous observations [140]. However, the situation is less clear for low concentrations. $\Delta\sigma$ tend to decrease with low–chromium concentrations and when an optimum is observed, it is around 5 wt% for 9Cr-1Mo and Eurofer'97 whereas previous results had shown that 7 to 9Cr steels show the least irradiation hardening [31]. However, it is not possible to draw certain conclusions as modelling uncertainties tend to become large.

High–chromium concentrations are clearly detrimental to the mechanical

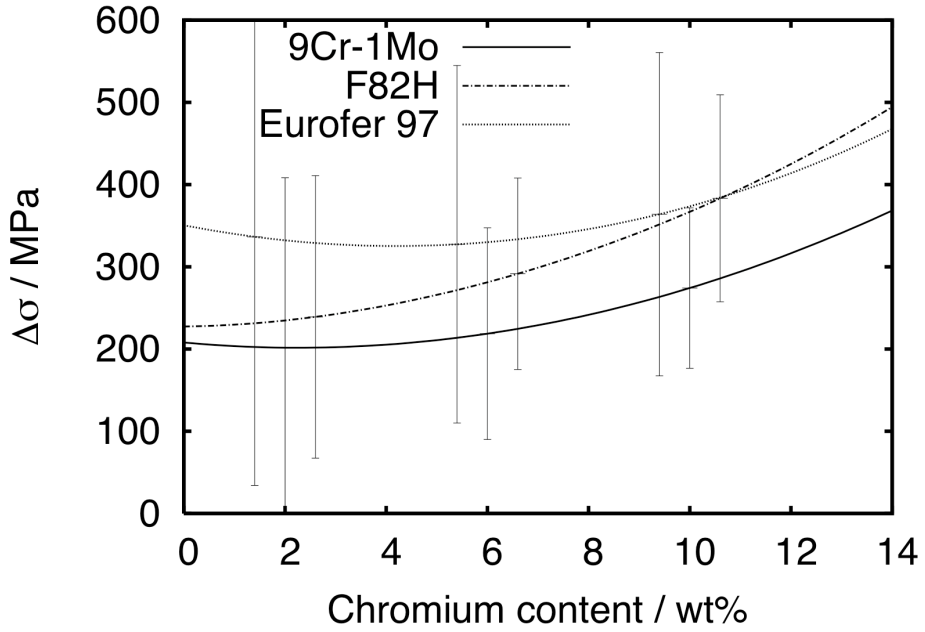

Figure 6.14: Variation in the yield strength as a function of the chromium temperature for three different low-activation steels. The irradiation doses are 3 dpa for Eurofer'97 and F82H and 10 dpa for 9Cr-1Mo. In both cases, $T_{irr} = T_{test} = 300$ K.

properties, as shown with the elongation and the yield strength models. However, based on modelling, only ΔDBTT appears to be optimised at 9 wt% Cr [84]. For the elongation and the yield strength, it is possible to say that low Cr values lessen the effects of irradiation but it is not possible to conclude if an optimum value exists.

6.3.3 Irradiation temperature and test temperature

The temperature at which defects are introduced in the alloy influences the strength of the hardening. In Figure 6.15, $\Delta\sigma$ for 9Cr-1MoVNb is plotted as a function of the irradiation dose for three different irradiation temperatures which in this case are identical to that at which the tests were conducted: 300 K, 500 K and 700 K. In Figure 6.16, $\Delta\sigma$ is then plotted as a function of the testing temperature for two irradiation doses: 3 dpa and 20 dpa. 20

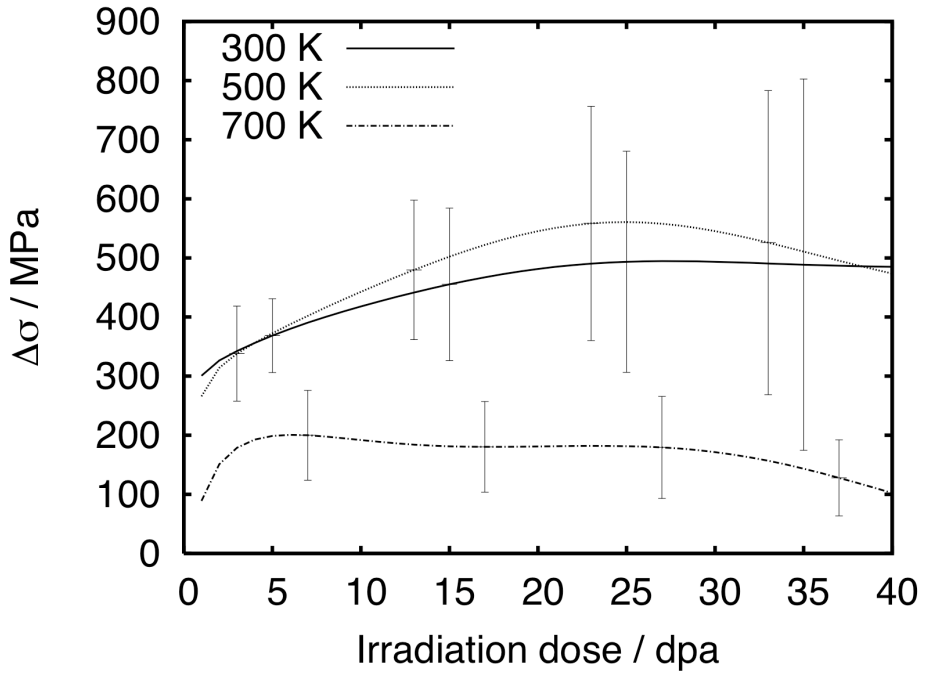

Figure 6.15: Variation of the yield strength of 9Cr-1MoVNb as a function of the irradiation dose at three irradiation and test temperatures: 300, 500 and 700 K. The alloys were normalised 1 h at 1313 K and tempered 1 h at 1033 K.

dpa was chosen because hardening goes through a maximum at that value (Figure 6.15).

The maximum in $\Delta\sigma$ is observed at 20–25 dpa when the irradiation and testing are realised at 500 K (Figure 6.15). At 300 K and 500 K, $\Delta\sigma$ are similar until $\approx$ 10 dpa but then the difference reached up to $\approx$ 100 MPa at 20 dpa. At low doses, hardening is mainly produced by point defects or small clusters, less sensitive to temperature [28] but more complex structures appear at higher doses. Defects start to reorganise into dislocation loops and networks, particularly at high temperatures, enhancing the hardening and explaining why $\Delta\sigma$ at 500 K is higher than $\Delta\sigma$ at 300 K

At 700 K, hardening effects are less severe (Figure 6.16) due to the temperature–accelerated recombination of defects. The irradiation hardening is logically greater at higher doses but the recovery due to annealing is

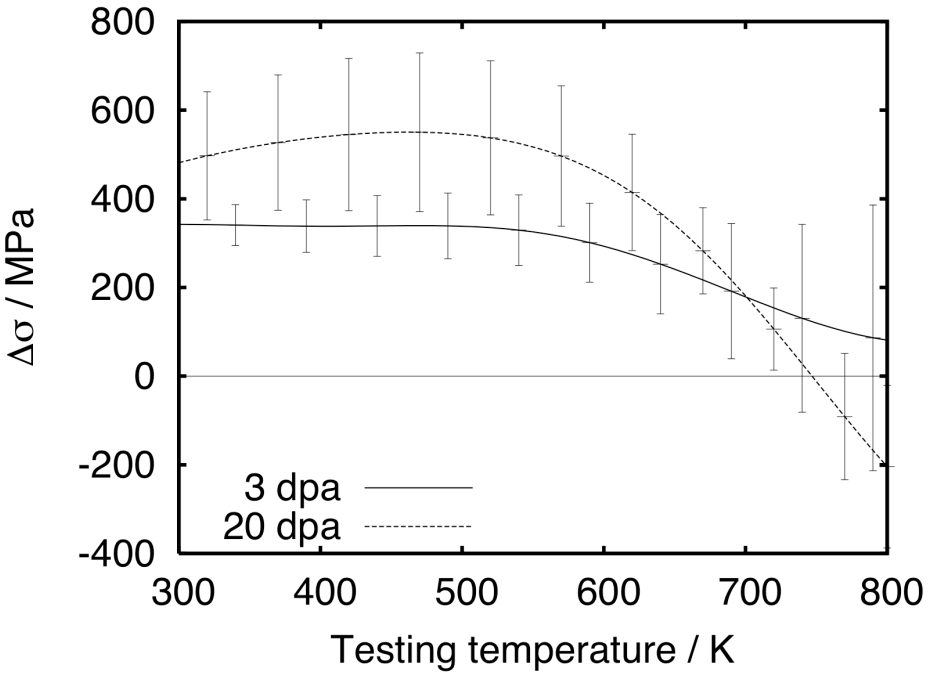

Figure 6.16: Variation of the yield strength of 9Cr-1MoVNb as a function of the test temperature for two irradiation doses: 3 and 20 dpa. Irradiation and tensile testing temperatures are the same. The alloy was normalised 1 h at 1313 K and tempered 1 h at 1033 K.

also more pronounced at higher temperature. At 700 K, the thermal activation is such that point defects quickly annihilate or are trapped at sinks and loops become unstable [131].

6.4 Comparison with Gaussian processes

Gaussian process modelling was used in this section to reproduce some aspects of the work on yield strength described earlier. A Gaussian process (GP) and a neural network (NN) model were trained on the same database and tested against experimental data. Their generalisation to unseen data was studied and they were used to make predictions. Their performance and evaluation of errors were also compared.

6.4.1 Models

A variety of methods exists that can be used to infer relationships from a large database, with various levels of success. In the case of the hot–strength of ferritic steels, genetic programming was compared with neural networks but was found not to generalise well on unseen data, due to a lack of flexibility in the method [141].

The theory of Gaussian process modelling was described in Chapter 3. That technique has been used in a large number of domains [62] and particularly in metallurgy for the development of microstructure during thermomechanic processing of metals [63], the formation of austenite in steel [64] and the microstructure and recrystallisation in aluminium–manganese alloys [65, 66]. In the case of the yield strength of nickel–base superalloys, Gaussian processes were compared with neural networks and showed the same ability to predict the behaviour of materials that were not included in the database during the training [142].

Several other aspects of GP lead to think that they represent an acceptable alternative to neural networks to model irradiated steels.

Unlike neural networks, Gaussian processes use the whole database for that and do not require a test set.

Neural networks create a large number of sub-models, which are subsequently ranked and combined to form a committee. This laborious and time–consuming process is simplified with Gaussian processes.

Gaussian processes, like neural networks, are able to calculate modelling uncertainties, reflecting the quality of the data and providing information on the risks of extrapolation. In all future calculations, predictions are given

with $\pm 1\sigma$. For neural networks, σ is described in Chapter 3. For the GP method, it corresponds to the calculated probability distribution of the output.

Database and neural network

The neural–network and Gaussian process models of the yield strength were trained on a database made of 617 experimental values (Table 6.3). The training of the neural network follows the procedure described in Chapter 3. The program for GP was used as provided and no intervention was required.

6.4.2 Comparison

Predictions with the GP and the NN were first realised on two datasets, one of the them made of new data, in order to study their generalisation. Both models were then used to make predictions.

Generalisation

Two sets of data were created: the first one containing the data used for the training and the second one containing new data. The new set was made of 150 yield strength values for irradiated and unirradiated alloys in different metallurgical and test conditions. They were not included in the initial database but were inside the data range for training and testing, with irradiation doses reaching up to 15 dpa.

In order to compare performance and estimation of errors, the *error standard deviation* (root mean square residual, RMS) R_{test} and the average size of error bars E_{bar} were calculated as follows:

$$R_{test} = \sqrt{\frac{1}{N}\sum_{i=1}^{N}(T_i - O_i)^2} \tag{6.4}$$

$$E_{bar} = \frac{1}{N}\sum_{i=1}^{N} E_i \tag{6.5}$$

where N represents the total number of predictions, T_i and O_i the experimental and calculated values and E_i the error accompanying each prediction. The residual R_{test}, by quantifying the "distance" between the prediction and

Parameter	Minimum	Maximum	Average	Standard deviation
T_γ / K	1173	1373	1319	46
t_γ / min	4.8	111	42	17
T_T / K	948	1053	1017	29
t_T / min	30	480	87	77
C / wt%	0.064	0.21	0.122	0.042
Cr / wt%	2.15	13.6	8.9	2.5
W / wt%	0	2.96	1.07	0.95
Mo / wt%	0	1.59	0.46	0.51
Ta / wt%	0	0.14	0.03	0.04
V / wt%	0	0.39	0.22	0.07
Si / wt%	0	0.42	0.12	0.10
Mn / wt%	0	2.09	0.48	0.25
N / wt%	0	0.17	0.017	0.026
Cu / wt%	0	0.16	0.019	0.031
Nb / wt%	0	0.45	0.024	0.065
Ni / wt%	0	2.3	0.32	0.63
P / wt%	0	0.03	0.008	0.007
Ti / wt%	0	0.052	0.005	0.008
Irradiation temperature / K	293	1146	470	207
Irradiation dose / dpa	0	72	9.1	14.5
Helium / appm	0	5000	147	574
Test temperature / K	123	923	551	210
Yield strength / MPa	174	1357	669	256

Table 6.3: Properties of database used to create the neural network and Gaussian process models. T_γ and t_γ are the austenitisation temperature and time respectively, and T_T and t_T the tempering temperature and time respectively.

the actual value, is a good tool to evaluate the accuracy of the model.

Predictions for the first set are given in Figure 6.17.

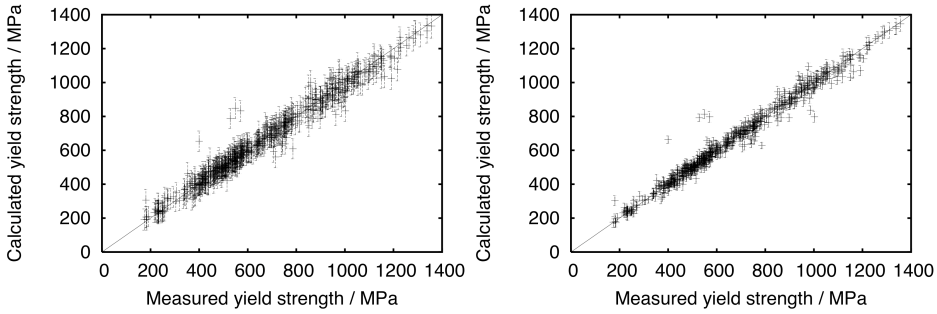

(a) Gaussian process (b) Neural network

Figure 6.17: Predictions for the database itself (617 data) for the Gaussian process (a) and the neural network (b).

There is a small dispersion around the $y = x$ line which means both models give good predictions even if a small number of outliers (experimental value outside of the ± 1 σ prediction) can be observed. Modelling uncertainties are larger for the Gaussian process though.

Predictions for new data are given in Figure 6.18.

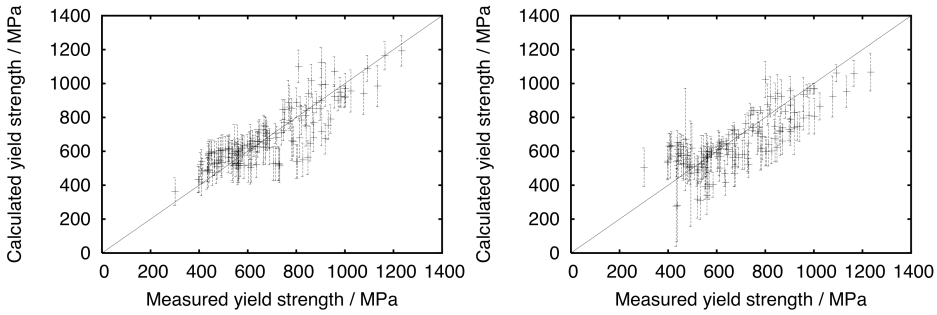

(a) Gaussian precess (b) Neural network

Figure 6.18: Predictions for unseen data (150 values) for the Gaussian process (a) and the neural network (b).

Corresponding R_{test} and E_{bar} are given in Table 6.4.

Table 6.4: R_{test} and E_{bar} for the Gaussian process and the neural network models.

	Neural Network		Gaussian Process	
	R_{test}	E_{bar}	R_{test}	E_{bar}
Seen data / MPa	38	±29	44	±63
Unseen data / MPa	120	±84	102	±83

With the dataset used for training, R_{test} for the Gaussian process is slightly larger than that for the neural network and error bars (E_{bar}) are on average twice larger. For unseen data, error bars have a similar size but R_{test} is reduced by 18 MPa.

Based on these observations, neural–network predictions are more accurate than Gaussian process on data that were used for the training. However, on unseen data, GP performs slightly better. This suggests that GP generalises better than NN but this is offset by the larger modelling uncertainties obtained by GP. It is however not clear whether this is a fundamental outcome or associated with the data.

Predictions

After demonstrating the ability of GP to generalise to new data, the performances of NN and GP were compared by using them to make predictions. Calculations were made with GP and NN for two alloys with two different chromium concentrations: 2.25 wt% and 9 wt%. Results of calculations of the yield strength as a function of the irradiation are given in Figure 6.19(a) for 2.25Cr and 6.19(b) for 9Cr. Compositions are given in Section 5.2. In both cases, the irradiation and testing temperature were equal to 638 K.

The main difference between the two models is at low doses where the neural network captures the step increase between 0 and 5 dpa followed by a peak/saturation (which is coherent with hardening mechanisms) whereas the Gaussian process calculates a smoother trend. Error bars are larger with GP but both models are in agreement with experimental values. They both correctly represent the overall behaviour of the steel.

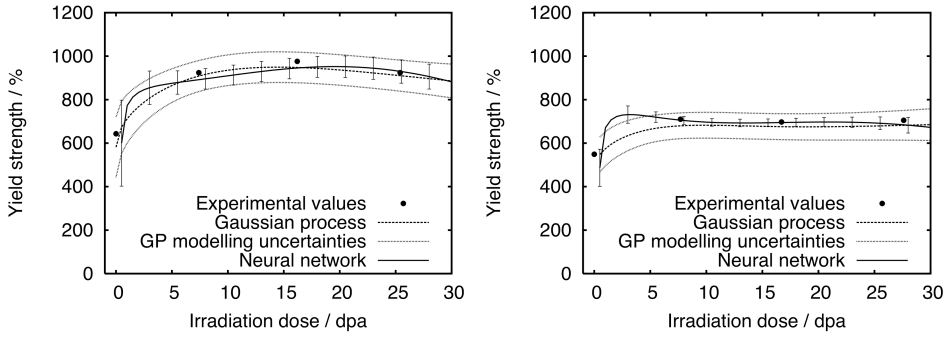

(a) 2.25 Cr (b) 9 Cr

Figure 6.19: GP and NN calculations of the yield strength of a 2.25 Cr alloy (a) and a 9 Cr alloy (b). Black dots represent experimental values, included in the database.

6.4.3 Extrapolation

Predicting the yield strength in conditions that simulate the fusion regime remains the main objective. Using the Gaussian process, the yield strength of Eurofer'97 and F82H was calculated at doses and temperatures of up to 200 dpa and 1000 K.

Figures 6.20 and 6.21 represent the yield strength and error for Eurofer'97 and Figures 6.22 and 6.23 for F82H. Chemical compositions, heat treatments and irradiation and testing conditions are similar to those in Section 6.1.4.

For moderate irradiation doses and temperatures, predictions by the neural network and the Gaussian process are similar but start to diverge when the dose and the temperature increase. The Gaussian process prediction tends towards an arbitrarily chosen mean value which is often the case when a model is extrapolated beyond a certain lengthscale.

Just as with the elongation, several mechanisms can be postulated but the only way to decide which trend is correct is to collect data at higher irradiation doses. Data at irradiation doses above 100 dpa for example will reduce modelling uncertainties and will enable the model to correctly represent the regime of highly irradiated materials.

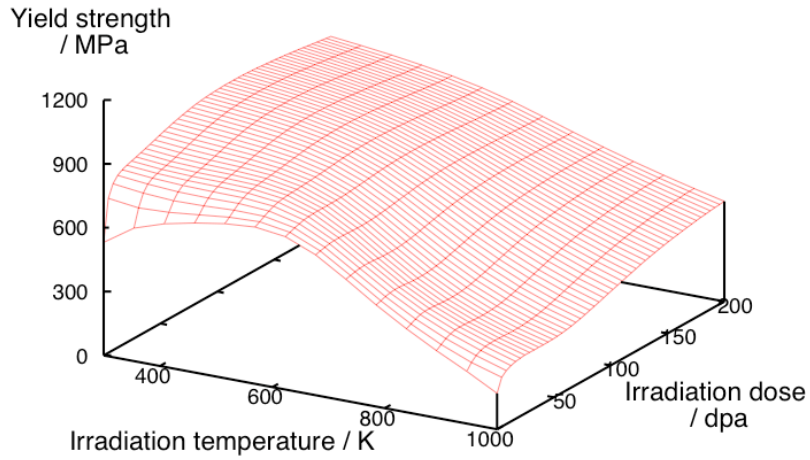

Figure 6.20: Predictions for Eurofer'97 in fission and fusion conditions.

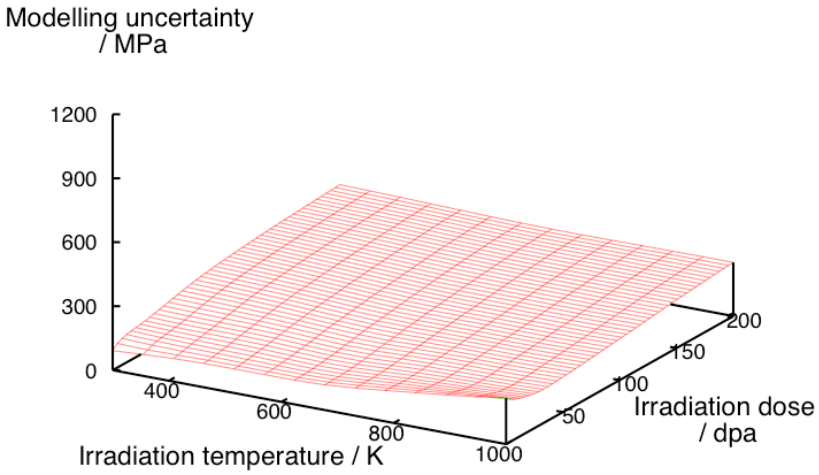

Figure 6.21: Predictions for Eurofer'97 in fission and fusion conditions.

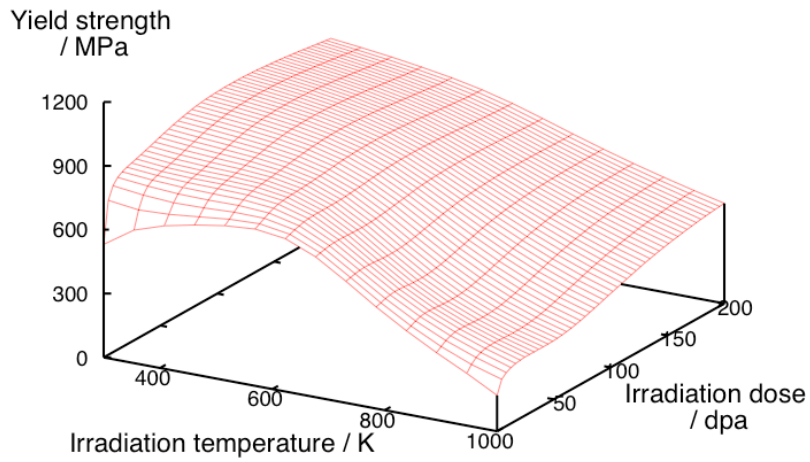

Figure 6.22: Predictions for Eurofer'97 in fission and fusion conditions.

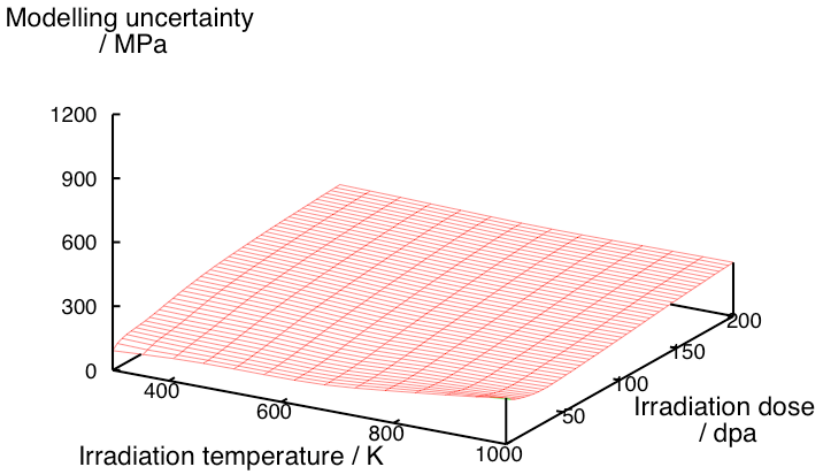

Figure 6.23: Predictions for Eurofer'97 in fission and fusion conditions.

6.5 Conclusions and summary

In this chapter, neural–network and Gaussian process models of the yield strength were created and compared to experimental data and against each other.

A new neural–network model of the yield strength that incorporates the heat treatment was created and produced correct predictions. It was used to interpret the yield strength as a function of various contributions from ferrite, solid solution strengthening, carbides and microstructure and a contribution from irradiation–induced hardening. That decomposition allowed an explanation of the loss of strength with temperature. It enabled us to follow the variation with temperature only due to irradiation. It highlighted the role of the irradiation and test temperatures and the change in behaviour when those two temperatures differ.

Modelling the variation of the yield strength ($\Delta\sigma$) instead of the yield strength directly allowed an easier capture of certain properties. The $\Delta\sigma$ model confirmed that radiation–induced hardening is maximal at intermediate temperature due to a higher mobility of defects and pointed out that the yield strength is not necessarily optimised at 9 wt% Cr even if low–chromium alloys generally present a better resistance.

Gaussian process modelling was introduced and compared to neural network results. Both models predicted adequately data included in the database but the Gaussian process generalises better on unseen data.

Training a Gaussian process also requires less time than for a neural network because there is neither a need to create unnecessary models nor to assess them. Gaussian processes get information from the whole database but they need a constant access to the database for predictions. Neural–network models can be exported *as is*, without the database, which may contain confidential data.

The different behaviour between the Gaussian process and the neural network when used to extrapolate confirmed that it is not, at the moment, possible to realistically calculate the conditions of a steel in fusion conditions. More data need to be obtained at high doses.

The neural–network model of the yield strength is freely available online on the Materials Algorithms Project:
http://www.msm.cam.ac.uk/map/mapmain.html
Instructions for the program are given in the Appendix C.

Acknowledgement

I am very thankful to Oliver Stegle for the useful explanations about Gaussian processes. The program itself was created and provided by Oliver Stegle and D. J. C. MacKay from the Department of Physics from the Inference Group, Cavendish Laboratories, University of Cambridge [143] and run on MATLAB [144].

Chapter 7

Optimisation

Several solutions have been proposed to reduce modelling uncertainties and increase the precision of the predictions of a neural network, such as the simplification of the network and the introduction of a target–driven component selection [145, 146] or the addition of stochastic noise in the database [147].
In this chapter, an attempt was made to improve the ability to extrapolate by manually allocating the two sets resulting from the initial partitioning of the initial database, the training set being made of data for which the irradiation is "low" and the testing set being made of data for which it is "high". For each of the parameters described in the two previous chapters (elongation and yield strength) and for the ductile–to–brittle transition temperature, two neural networks were created: one following that procedure and one for which the training and testing sets are automatically determined. This has the effect that the models with the best ability to extrapolate are selected at the committee selection stage of the training. Predictions were compared and the most striking outcome is that this new training reduces errors in predictions and modelling uncertainties when the parameter to model in extrapolated.

7.1 Method

During the design of a neural network, overfitting is avoided by partitioning the initial database into two equal sets of data, one for the training and one for the testing.

The aim of the modified method is to have a complete control on the content of the training and testing sets and suppress the random selection. It is expected that a careful choice of the two sets will improve the extrapolation ability of the network without compromising its performance in interpolation mode.

7.2 Definitions

A few terms used in the next sections must be defined beforehand:

- *Interpolation mode* refers to calculations made by a model on data which are within the range of values between the minimum and the maximum value of the database.
- *Extrapolation mode* refers to calculations made by a model on data beyond the domain defined just above. This mode is usually used to explore domains where experimental data are absent.
- *Classical training* and *classical model* refer to a neural network trained as described in Chapter 3 (automatic partitioning of the database).
- *Optimised training* and *optimised model* refer to a neural network trained on a database that was manually partitioned. The method is detailed in the following section.
- *Training*, *testing* and *extrapolation set* refer to sets of data used for the training and the testing of the model and data, not included in the database, used for prediction.

7.2.1 Partitioning of the database

The training of a neural network involves the partitioning of the initial database. Model manager [148], the software used to create the models, allows one to select the size of the testing and training sets but not the content, which is automatically determined. The repetition of the training can lead to a different partitioning and a different model. In order to suppress this source of difference, it has been suggested that a manual selection of the training and testing datasets may be an alternative procedure [145, 146] .

In the case of irradiated steels, it is possible to train the model on experimental data for which the dose is "low" and then test it on data for "higher" doses.

7.2.2 Creation of models, performance and comparison

The procedure to create an optimised neural network was similar to the one described in Chapter 3 but the *training* and *testing set* data were allocated manually.

Considerable data on irradiation are available at doses below 30 dpa and very little at doses between 30 and 100 dpa, which is a level relevant to fusion reactors. Approximately, only 3.5 % of the alloys presented in Appendix A were irradiated at doses above 30 dpa. For that reason, data collected at doses below that limit was used to create the networks and that collected at doses above that limit (*extrapolation set*) was used to test the model in extrapolation mode. Data obtained at doses below 30 dpa were divided into a *training set* (0–15 dpa) and a *testing set* (15 dpa–30 dpa). More details on the repartition of data can be found in Sections 7.3, 7.4 and 7.5.

During the training with the BIGBACK program, the files `data.txt.train` and `data.txt.test` created by Model Manager were modified.

`data.txt.train` contains data corresponding to the *training set* and `data.txt.test` to the *testing set*. Data for the *extrapolation set* are unseen by the model during the training and are kept for subsequent tests.

In order to compare performances and estimation of errors between a *classical* and an *optimised model*, the *error standard deviation* (root mean square residual, RMS) R_{test} and the average size of error bars E_{bar} were calculated as follows:

$$R_{test} = \sqrt{\frac{1}{N}\sum_{i=1}^{N}(T_i - O_i)^2} \tag{7.1}$$

$$E_{bar} = \frac{1}{N}\sum_{i=1}^{N} E_i \tag{7.2}$$

where N represents the total number of predictions, T_i and O_i the experi-

mental and calculated values and E_i the error accompanying each prediction.

Calculations for the three parameters are reviewed next.

7.3 Elongation

An *optimised* model of the elongation was created using the database from Chapter 5. The spread of data is illustrated in Figure 7.1. The *training set* was made of 1480 experimental values, the *testing set* of 70 experimental values and 58 experimental values were kept to test the model in *extrapolation mode*. For comparison, a *classical* model of the elongation was trained on the same database.

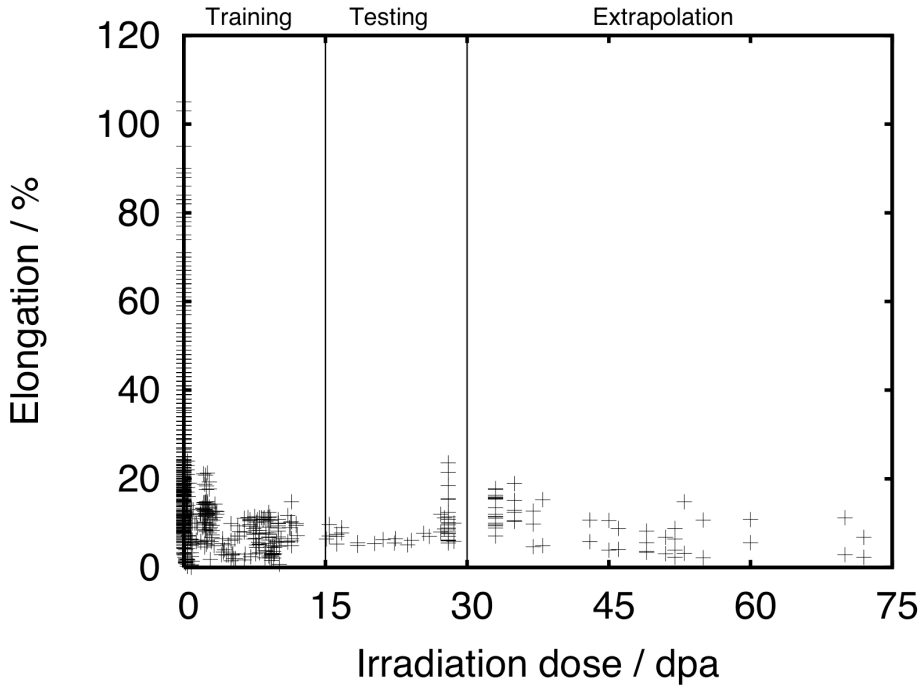

Figure 7.1: Repartition of elongation values in the database.

Calculations for the three sets of data are shown next: Figure 7.2 for the *training set*, Figure 7.3 for the *testing set* and Figure 7.4 for the *extrapolation set*. Residual tests (R_{test}) and average error bars (E_{bar}) are listed in Table 7.1.

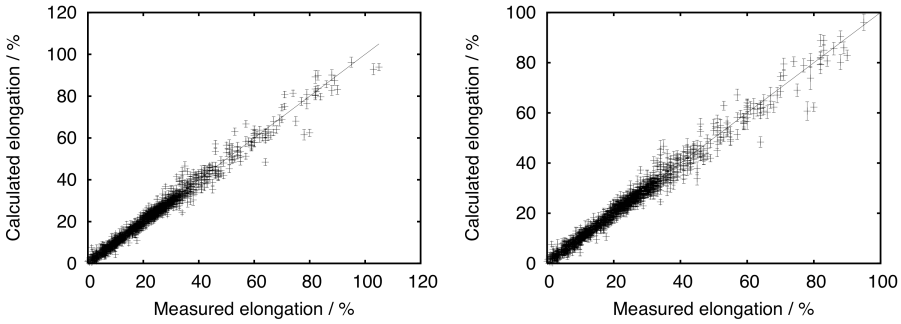

(a) Classical model (b) Optimised model

Figure 7.2: Predictions for the *training set*.

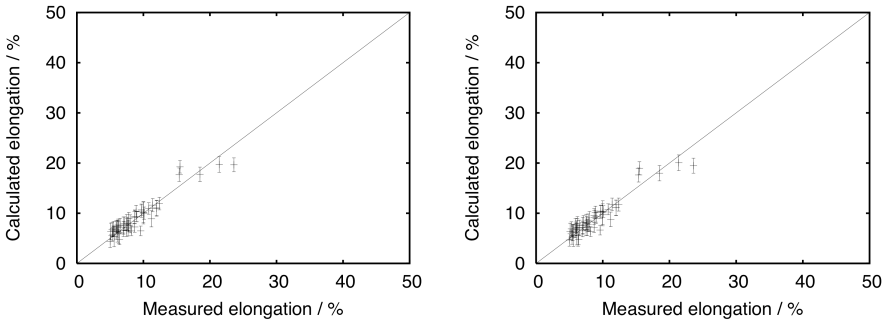

(a) Classical model (b) Optimised model

Figure 7.3: Predictions for the *testing set*.

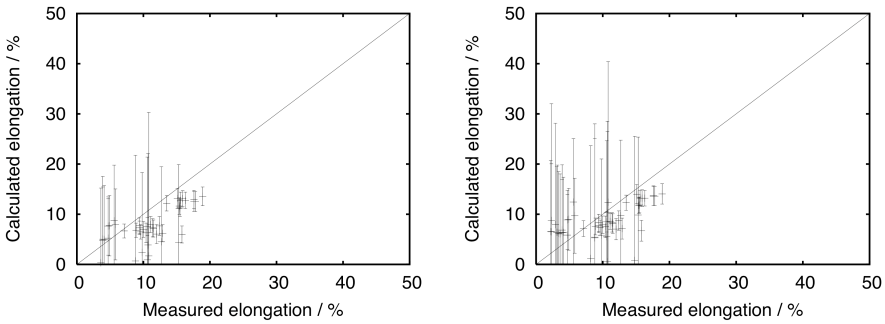

(a) Classical model (b) Optimised model

Figure 7.4: Predictions for the *extrapolation set*.

Table 7.1: Residual test and average error bars for the elongation with a *classical* and an *optimised* model. All values are given in %.

Dose	Parameter	Classical model	Optimised model
Training set	R_{test}	2.2	2.3
(0–15 dpa)	E_{bar}	±1.3	±1.5
Testing set	R_{test}	1.3	1.3
(15–30 dpa)	E_{bar}	±1.4	±1.4
Extrapolation set	R_{test}	8.7	5.0
($>$ 30 dpa	E_{bar}	±11.6	±11.1

For the *training* and *testing sets*, the manual partitioning of the database does not have an influence on the predictions. R_{test} and E_{bar} have almost the same value in both cases.

For the *extrapolation set*, modelling uncertainties have a similar order of magnitude but the residual is reduced from 8.7 to 5.0 %.

7.4 Yield strength

An *optimised* model of the yield strength was designed using the database from Chapter 6. The spread of data is illustrated in Figure 7.5. The *training set* was made of 1778 experimental values, the *testing set* of 70 experimental values and 68 experimental values were kept to test the model in *extrapolation mode*. For comparison, a *classical model* of the yield strength was trained on the same database.

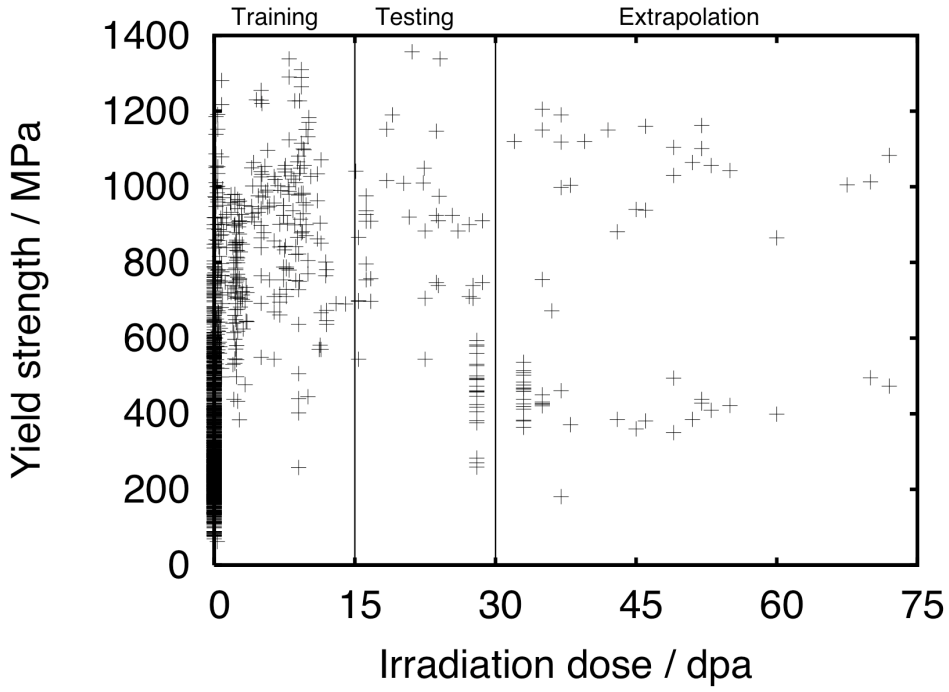

Figure 7.5: Repartition of yield strength values in the database.

Calculations for the three sets of data are shown next: Figure 7.6 for the *training set*, Figure 7.7 for the *testing set* and Figure 7.8 for the *extrapolation set*. Residual tests (R_{test}) and average error bars (E_{bar}) are listed in Table 7.2.

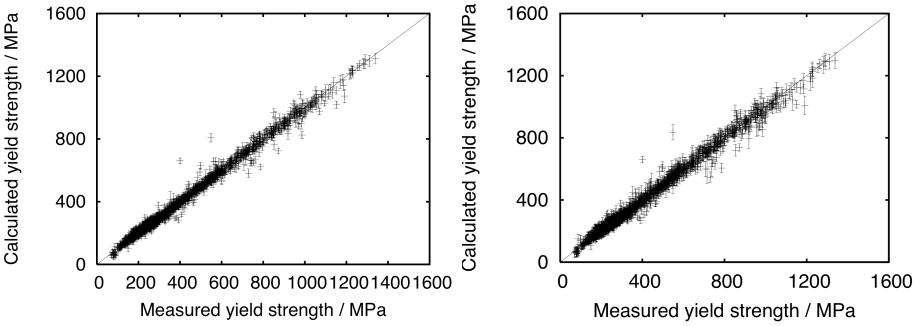

(a) Classical model (b) Optimised model

Figure 7.6: Predictions for the *training set*.

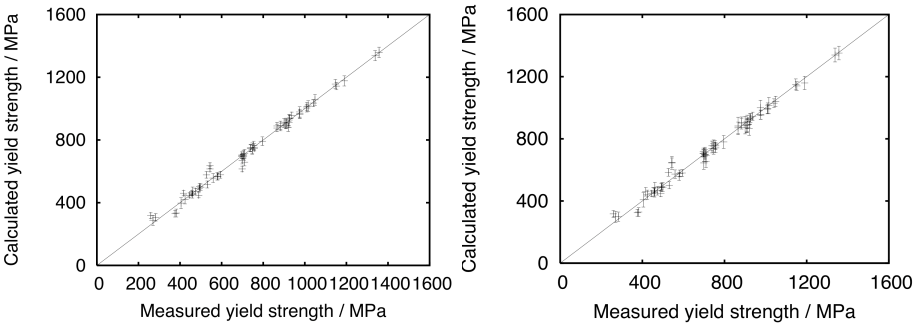

(a) Classical model (b) Optimised model

Figure 7.7: Predictions for the *testing set*.

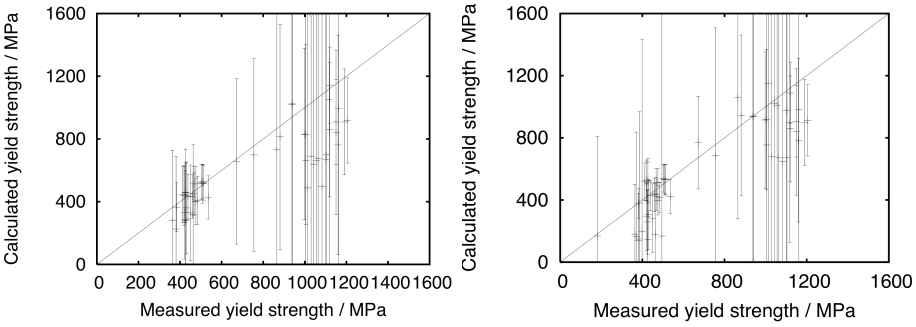

(a) Classical model (b) Optimised model

Figure 7.8: Predictions for the *extrapolation set*.

Table 7.2: Calculations for the yield strength with a *classical* and an *optimised* mode. All values are given in MPa.

Dose	Parameter	Classical model	Optimised model
Training set	R_{test}	24	29
(0–15 dpa)	E_{bar}	±17	±22
Testing set	R_{test}	25	29
(15–30 dpa)	E_{bar}	±24	±33
Extrapolation set	R_{test}	361	300
(> 30 dpa)	E_{bar}	±817	±682

Unlike the elongation, R_{test} for the yield strength on the *training* and *testing set* are slightly larger with the *optimised model* (+5 MPa for the *training set* and +4 MPa for the *testing set*). Modelling uncertainties are also more important

However, on the *extrapolation set*, R_{test} and modelling uncertainties are reduced with the optimised model. R_{test} is reduced by 61 MPa, from 361 to 300 MPa, and E_{bar} by 135 MPa, from 817 to 682 MPa.

7.5 Ductile–to–brittle transition temperature

An *optimised* model of the ductile–to–brittle transition temperature was created with the database compiled by Yamamoto *et al.* [149] and used by Cottrell *et al.* [84]. The spread of data is illustrated in Figure 7.9. The *training set* was made of 514 experimental values, the *testing set* of 45 experimental values and finally, 21 experimental values were kept to test the model in *extrapolation mode*. For comparison, a *classical model* of the ductile–to–brittle transition temperature was trained on the same database.

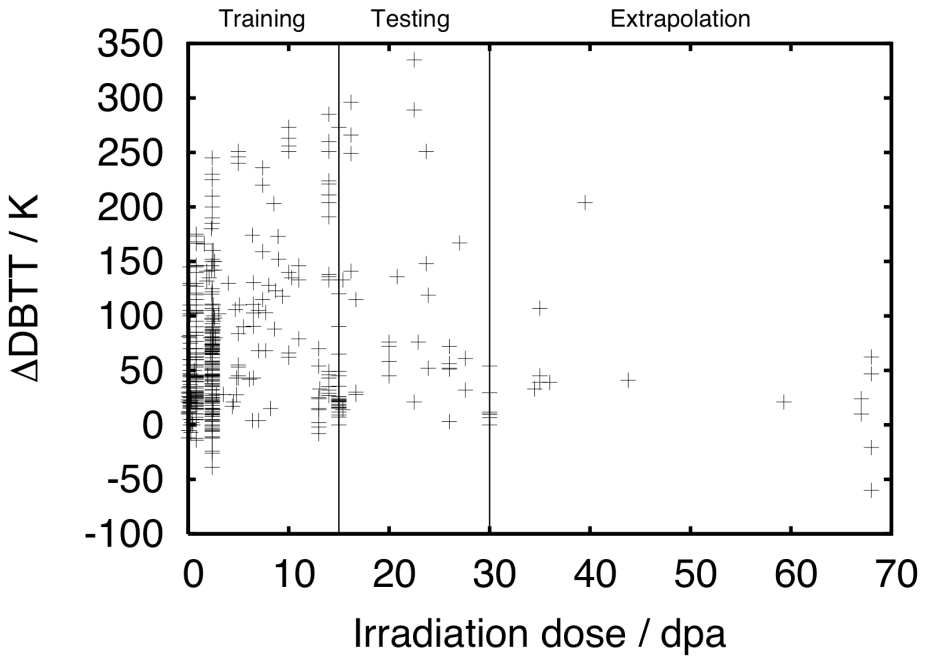

Figure 7.9: Repartition of ductile–to–brittle transition temperature values in the database.

Calculations for the three sets of data are shown next: Figure 7.10 for the *training set*, Figure 7.11 for the *testing set* and Figure 7.12 for the *extrapolation*. Residual tests (R_{test}) and average error bars (E_{bar}) are listed in Table 7.2.

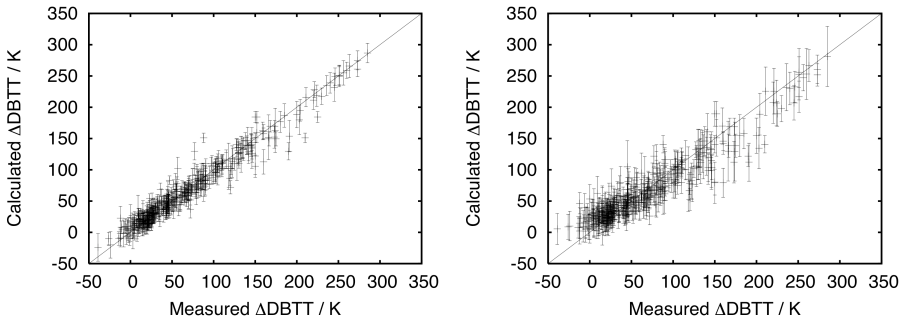

(a) Classical model (b) Optimised model

Figure 7.10: Predictions for the *training set*.

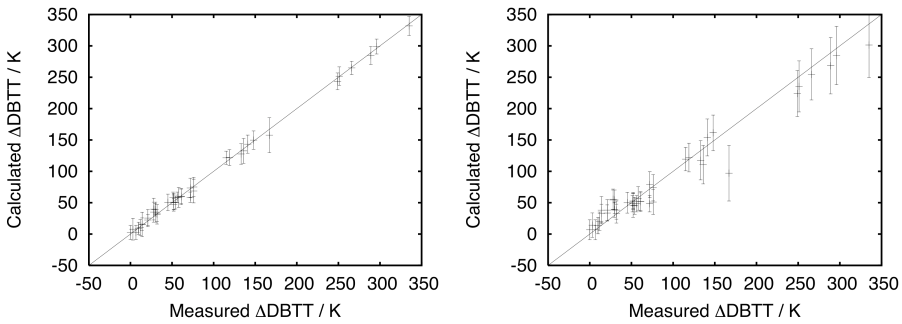

(a) Classical model (b) Optimised model

Figure 7.11: Predictions for the *testing set*.

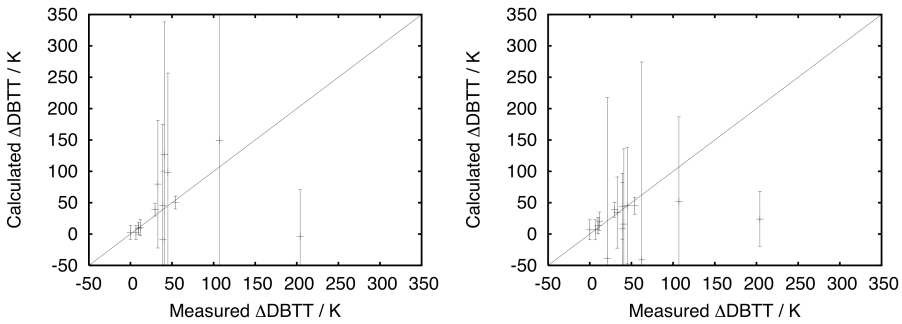

(a) Classical model (b) Optimised model

Figure 7.12: Predictions in the *extrapolation set*.

Table 7.3: Calculations for the ductile–to–brittle transition temperature with a *classical* and an *optimised* mode. All values are given in K.

Dose	Parameter	Classical model	Optimised model
Training set	R_{test}	11.8	20.3
(0–15 dpa)	E_{bar}	±12.2	±16.6
Testing set	R_{test}	4.7	17.9
(15–30 dpa)	E_{bar}	±13.2	±21.2
Extrapolation	R_{test}	149.8	73.3
(> 30 dpa)	E_{bar}	±289.4	±154.7

Similar to the yield strength, the *classical model* gives better predictions on the *training* and the *testing set*. However, for extrapolated data, predictions with the *optimised model* are more accurate. R_{test} is reduced by ≈76 K and error bars by ≈135 K.

7.6 Discussion

Predictions for the three sets of data for the two training methods are listed in Tables 7.4, 7.5 and 7.6.

Table 7.4: Predictions for the *training set* (0–15 dpa).

		Classical model	Optimised model
Elongation / %	R_{test}	2.2	2.3
	E_{bar}	±1.3	±1.5
Yield strength / MPa	R_{test}	24	32
	E_{bar}	±17	±22
ΔDBTT / K	R_{test}	11.8	20.3
	E_{bar}	±12.2	±16.6

Table 7.5: Predictions for the *testing set* (15–30 dpa).

		Classical model	Optimised model
Elongation / %	R_{test}	1.4	1.3
	E_{bar}	±1.3	±1.4
Yield strength / MPa	R_{test}	25	29
	E_{bar}	±24	±33
ΔDBTT / K	R_{test}	4.7	17.9
	E_{bar}	±13.2	±21.2

The situation for the training and testing sets is similar. For irradiation doses below 15 dpa, predictions for the elongation are comparable. In each case, R_{test} and E_{bar} calculated by both models are of similar sizes. However, predictions are less accurate and modelling uncertainties are larger for the yield strength and the ΔDBTT (+8 MPa for R_{test} and +5 MPa for E_{bar} for σ and +8.5 K and +4.4 K for the ΔDBTT).

For irradiation doses between 15 and 30 dpa, the two training methods give the same results for the elongation. However, R_{test} and E_{bar} are slightly larger for the yield strength (+4 MPa for R_{test} and +9 MPa for E_{bar}) and much larger for the ductile–to–brittle transition temperature (13.2 K for

R_{test} and 8 K for E_{bar}).

Table 7.6: Predictions for data used in *extrapolation* mode (>30 dpa).

		Classical model	Optimised model
Elongation / %	R_{test}	8.7	5.0
	E_{bar}	±11.6	±11.1
Yield strength / MPa	R_{test}	361	300
	E_{bar}	±817	±682
ΔDBTT / K	R_{test}	149.8	73.3
	E_{bar}	±249.4	±154.7

For calculations on the *extrapolation set*, R_{test} and E_{bar} are naturally much larger, because data are well outside the range of the training database. However, for the *optimised model*, a reduction in the residual test is observed for the three parameters (-3.7 % for the elongation, -61 MPa for the strength and -76.6 K for the ductile–to–brittle transition temperature) and modelling uncertainties accompanying the predictions are also reduced for σ and ΔBDTT (-135 MPa and 94.7 K) but nothing conclusive can be said for the elongation.

Some arguments can be put forward to explain the advantages of the optimised model over the classical one.

An *optimised* neural–network model is made of sub–models that particularly perform well at high irradiation doses and it is known that neural networks often keep the trend they have captured at the end of the database [142]. The trend inferred at high dose still represents the reality as long as underlying mechanisms remain the same [150]. In the case of irradiation, the hardening mode changes after a critical dose whose value varies between 10 and 20 dpa. Radiation–induced hardening is very important in the early moments of the irradiation but it usually saturates above that value. Models that have captured that feature are selected in the committee and are more likely to correctly represent what happens beyond the database. However, after a certain lengthscale, predictions by a neural network are biased by the mathematical function initially chosen.

The possibility to choose the type of data to include in the training or

testing set allows a better distribution of the information. Databases are often compiled by aggregating results from the literature which can lead to the accumulation of experimental values concerning a particular alloy. After the splitting, such clusters can end up in one or the other set of data, and that would mean that submodels can be trained on a particular grade of alloys and tested on another one. When the final committee is built up, it may not perform satisfactorily on the whole database. In some cases, it has been observed that the manual selection of the two sets leads to improved prediction ability [151].

Before the splitting of the initial database, it is also possible to allow the randomisation of the database, to avoid the existence of aforementioned clusters of data. This involves a random reorganisation of the lines of the database.

7.7 Conclusions and summary

A method for training a neural network during which the initial database was manually partitioned into a training and a testing set was tested. The training set was made of data for which the irradiation dose is below 15 dpa and the training set data for which the irradiation was between 15 and 30 dpa. Data with irradiation doses in excess of 30 dpa were used for extrapolation. Models of the elongation and yield strength were created compared to classical models.

The principal conclusion is that this optimised training, which forces the algorithm to select models which generalise well on data for high–irradiation doses, reduces errors and modelling uncertainties for new data that are situated outside the range of the database. However, this improvement in extrapolation mode is balanced by less accurate predictions in interpolation, for data already included in the database.

Besides that, the creation of the network, by specifically determining the training and testing sets, suppresses some randomness–based aspects of the partitioning of the initial database. It also allows a better distribution of the data in the two sets, avoiding the lack or the overrepresentation of a certain family of inputs in one or the other set of data.

This method can be extended to other cases where the model is used to extrapolate.

Chapter 8

Conclusions and suggestions for future work

The main goal of this thesis was to create well–designed empirical models of the mechanical properties of irradiated steels.

Based on prior experience with neural networks and previous work with irradiated steels, a set of recommendations for training future models were postulated. Models were improved by taking into account the heat treatment and by training them on the raw value of the output instead of a derived function. These two modifications brought more physical knowledge in the model and suppressed a mathematical bias observed in earlier calculations, particularly important highly extrapolated models.

A neural–network model was created, which allowed the calculation of the elongation for a variety of alloys. The Bayesian framework allowed an estimation of uncertainties via error bars which give information about the risk of extrapolation. Results from this model suggest that the elongation may not be optimised at 9 wt% Cr.

A neural–network model of the yield strength was created and produced correct predictions. In combination with other modelling tools, it helped to describe the loss of strength with the irradiation and test temperature. A model of the variation in the yield strength described the influence of temperature on hardening.

The Gaussian process technique was implemented to calculate the yield strength. When compared to neural networks, it showed a better ability to

generalise to new data.

Neural–network and Gaussian process predictions in fusion conditions were attempted but large modelling uncertainties at high dose and elevated temperature prevent one from drawing clear conclusions. Moreover, extrapolating two neural–network (in Kemp *et al.* and in this thesis) and a Gaussian process model of the same parameter has led to three different trends, which could be partly explained by the different mathematical functions chosen for each model. This also emphasises that the lack of data and knowledge of mechanisms remains the major problem.

It was possible to improve modelling predictions in extrapolation at moderate doses by manually allocating the training and testing sets. Models of three parameters were created and predictions were made for sets of data situated outside the range for training. They showed an improvement in accuracy and a reduction in modelling uncertainties. However, it would be necessary to determine to what extent the values delimiting the training, testing and extrapolating sets can influence that result. It would also be interesting to see if that result can be generalised and if such a training technique produces the same improvement with other neural network models.

Longer scale extrapolation will however require more data which will have to be collected. Data yielded by the IFMIF and ITER should be correctly exploited. Experiment reports should include an extensive characterisation of alloys (composition, heat treatment, any information relative to any pre–irradiation treatment of the steel) and a detailed description of the irradiation and tensile testing experiments (concentration in helium and hydrogen, type of reactor, duration of irradiation, flux, information about the energy of neutrons). Such detailed data would allow more "artificial parameters" which are the only way to include physical aspects in the model (dpa/helium, kinetic time, *etc.*).

An alternative suggestion to reduce modelling uncertainties and increase the reliability of models in areas far from the domain of available knowledge must come from a better understanding of hardening mechanisms. It will also be necessary to postulate mechanisms that are likely to influence the strength and toughness at high doses, such as radiation-induced dissolution of precipitates or radiation-induced amorphisation. This will enable us to

decide which trend is most likely to be true.

Finding an optimal composition for candidate materials using neural networks has already been attempted [116]. Such compositions should be refined as better models will be produced when data at higher doses are collected. Several parameters could be simultaneously optimised, by using different genetic algorithms or by using multiobjective evolutionary algorithms.

Appendix A

Publications used for the database

This is a list of the references (articles and experiment reports) used to create the databases for the neural–network and Gaussian process models of the elongation, yield strength and ductile–to–brittle transition temperature.

R. L. Klueh and P. J. Maziasz. Effect of irradiation in HFIR on tensile properties of Cr–Mo steels. *Journal of Nuclear Materials*, 187:43–54, 1992.

R. L. Klueh and J. M. Vitek. Post–irradiation tensile behavior of nickel–doped ferritic steels. *Journal of Nuclear Materials*, 150:272–280, 1987.

R. L. Klueh, M. A. Sokolov, K. Shiba, Y. Miwa, and J. P. Robertson. Embrittlement of reduced–activation ferritic/martensitic steels irradiated in HFIR at 300°C and 400°C. *Journal of Nuclear Materials*, 283–287:478–482, 2000.

R. L. Klueh and D. J. Alexander. Tensile and Charpy impact properties of irradiated reduced–activation ferritic steels. In 18. Symposium on effects of radiation on materials, pages 911–930, 1996.

R. L. Klueh, Ji-Jung Kai, and D. J. Alexander. Microstructure–mechanical properties correlation of irradiated conventional and reduced–activation martensitic steels. *Journal of Nuclear Materials*, 225:175–186, 1995.

R. L. Klueh. Irradiation hardening of ferritic steels: Effect of composition. *Journal of Nuclear Materials*, 179–181:728–732, 1991.

I. Belianov and P. Marmy. The effect of low dose irradiation on the impact fracture energy and tensile properties of pure iron and two ferritic martensitic steels. *Journal of Nuclear Materials*, 258–263:1259–1263, 1998.

M. B. Toloczko, M. L. Hamilton, and S. A. Maloy. High temperature tensile testing of modified 9Cr–1Mo after irradiation with high–energy protons. *Journal of Nuclear Materials*, 318:200–206, 2003.

A. F. Rowcliffe, J. P. Robertson, R. L. Klueh, K. Shiba, D. J. Alexander, M. L. Grossbeck, and S. Jitsukawa. Fracture toughness and tensile behavior of ferritic–martensitic steels irradiated at low temperatures. *Journal of Nuclear Materials*, 258–263:1275–1279, 1998.

J. Rensman, E. V. van Osch, M. G. Horsten, and D. S. d'Hulst. Post–irradiation mechanical tests on F82H EB and TIG welds. *Journal of Nuclear Materials*, 283–287:1201–1205, 2000.

E. Lucon and R. Chaouadi. Characterisation of the mechanical properties of Eurofer in the unirradiated and irradiated condition. Scientific Report SCK–CEN–BLG–945, Belgian Nuclear Research Centre, 2003.

H. Kurishita, H. Kayano, M. Narui, A. Kimura, M. L. Hamilton, and D. S. Gelles. Tensile properties of reduced activation Fe–9Cr–2W steels after FFTF irradiation. *Journal of Nuclear Materials*, 212–215:730–735, 1994.

K. Farrell and T. S. Byun. Tensile properties of candidate SNS target container materials after proton and neutron irradiation in the LAN–SCE accelerator. *Journal of Nuclear Materials*, 296:129–138, 2001.

Y. Dai, X. J. Jia, and K. Farrell. Mechanical properties of modified 9Cr–1Mo (T91) irradiated at $\leq\approx$300°C in SINQ Target–3. *Journal of Nuclear Materials*, 318:192–199, 2003.

J. Henry, X. Averty, Y. Dai, P. Lamagnère, J. P. Pizzanelli, J. J. Espinas, and P. Wident. Tensile properties of 9Cr–1Mo martensitic steel irradiated with high–energy protons and neutrons. *Journal of Nuclear Materials*, 187:215–227, 2003.

P. Jung, J. Henry, J. Chen, and J. C. Brachet. Effect of implanted helium on tensile properties and hardness of 9 wt% Cr martensitic stainless steels. *Journal of Nuclear Materials*, 150:241–248, 2003.

P. J. Henry, M. H. Mathon, and P. Jung. Microstructural analysis of 9 wt% Cr martensitic steels containing 0.5 at.% helium. *Journal of Nuclear Materials*, 318:249–259, 2003.

R. L. Klueh and J. M. Vitek. Fluence and helium effects on the tensile properties of ferritic steels at low temperatures. *Journal of Nuclear Materials*, 161:13–23, 1989.

H. Tanigawa, N. Hashimoto, H. Sakasegawa, R. L. Klueh, M. A. Sokolov, K. Shiba, S. Jitsukawa, and A. Kohyamay. Microstructure property analysis of HFIR–irradiated reduced–activation ferritic/martensitic steels. *Journal of Nuclear Materials*, 329–333:283–288, 2004.

D. J. Alexander, R. L. Klueh and M. Rieth. The effect of tantalum on the mechanical properties of a 9Cr–2W–0.25V–0.07Ta–0.1C steel. *Journal of Nuclear Materials*, 273:146–154, 1999.

K. W. Tupholme, D. Dulieu, and G. J. Butterworth. The development of low–activation martensitic 9 and 11Cr,W,V stainless steels for fusion reactor applications. *Journal of Nuclear Materials*, 155–157:650–655, 1988.

R. L. Klueh and J. M. Vitek. Tensile behavior of irradiated 12Cr–1MoVW steel. *Journal of Nuclear Materials*, 137(1):44–50, 1985.

H. Kayano, A. Kimura, M. Narui, T. Kikuchi, and S. Ohta. Effects of small changes in alloy composition on the mechanical properties of low activation 9%Cr–2%W. *Journal of Nuclear Materials*, 179–181:671–674, 1991.

R. L. Klueh and J. M. Vitek. Elevated–temperature tensile properties of irradiated image 2.25Cr–1Mo steel. *Journal of Nuclear Materials*, 126:9–17, 1984.

R. L. Klueh and J. M. Vitek. Elevated–temperature tensile properties of irradiated 9Cr-1MoVNb steel. *Journal of Nuclear Materials*, 132:27–31, 1985.

P. Jung, J. Henry, and J. Chen. Tensile properties of candidate structural materials for high–power spallation sources at high helium contents. *Journal of Nuclear Materials*, 343:275–284, 2005.

E. Wakai, S. Jitsukawa, H. Tomita, K. Furuya, M. Sato, K. Oka, T. Tanaka, F. Takada, T. Yamamoto, and Y. Kato. Radiation–hardening and –embrittlement due to He production in F82H steel irradiated at 250°C in JMTR. *Journal of Nuclear Materials*, 343:285–296, 2005.

R. L. Klueh, J. M. Vitek, and M. L. Grossbeck. Effect of low–temperature irradiation with (n, α) helium production on tensile properties of 12 Cr–1MoVW–type steels. *Journal of Nuclear Materials*, 104:887–891, 1981.

A. Alamo, M. Horsten, X. Averty, E. I. Materna–Morris, M. Rieth, and J. C. Brachet. Mechanical behavior of reduced–activation and conventional martensitic steels after neutron irradiation in the range 250–450°C. *Journal of Nuclear Materials*, 283–287:353–357, 2000.

R.L. Klueh, N. Hashimoto, M.A. Sokolov, P.J. Maziasz, K. Shiba, and S. Jitsukawa. Mechanical properties of neutron–irradiated nickel–containing martensitic steels: II. Review and analysis of helium–effects studies. *Journal of Nuclear Materials*, 357:169–182, 2006.

K. Farrell and T. S. Byun. Tensile properties of ferritic/martensitic steels irradiated in HFIR, and comparison with spallation irradiation data. *Journal of Nuclear Materials*, 318:274–282, 2003.

E. V. van Osch, J. van Hoepen, J. Boskeljon, and J. Rensman. Tensile properties of 2.5 dpa, 300°C: Neutron Irradiated RAFM plate, powder HIP and EB and TIG weld. Final report EBP 95–98 programme, Subtask SM 1.2.2, Nuclear Research & Consultancy Group, 2000.

Appendix B

Neural–network model of the elongation

This page details the program designed to calculate the elongation of irradiated steel, as described in Chapter 5. The program is available on the Materials Algorithms Project
(`http://www.msm.cam.ac.uk/map/mapmain.html`).

Provenance of Source Code:

Stéphane Forsik,
Phase Transformations Group,
Department of Materials Science and Metallurgy,
University of Cambridge,
Cambridge, U.K.

The neural network program was produced by:

David MacKay,
Cavendish Laboratory,
University of Cambridge,
Madingley Road,
Cambridge, CB3 0HE, U.K.

Purpose

This package allows prediction of the elongation of irradiated steels, as a function of the chemical composition, heat treatment, irradiation and test parameters.

Specification

Language: FORTRAN / C

Product form: Source code / Executable files

Operating Selntem: Linux & Windows 95/98/200/XP/Vista

Description

ELONGATION_IRRADIATED_STEEL contains a suite of programs which enable the user to estimate the elongation of irradiated steels, as a function of the chemical composition, heat treatment, irradiation and test parameters. It makes use of a neural network program called `generate44`, which was developed by David MacKay and is part of the *bigback5* program [70]. The network was trained using a large database of experimental results (Appendix A). 19 different models are provided, which differ from each other by the number of hidden units and by the value of the seed used when training the network. It was found that a more accurate result could be obtained by averaging the results from all the models [139]. This suite of programs calculates the results of each model and then combines them, by averaging, to produce a committee result and error estimate, as described by MacKay (page 387 of reference [152]). The source code for the neural network program can be downloaded from David MacKay's website [143]; the executable files only are available from MAP. Also provided are FORTRAN programs (as source code) for normalising the input data, averaging the results from the neural network program and unnormalising the final output file, along with other files necessary for running the program.

Programs are available which run on a Linux, and on a PC under Windows 95/98/2000/XP. A set of program and data files are provided for the model, which calculate the elongation of irradiated steels in NN. The files for Unix and Linux are included in a directory called NN. This directory contains the following files and subdirectories:

`README`

A text file containing step–by–step instructions for running the program, including a list of input variables.

`MINMAX`
A text file containing the minimum and maximum limits of each input and output variable. This file is used to normalise and unnormalise the input and output data.

`test.dat`
An input text file containing the input variables used for predictions.

`model.gen`
This is a unix shell file containing the command steps required to run the module. It can be executed by typing `csh model.gen` at the command prompt. This shell file compiles and runs all the programs necessary for normalising the input data, executing the network for each model, unnormalising the output data and combining the results of each model to produce the final committee result.

`RET_AUST.exe`
This executable program for the PC correspond to the unix command file `model.gen`.

`no_of_lines.ex`
This executable file reads the information of number of data from keyboard input and creates `no_of_rows.dat` file, this file is used by `spec.ex`/`spec.exe` to create `spec.t1`.

`spec.ex` / `spec.exe`
This executable file reads the information in `no_of_rows.dat` and creates a file called `spec.t1`.

`spec.t1`
A dynamic file, created by `spec.ex`/`spec.exe`, which contains information about the module and the number of data items being supplied. It is read by the program `generate44` / `generate55.exe`.

norm_test.in
This is a text file which contains the normalised input variables. It is generated by the program normtest.for in subdirectory s.

generate44 / generate55
This is the executable file for the neural network program. generate44 runs on unix selntems and generate55 on the PC. It reads the normalised input data file, norm_test.in, and uses the weight files in subdirectory c. The results are written to the temporary output file _out.

_ot, _out, _res, _sen
These files are created by generate44 and can be deleted.

Result
Contains the final un–normalised committee results for the elongation.

SUBDIRECTORY s
no_of_lines.c
The source code for program no_of_lines.ex.

spec.c
The source code for program spec.ex.

normtest.for
Program to normalise the data in test.dat and produce the normalised input file norm_test.in. It makes use of information read in from no_of_rows.dat and committee.dat.

gencom.for
This program uses the information in committee.dat and combines the predictions from the individual models, in subdirectory outprdt, to obtain an averaged value (committee prediction). The output (in normalised form) is written to com.dat.

`treatout.for`
Program to un–normalise the committee results in `com.dat` and write the output predictions to `unnorm_com`. This file is then renamed `Result`.

`committee.dat`
A text file containing the number of models to be used to form the committee result and the number of input variables. It is read by `gencom.for`, `normtest.for` and `treatout.for`.

`SUBDIRECTORY c`
`_w*f`
The weights files for the different models.

`*.lu`
Files containing information for calculating the size of the error bars for the different models.

`_c*`
Files containing information about the perceived significance value for each model.

`_R*`
Files containing values for the noise, test error and log predictive error for each model.

`SUBDIRECTORY d`
`outran.x`
A normalised output file which was created during the building of the model. It is accessed by `generate44` via `spec.t1`.

`SUBDIRECTORY outprdt`
`out1, out2` etc.
The normalised output files for each model.

`com.dat`
The normalised output file containing the committee results. It is generated by `gencom.for`.

Detailed instructions on the use of the program are given in the `README` files.

Parameters

Input parameters

The input variables for the model are listed in the `README` file. The maximum and minimum values for each variable are given in the file `MINMAX`.

Output parameters

These program gives the elongation of irradiated steels. The corresponding output files is called `Result.dat` or `Result`.

Error Indicators

None.

Accuracy

A full calculation of the error bars is presented in reference [139].

Appendix C

Neural–network model of the yield strength

This page details the program designed to calculate the yield strength of irradiated steel, as described in Chapter 6. The program is available on the Materials Algorithms Project (`http://www.msm.cam.ac.uk/map/mapmain.html`).

Provenance of Source Code:

Stéphane Forsik,
Phase Transformations Group,
Department of Materials Science and Metallurgy,
University of Cambridge,
Cambridge, U.K.

The neural network program was produced by:

David MacKay,
Cavendish Laboratory,
University of Cambridge,
Madingley Road,
Cambridge, CB3 0HE, U.K.

Purpose

This package allows prediction of the yield strength of irradiated steels, as a function of the chemical composition, heat treatment, irra-

diation and test parameters.

Specification

Language: FORTRAN / C
Product form: Source code / Executable files
Operating Selntem: Linux & Windows 95/98/200/XP/Vista

Description

YIELD_STRENGTH_IRRADIATED_STEEL contains a suite of programs which enable the user to estimate the yield strength of irradiated steels, as a function of the chemical composition, heat treatment, irradiation and test parameters. It makes use of a neural network program called `generate44`, which was developed by David MacKay and is part of the *bigback5* program [70]. The network was trained using a large database of experimental results (Appendix A). 19 different models are provided, which differ from each other by the number of hidden units and by the value of the seed used when training the network. It was found that a more accurate result could be obtained by averaging the results from all the models [139]. This suite of programs calculates the results of each model and then combines them, by averaging, to produce a committee result and error estimate, as described by MacKay (page 387 of reference [152]). The source code for the neural network program can be downloaded from David MacKay's website [143]; the executable files only are available from MAP. Also provided are FORTRAN programs (as source code) for normalising the input data, averaging the results from the neural network program and unnormalising the final output file, along with other files necessary for running the program.

Programs are available which run on a Linux, and on a PC under Windows 95/98/2000/XP. A set of program and data files are provided for the model, which calculate the yield strength of irradiated steels in NN. The files for Unix and Linux are included in a directory called NN. This directory contains the following files and subdirectories:

`README`
A text file containing step–by–step instructions for running the program, including a list of input variables.

`MINMAX`
A text file containing the minimum and maximum limits of each input and output variable. This file is used to normalise and unnormalise the input and output data.

`test.dat`
An input text file containing the input variables used for predictions.

`model.gen`
This is a unix shell file containing the command steps required to run the module. It can be executed by typing `csh model.gen` at the command prompt. This shell file compiles and runs all the programs necessary for normalising the input data, executing the network for each model, unnormalising the output data and combining the results of each model to produce the final committee result.

`RET_AUST.exe`
This executable program for the PC correspond to the unix command file `model.gen`.

`no_of_lines.ex`
This executable file reads the information of number of data from keyboard input and creates `no_of_rows.dat` file, this file is used by `spec.ex`/`spec.exe` to create `spec.t1`.

`spec.ex` / `spec.exe`
This executable file reads the information in `no_of_rows.dat` and creates a file called `spec.t1`.

`spec.t1`
A dynamic file, created by `spec.ex`/`spec.exe`, which contains infor-

mation about the module and the number of data items being supplied. It is read by the program `generate44` / `generate55.exe`.

`norm_test.in`
This is a text file which contains the normalised input variables. It is generated by the program `normtest.for` in subdirectory `s`.

`generate44` / `generate55`
This is the executable file for the neural network program. `generate44` runs on unix `selntems` and `generate55` on the PC. It reads the normalised input data file, `norm_test.in`, and uses the weight files in subdirectory `c`. The results are written to the temporary output file `_out`.

`_ot, _out, _res, _sen`
These files are created by`generate44` and can be deleted.

`Result`
Contains the final un–normalised committee results for the predicted yield strength.

`SUBDIRECTORY s`
`no_of_lines.c`
The source code for program `no_of_lines.ex`.

`spec.c`
The source code for program `spec.ex`.

`normtest.for`
Program to normalise the data in test.dat and produce the normalised input file `norm_test.in`. It makes use of information read in from `no_of_rows.dat` and `committee.dat`.

`gencom.for`
This program uses the information in `committee.dat` and combines

the predictions from the individual models, in subdirectory `outprdt`, to obtain an averaged value (committee prediction). The output (in normalised form) is written to `com.dat`.

`treatout.for`
Program to un–normalise the committee results in `com.dat` and write the output predictions to `unnorm_com`. This file is then renamed `Result`.

`committee.dat`
A text file containing the number of models to be used to form the committee result and the number of input variables. It is read by `gencom.for`, `normtest.for` and `treatout.for`.

`SUBDIRECTORY c`
`_w*f`
The weights files for the different models.

`*.lu`
Files containing information for calculating the size of the error bars for the different models.

`_c*`
Files containing information about the perceived significance value for each model.

`_R*`
Files containing values for the noise, test error and log predictive error for each model.

`SUBDIRECTORY d`
`outran.x`
A normalised output file which was created during the building of the model. It is accessed by `generate44` via `spec.t1`.

`SUBDIRECTORY outprdt`

`out1, out2` etc.
The normalised output files for each model.

`com.dat`
The normalised output file containing the committee results. It is generated by `gencom.for`.

Detailed instructions on the use of the program are given in the `README` files.

Parameters
Input parameters
The input variables for the model are listed in the `README` file. The maximum and minimum values for each variable are given in the file `MINMAX`.
Output parameters
These program gives the yield strength of irradiated steels. The corresponding output files is called `Result.dat` or `Result`.

Error Indicators
None.

Accuracy
A full calculation of the error bars is presented in reference [139].

Bibliography

[1] L. J. Perkin, B. G. Logan, M. D. Rosen, M. D. Perry, T. Diaz de la Rubia, N. M. Ghoniem, T. Ditmire, P. T. Springer, and S. C. Wilks. The investigation of high intensity laser driven micro neutron sources for fusion materials research at high fluence. *Nuclear Fusion*, 40(1):1–19, 2000.

[2] S. Konishi, S. Nishio, K. Tobita, and the DEMO design team. DEMO plant design beyond ITER. *Fusion Engineering and Design*, 63–64:11–17, 2002.

[3] I. V. Kurchatov. On the possibility of producing thermonuclear reactions in a gas discharge. *Journal of Nuclear Materials*, 4(2):193–198, 1957.

[4] M. Shimada, A. E. Costley, G. Federici, K. Ioki, A. S. Kukushkin, V. Mukhovatov, A. Polevoi, and M. Sugihara. Overview of goals and performance of ITER and strategy for plasma–wall interaction investigation. *Journal of Nuclear Materials*, 337–339:808–815, 2005.

[5] R. L. Klueh and P. J. Maziasz. Effect of irradiation in HFIR on tensile properties of Cr-Mo steels. *Journal of Nuclear Materials*, 187:43–54, 1992.

[6] Dale L. Smith, Richard F. Mattas, and Michael C. Billone. Fusion reactor materials. In Brian R.T. Frost, editor, *Materials Science and Technology*, chapter 10, pages 245–340. Wiley–VCH, 1997.

[7] ITER official website, http://www.iter.org/.

[8] Jeffrey P. Freidberg. *Plasma Physics and Fusion Energy.* Cambridge University Press, 2007.

[9] L. K. Mansur and M. L. Grossbeck. Mechanical property changes induced in structural alloys by neutron irradiations with different helium–to–displacement ratios. *Journal of Nuclear Materials*, 155–157:130–147, 1988.

[10] R. L. Klueh and J. M. Vitek. Fluence and helium effects on the tensile properties of ferritic steels at low temperatures. *Journal of Nuclear Materials*, 161:13–23, 1989.

[11] L. K. Mansur. Mechanics and kinetics of radiation effects in metals and alloys. In Gordon R. Freeman, editor, *Kinetics of nonhomogeneous processes*, chapter 8, pages 377–463. John Wiley & Sons, Inc., 1987.

[12] L. R. Greenwood. Neutron source characterization for fusion materials studies. *Journal of Nuclear Materials*, 104:797–801, 1981.

[13] E. Daum, K. Ehrlich, S. Jitsukawa, H. Matsui, and A. Möslang. The international fusion materials irradiation facility IFMIF–an overview of user aspects. *Fusion Engineering and Designn*, 49–50:435–444, 2009.

[14] T. Kondo. IFMIF, its facility concept and technology. *Journal of Nuclear Materials*, 258–263:47–55, 1998.

[15] V. Mukhovatov, M. Shimada, K. Lackner, D.J. Campbell, N.A. Uckan, J.C. Wesley, T.C. Hender, B. Lipschultz, A. Loarte, R.D. Stambaugh, R.J. Goldston, Y. Shimomura, M. Fujiwara, M. Nagami, V.D. Pustovitov, H. Zohm, ITPA CC Members, ITPA Topical Group Chairs, Co-Chairs, and the ITER International Team. Chapter 9: ITER contributions for DEMO plasma development. *Nuclear Fusion*, 47(6):S404–S413, 2007.

[16] N. Baluc, D. S. Gelles, S. Jitsukawa, A. Kimura, R. L. Klueh, G. R. Odette, B. van der Schaaf, and Jinnan Yu. Status of reduced–activation ferritic/martensitic steel development. *Journal of Nuclear Materials*, 367–370(1):33–41, 2007.

[17] K. Ehrlich, E. E. Bloom, and T. Kondo. International strategy for fusion materials development. *Journal of Nuclear Materials*, 283–287(1):79–88, 2000.

[18] L. Boccaccini, L. Giancarli, G. Janeschitz, S. Hermsmeyer, Y. Poitevin, A. Cardella, and E. Diegele. Materials and design of the european demo blankets. *Journal of Nuclear Materials*, 329-333:148–155, 2004.

[19] D. Maisonnier, I. Cook, P. Sardain, L. Boccaccini, L. Di Pace, L. Giancarli, N. Prachai, A. Pizzuto, and PPCS Team. Demo and fusion power plant conceptual studies in europe. *Fusion Engineering and Design*, 81(8–14):1123–1130, 2006.

[20] D. Maisonnier. European demo design and maintenance strategy. *Fusion Engineering and Design*, 83(7–9):858–864, 2008.

[21] E. E. Bloom, S. J. Zinkle, and F. W. Wiffen. Materials to deliver the promise of fusion power–progress and challenges. *Journal of Nuclear Materials*, 329–333(1):12–19, 2004.

[22] S. J. Zinkle and B. N. Singh. Analysis of displacement damage and defect production under cascade damage conditions. *Journal of Nuclear Materials*, 199:173–295, 1993.

[23] H. Ullmaier. The influence of helium on the bulk properties of fusion reactor structural materials. *Nuclear Fusion*, 21:1039–1083, 1984.

[24] R. L. Klueh and J. M. Vitek. *Ferritic Alloys for Use in Nuclear Energy Technologies*, page 615. The Metallurgical Society of AIME, Warrendale, Pennsylvania, 1984.

[25] A. F. Rowcliffe, J. P. Robertson, R. L. Klueh, K. Shiba, D. J. Alexander, M. L. Grossbeck, and S. Jitsukawa. Fracture toughness and tensile behavior of ferritic–martensitic steels irradiated at low temperatures. *Journal of Nuclear Materials*, 258–263:1275–1279, 1998.

[26] J. Malaplate, L. Vincent, X. Averty, J. Henry, and B. Marini. Characterization of He embrittlement of a 9Cr–1Mo steel using local approach of brittle fracture. *Engineering Fracture Mechanics*, 75(11):3570–3580, July 2008.

[27] Y. Dai, G. W. Egeland, and B. Long. Tensile properties of EC316LN irradiated in SINQ to 20 dpa. *Journal of Nuclear Materials*, 377:109–114, 2008.

[28] R. L. Klueh and D. J. Alexander. Embrittlement of 9Cr–1MoVNb and 12Cr–1MoVW steels irradiated in HFIR. *Journal of Nuclear Materials*, 187:60–69, 1992.

[29] D. S. Gelles. On quantification of helium embrittlement in ferritic/martensitic steels. *Journal of Nuclear Materials*, 283–287:838–840, 2000.

[30] R. L. Klueh, D. S. Gelles, S. Jitsukawa, A. Kimura, G. R. Odette, B. van der Schaaf, and M. Victoria. Ferritic/martensitic steels–overview of recent results. *Journal of Nuclear Materials*, 307–311(1):455–465, 2002.

[31] A. Kohyama, A. Hishinuma, D. S. Gelles, R. L. Klueh, W. Dietz, and K. Ehrlich. Low–activation ferritic and martensitic steels for fusion application. *Journal of Nuclear Materials*, 233–237:138–147, 1996.

[32] R. L. Klueh. Reduced–activation bainitic and martensitic steels for nuclear fusion applications. *Current Opinion in Solid State and Materials Science*, 8:239–250, 2004.

[33] D. S. Gelles. Development of martensitic steels for high neutron damage applications. *Journal of Nuclear Materials*, 239:99–106, 1996.

[34] G. A. Cottrell and L. J. Baker. Structural materials for fusion and spallation sources. *Journal of Nuclear Materials*, 318:260–266, 2003.

[35] R. Andreani, E. Diegele, R. Laesser, and B. van der Schaaf. The European integrated materials and technology programme in fusion. *Journal of Nuclear Materials*, 329–333:20–30, 2004.

[36] S. N. Rosenwasser, P. Miller, J. A. Dalessandro, J. M. Rawls, W. E. Toffolo, and W. Chen. The application of martensitic stainless steels in long lifetime fusion first wall/blankets. *Journal of Nuclear Materials*, 85-86:177–182, 1979.

[37] R. L. Klueh, D. J. Alexander, and E. A. Kenik. Development of low–Cr, Cr–W steels for fusion. *Journal of Nuclear Materials*, 227:11–23, 1995.

[38] A. Hishinuma, A. Kohyama, R. L. Klueh, D. S. Gelles, W. Dietz, and K. Ehrlich. Current status and future R&D for reduced–activation ferritic/martensitic steels. *Journal of Nuclear Materials*, 258–263(1):193–204, 1998.

[39] T. Muroga, M. Gasparetto, and S. J. Zinkle. Overview of materials research for fusion reactors. *Fusion Engineering and Design*, 61–62:13–25, 2002.

[40] R. L. Klueh and A. T. Nelson. Ferritic/martensitic steels for next–generation reactors. *Journal of Nuclear Materials*, 371(1–3):37–52, 2007.

[41] F. Abe, H. Araki, and T. Noda. Microstructural evolution in bainite martensite and delta–ferrite of low activation Cr–2W ferritic steels. *Materials Science and Technology*, 6:714–723, 1990.

[42] R. Laesser, N. Baluc, J.-L. Boutard, E. Diegele, S. Dudarev, M. Möslang, R. Pippan, B. Riccardi, and B. van der Schaaf. Structural materials for DEMO: The EU development, strategy, testing and modelling. *Fusion Engineering and Design*, 82(5–14):511–520, 2007.

[43] R. L. Klueh, D. S. Gelles, and T. A. Lechtenberg. Development of ferritic steels for reduced activation: the US program. *Journal of Nuclear Materials*, 141–143:1081–1087, 1986.

[44] T. Hasegawa, Y. Tomita, and A. Kohyama. Influence of tantalum and nitrogen contents, normalizing condition and TMCP process on the mechanical properties of low–activation 9Cr–2W–0.2V–Ta steels for fusion application. *Journal of Nuclear Materials*, 258–263:1153–1157, 1998.

[45] K. Shiba, R. L. Klueh, Y. Miwa, J. P. Robertson, and A. Hishinuma. Tensile behavior of F82H with and without spectral tailoring. *Journal of Nuclear Materials*, 283–287:358–361, 2000.

[46] R. L. Klueh and D. J. Alexander. Embrittlement of Cr–Mo steels after low–fluence irradiation in HFIR. *Journal of Nuclear Materials*, 218(2):151–160, 1995.

[47] Q. Huang, C. Li, Y. Li, M. Chen, M. Zhang, L. Peng, Z. Zhu, Y. Song, and S. Gao. Progress in development of China low–activation martensitic steel for fusion application. *Journal of Nuclear Materials*, 367–370:142–146, 2007.

[48] R. L. Klueh, E. T. Cheng, M. L. Grossbeck, and E. E. Bloom. Impurity effects on reduced–activation ferritic steels developed for fusion applications. *Journal of Nuclear Materials*, 280(3):353–359, 2000.

[49] A. Alamo, J. L. Bertin, V. K. Shamardin, and P. Wident. Mechanical properties of 9Cr martensitic steels and ODS–FeCr alloys after neutron irradiation at 325 °C up to 42 dpa. *Journal of Nuclear Materials*, 367–370:54–59, 2007.

[50] A. Kimura, T. Sawai, K. Shiba, A. Hishinuma, S. Jitsukawa, S. Ukai, and A. Kohyama. Recent progress in reduced–activation ferritic steels R&D in Japan. *Nuclear Fusion*, 43:1246–1249, 2003.

[51] S. A. Maloy, M. R. James, W. R. Johnson, T. S. Byun, K. Farrell, and M. B. Toloczko. Comparison of fission neutron and proton/spallation neutron irradiation effects on the tensile behaviour of type 316 and 304 stainless steel. *Journal of Nuclear Materials*, 318:283–291, 2003.

[52] A. Alamo, M. Horsten, X. Averty, E. I. Materna-Morris, M. Rieth, and J. C. Brachet. Mechanical behavior of reduced–activation and conventional martensitic steels after neutron irradiation in the range 250–450°C. *Journal of Nuclear Materials*, 283–287:353–357, 2000.

[53] E. Lucon, R. Chaouadi, and M. Decréton. Mechanical properties of the European reference RAFM steel (Eurofer'97) before and after irradiation at 300 °C. *Journal of Nuclear Materials*, 329–333:1078–1082, 2004.

[54] C. Petersen, R. Schmitt, and D. Garnier. Thermal and isothermal low cycle fatigue of MANET I and II. *Journal of Nuclear Materials*, 233-237:285–288, 1996.

[55] L. Schaefer, M. Schirra, and K. Ehrlich. Mechanical properties of low–activating martensitic 8–10% CrWVTa steels of type OPTIFER. *Journal of Nuclear Materials*, 233–237:264–269, 1996.

[56] S. Jitsukawa, M. Tamura, B. van der Schaaf, R. L. Klueh, A. Alamo, C. Petersen, M. Schirra, P. Spaetig, G. R. Odette, A. A. Tavassoli, K. Shiba, A. Kohyama, and A. Kimura. Development of an extensive database of mechanical and physical properties for reduced–activation martensitic steel F82H. *Journal of Nuclear Materials*, 307–311:179–186, 2002.

[57] K. Farrell and T. S. Byun. Tensile properties of ferritic/martensitic steels irradiated in HFIR, and comparison with spallation irradiation data. *Journal of Nuclear Materials*, 318:274–282, 2003.

[58] A. Kimura, T. Morimura, M. Narui, and H. Matsui. Irradiation hardening of reduced–activation martensitic steels. *Journal of Nuclear Materials*, 233–237:319–325, 1996.

[59] H. K. D. H. Bhadeshia. Neural networks in materials science. *ISIJ International*, 39:966–979, 1999.

[60] S. H. Nam and S. V. Oh. Real–time dynamic visual tracking using PSD sensors and extended trapezoidal motion planning. *Applied Intelligence*, 10:53–70, 1999.

[61] S. Chatterjee, M. Murugananth, and H. K. D. H. Bhadeshia. δ–TRIP steel. *Materials Science and Technology*, 23:819–827, 2007.

[62] J. Kocijan. Gaussian process models for systems identification. In Matej Gasperin and Bostjan Pregelj, editors, *Proceedings of the 9th International PhD Workshop on Systems and Control*, 2008.

[63] C. A. L. Bailer-Jones, T. J. Sabin, D. J. C. MacKay, and P. J. Withers. Prediction of deformed and annealed microstructures using Bayesian neural networks and Gaussian processes. In T. Chandra, S. R. Leclair, J. A. Meech, B. Verma, M. Smith, and B. Balachandran, editors, *Proceedings of the Australasia Pacific Forum on Intelligent Processing and Manufacturing of Materials*, 1997.

[64] C. A. L. Bailer-Jones, H. K. D. H. Bhadeshia, and D. J. C. MacKay. Gaussian process modelling of austenite formation in steel. *Materials Science and Technology*, 15:287–294, 1999.

[65] T. J. Sabin, S. M. Roberts C. A. L. Bailer-Jones, D. J. C. MacKay, and P. J. Withers. Gaussian process modelling of the evolution of microstructure in cold–worked aluminium–magnesium alloys. In T. Chandra and T. Sakai, editors, *Proceedings of the International Conference on Thermomechanical Processing*, volume 1, page 1043, Pennsylvania, PA, 1997. The Minerals, Metals and Materials Society.

[66] T. J. Sabin, C. A. L. Bailer-Jones, and P. J. Withers. Accelerated learning using Gaussian process models to predict static recrystalisation in an Al–Mg alloy. *Modelling and Simulation in Materials Science and Engineering*, 8:687–706, 2000.

[67] C. Capdevila, F. G. Caballero, and C. Garcia de Andrés. Predic-

tion of martensite start temperature by neural–network analysis. *Journal de Physique IV*, 112:217–221, 2003.

[68] D. J. C. MacKay. A practical Bayesian framework for backpropagation networks. *Neural Computation*, 4(3):448–472, 1992.

[69] D. J. C. MacKay. Bayesian interpolation. *Neural Computation*, 4:415–447, 1992.

[70] D. J. C. MacKay, Materials Algorithms Project Program Library. http://www.msm.cam.ac.uk/map/utilities/modules/nnecode.html.

[71] H. R. Maier and G. C. Dandy. Neural networks for the prediction and forecasting of water resources variables: a review of modelling issues and applications. *Environmental Modelling and Software*, 15:101–124, 2000.

[72] M. W. Gardner and S. R. Dorling. Artificial neural networks (the multilayer perceptron)–a review of applications in the atmospheric sciences. *Atmospheric Environment*, 32(14–15):2627–2636, 2000.

[73] H. Adeli. Neural networks in civil engineering: 1989–2000. *Computer-aided civil and infrastructure engineering*, 16:126–142, 2001.

[74] A. B. Bulasari. Applications of neural networks in process engineering. *Journal of Systems Engineering*, 4:131–170, 1994.

[75] R. D. Vanluchene and R. Sun. Neural networks in structural engineering. *Microcomputers in Civil Engineering*, 5:207–215, 1990.

[76] H. K. D. H. Bhadeshia. Neural networks and information in materials science. *Statistical Analysis and Data Mining*, 1(5):296–305, 2008.

[77] H. K. D. H. Bhadeshia, R. C. Dimitriu, S. Forsik, J. H. Pak, and J. H. Ryu. On performance of neural networks in materials science. *Materials Science and Technology*, 25(4):504–510, 2009.

[78] D. Rodney. Atomic modeling of irradiation–induced hardening. *Comptes Rendus Physique*, 9(3–4):418–426, 2008.

[79] L. Gámez, E. Martinez, J. M. Perlado, P. Cepas, M. J. Caturla, M. Victoria, J. Marian, C. Arévalo, M. Hernandez, and D. Gomez. Kinetic Monte Carlo modelling of neutron irradiation damage in iron. *Fusion Engineering and Design*, 82(15–24):2666–2670, 2007.

[80] L. Malerba, A. Caro, and J. Wallenius. Multiscale modelling of radiation damage and phase transformations: The challenge of FeCr alloys. *Journal of Nuclear Materials*, 382:112–125, 2008.

[81] M. J. Makin and F. J. Minter. Irradiation hardening in copper and nickel. *Acta Metallurgica*, 8:691–699, 1960.

[82] T. S. Byun and K. Farrell. Irradiation hardening behavior of polycrystalline metals after low–temperature irradiation. *Journal of Nuclear Materials*, 326:86–96, 2004.

[83] R. Kemp, G. A. Cottrell, H. K. D. H. Bhadeshia, G. R. Odette, T. Yamamoto, and H. Kishimoto. Neural–network analysis of irradiation hardening in low–activation steels. *Journal of Nuclear Materials*, 348:311–328, 2006.

[84] G. A. Cottrell, R. Kemp, H. K. D. H. Bhadeshia, G. R. Odette, and T. Yamamoto. Neural network analysis of Charpy transition temperature of irradiated low–activation martensitic steels. *Journal of Nuclear Materials*, 367–370:603–609, 2007.

[85] C. E. Rasmussen and C. K. I. Williams. *Gaussian Processes for Machine Learning*. MIT Press, 2006.

[86] M. N. Gibbs. *Bayesian Gaussian Processes for Regression and Classication*. PhD thesis, University of Cambridge, 1998.

[87] N. Cressie. Statistics for spacial data. *Terra Nova*, 4(5):613–617, 1992.

[88] C. K. I. Williams and C. E. Rasmussen. Gaussian processes for regression. In *Advances in Neural Information Processing Systems 8*, 1996.

[89] M. N. Gibbs and D. J. C. MacKay. Efficient implementation of Gaussian processes. Technical report, 1997.

[90] Y. Kojchi, I. Hiroshi, T. Hideo, Y. Masayoshi, K. Osamu, K. Kiyoshi, and K. Kazuhio. NRIM data sheets 1b, 3b, 8b, 11b, 12b, 17b, 18b, 19b, 20b, 21b. Technical report, National Research Institute for Metals, Tokyo, Japan, 1994.

[91] E. Wakai, M. Ando, T. Sawai, H. Tanigawa, T. Taguchi, R.E. Stoller, T. Yamamoto, Y. Kato, and F. Takada. Effect of heat treatments on tensile properties of F82H steel irradiated by neutrons. *Journal of Nuclear Materials*, 367–370(1):74–80, 2007.

[92] H.K.D.H. Bhadeshia. Design of ferritic creep–resistant steels. *ISIJ International*, 41(6):626–640, 1999.

[93] R.L. Klueh, N. Hashimoto, M.A. Sokolov, P.J. Maziasz, K. Shiba, and S. Jitsukawa. Mechanical properties of neutron–irradiated nickel–containing martensitic steels: II. Review and analysis of helium–effects studies. *Journal of Nuclear Materials*, 357:169–182, 2006.

[94] H. K. D. H. Bhadeshia and R. W. K. Honeycombe. *Steels: Microstructure and Properties, 3rd edition.* Butterworth–Heinemann, London, 2006.

[95] J. Fridberg, L. E. Torndähl, and M. Hillert. Diffusion in iron. *Jernkontorets Annaler*, 153:263–276, 1969.

[96] J. W. Christian. *Theory of Transformations in Metal and Alloys, Part I.* Pergamon Press, Oxford, U. K., 3 edition, 2003.

[97] Miguel Angel Yescas Gonzalez. *Modelling the Properties of Austempered Ductile Cast Iron.* PhD thesis, University of Cambridge, 2001.

[98] P. Jung, C. Liu, and J. Chen. Retention of implanted hydrogen and helium in martensitic stainless steels and their effects on mechanical properties. *Journal of Nuclear Materials*, 296:165–173, 2001.

[99] M. Yescas, H. K. D. H. Bhadeshia, and D. J. C. MacKay. Estimation of the amount of retained austenite in austempered ductile irons using neural networks. *Materials Science & Engineering A*, 311(1–2):162–173, 2001.

[100] M. Avrami. Kinetics of phase change 1. *Journal of Chemical Physics*, 7:1103–1112, 1939.

[101] M. Avrami. Kinetics of phase change 2. *Journal of Chemical Physics*, 8:212–224, 1940.

[102] M. Avrami. Kinetics of phase change 3. *Journal of Chemical Physics*, 9:177–184, 1941.

[103] T. Sourmail, H. K. D. H. Bhadeshia, and D. J. C. MacKay. Neural network model of creep strength of austenitic stainless steels. *Materials Science and Technology*, 18:655–663, 2002.

[104] N. Hashimoto, S. J. Zinkle, A. F. Rowcliffe, J. P. Robertson, and S. Jitsukawa. Deformation mechanisms in 316 stainless steel irradiated at 60 °C and 330 °C. *Journal of Nuclear Materials*, 283–287:528–534, 2000.

[105] T. H. Blewitt, R. R. Coltman, R. E. Jamison, and J. K. Redman. Radiation hardening of copper single crystals. *Journal of Nuclear Materials*, 2(4):277–298, 1960.

[106] D. K. Holmes. Solid State Division Annual Progress Report, ORNL-2413, November 1957.

[107] *Proceeding of the 2nd International Conference on Peaceful Uses of Atomic Energy*, 1958.

[108] A. A. B. Sugden and H. K. D. H. Bhadeshia. The estimation of non–uniform elongation in low–alloy steel weld deposits. *Journal of Materials Science*, 25(1):613–618, 1990.

[109] E. A. Metzbower, J. J. DeLoach, S. H. Lalam, and H. K. D. H. Bhadeshia. Neural–network analysis of strength and ductility of welding alloys for high–strength low–alloy shipbuilding steels. *Science and Technology of Welding*, 6:116–121, 2001.

[110] H. K. D. H. Bhadeshia. Design of ferritic creep–resistant steels. *ISIJ International*, 41:621–640, 2001.

[111] R. C. Dimitriu and H. K. D. H. Bhadeshia. Hot–strength of creep–resistant ferritic steels and relationship to creep–rupture data. *Materials Science and Technology*, 23(9):1127–1131, 2007.

[112] R. S. Nelson, J. A. Hudson, and D. J. Mazey. The stability of precipitates in an irradiation environment. *Journal of Nuclear Materials*, 44(3):318–330, 1972.

[113] T. Morimura, A. Kimura, and H. Matsui. Void swelling of Japanese candidate martensitic steels under FFTF/MOTA irradiation. *Journal of Nuclear Materials*, 239:118–125, 1996.

[114] R. L. Klueh. Heat treatment behaviour and tensile properties of Cr–W steels. *Metallurgical and Materials Transactions A*, 20(3):463–470, 1989.

[115] E. Lucon and R. Chaouadi. Characterisation of the mechanical properties of EUROFER in the unirradiated and irradiated condition. Scientific Report SCK-CEN-BLG-945, Belgian Nuclear Research Centre, 2003.

[116] Richard Kemp. *Alloy Design for a Fusion Power Plant*. PhD thesis, University of Cambridge, 2006.

[117] R. Kemp, G.A. Cottrell, and H.K.D.H. Bhadeshia. Designing optimised experiments for the international fusion materials irradiation facility. *Journal of Nuclear Materials*, 367-370(2):1586–1589, 2007.

[118] A. A. B. Sugden and H. K. D. H. Bhadeshia. A model for the strength of the as–deposited regions of steel weld metals. *Metallurgical Transactions A*, 19A(6):1597–1602, 1988.

[119] M. B. Toloczko, M. L. Hamilton, and S. A. Maloy. High–temperature tensile testing of modified 9Cr–1Mo after irradiation with high–energy protons. *Journal of Nuclear Materials*, 318:200–206, 2003.

[120] N. Bailey and R. J. Pargeter. Weld. inst. res. rep. 70/1978/m. Technical report, The Welding Institute, Abington, UK, 1978.

[121] I. G. Bosward and R. John. In UK The Welding Institute, Abington, editor, *Trends in Steel and Consumables for Welding*, pages 135–150, 1979.

[122] G. M. Evans. Effect of welding position on the microstructure and properties. Technical Report IIW Doc. II A 529 81, International Institute of Welding, 1981.

[123] A. Sugden. *Towards the Prediction of Weld Metal Properties*. PhD thesis, University of Cambridge, 1988.

[124] W. C. Leslie. Iron and its dilute substitutional solid solutions. *Metallurgical and Materials Transactions B*, 3(1):5–26, 1972.

[125] MTData: Metallurgical and Thermochemical Databank. Teddington, UK: National Physical Laboratory; 1995. http://www.npl.co.uk/mtdata/.

[126] D. Kalish, S. A. Kulin, and M. Cohen. Bainitic structures and thermomechanical treatments applied to steel. *Journal of Metals*, 17:157–164, 1965.

[127] H. K. D. H. Bhadeshia and A. R. Waugh. Bainite: An atom probe study of the incomplete reaction phenomenon. *Acta Metallurgica*, 30:775–784, 1982.

[128] M. Peet, S. S. Babu, M. K. Miller, and H. K. D. H. Bhadeshia. Three–dimensional atom probe analysis of carbon distribution in low–temperature bainite. *Scripta Materialia*, 50:1277–1281, 2004.

[129] F. G. Caballero, M. K. Miller, S. S. Babu, and C. Garcia-Mateo. Atomic scale observations of bainite transformation in a high carbon high silicon steel. *Acta Materialia*, 55:381–390, 2007.

[130] NAG Fortran Library, Numerical Algorithms Group Ltd, Oxford, U.K.
http://www.nag.co.uk.

[131] R. L. Klueh, K. Ehrlich, and F. Abe. Ferritic/martensitic steels: promises and problems. *Journal of Nuclear Materials*, 191-194:116–124, 1992.

[132] R. L. Klueh, P. J. Maziasz, and J. M. Vitek. Postirradiation tensile behavior of nickel–doped ferritic steels. *Journal of Nuclear Materials*, 141–143:960–965, 1986.

[133] R. L. Klueh and J. M. Vitek. Elevated-temperature tensile properties of irradiated image 2.25Cr-1Mo steel. *Journal of Nuclear Materials*, 126:9–17, 1984.

[134] R. Kasada, A. Kimura, H. Matsui, M. Hasegawa, and M. Narui. Effects of varying temperature irradiation on the neutron irradiation hardening of reduced–activation 9Cr–2W martensitic steels. *Journal of Nuclear Materials*, 271–272:360–364, 1999.

[135] M. I. Luppo, C. Bailat, R. Schäubline, and M. Victoria. Tensile properties and microstructure of 590 MeV proton–irradiated pure Fe and a Fe–Cr alloy. *Journal of Nuclear Materials*, 283–287:483–487, 2000.

[136] Y. Dai, S. A. Maloy, G. S. Bauer, and W. F. Sommer. Mechanical properties and microstructure in low–activation martensitic steels F82H and Optimax after 800–MeV proton irradiation. *Journal of Nuclear Materials*, 283–287:513–517, 2000.

[137] J. Saito, T. Suda, S. Yamashita, S. Ohnuki, H. Takahashi, N. Akasaka, M. Nishida, and S. Ukai. Void formation and microstructural development in oxide dispersion strengthened ferritic steels during electron–irradiation. *Journal of Nuclear Materials*, 258–263:1264–1268, 1998.

[138] I. Belianov and P. Marmy. The effect of low dose irradiation on the impact fracture energy and tensile properties of pure iron and two ferritic martensitic steels. *Journal of Nuclear Materials*, 258–263:1259–1263, 1998.

[139] S. Forsik and H.K.D.H. Bhadeshia. Elongation of irradiated steels. *Material and Manufacturing Processes*, 24(2):1–8, 2009.

[140] A. Kimura and H. Matsui. Neutron irradiation effects on the microstructure of low–activation ferritic alloy. *Journal of Nuclear Materials*, 212–215:701–706, 1994.

[141] R. C. Dimitriu, H. K. D. H. Bhadeshia, C. Fillon, and C. Poloni. Strength of ferritic steels: Neural networks and genetic programming. *Materials and Manufacturing Processes*, 24(1):10–15, 2009.

[142] F. Tancret, H. K. D. H. Bhadeshia, and D. J. C. MacKay. Comparison of artificial neural networks with Gaussian processes to model the yield strength of nickel–base superalloys. *ISIJ International*, 39:1020–1026, 1999.

[143] D. J. C. MacKay, Professor of Natural Philosophy, Department of Physics, Cavendish Laboratory, University of Cambridge http://www.inference.phy.cam.ac.uk/mackay/.

[144] MATLAB, The MathWorks, Inc. http://www.mathworks.com.

[145] Colin G Windsor, Geoff Cottrell, and Richard Kemp. Prediction of yield stress in highly irradiated ferritic steels. *Modelling and Simulation in Materials Science and Engineering*, 16, 2008.

[146] C. Windsor, G. Cottrell, and R. Kemp. Prediction of the Charpy transition temperature in highly irradiated ferritic steels. *Modelling and Simulation in Materials Science and Engineering*, 16, 2008.

[147] Rajesh Mehta, Satyam S. Sahay, Amlan Datta, and Aman Chodha. Neural network models for industrial batch annealing

operation. *Materials and Manufacturing Processes*, 23(2):203–208, 2008.

[148] Thomas Sourmail. Model Manager, Neuromat ltd. http://www.neuromat.com/model_manager.html.

[149] E. Wakai, S. Jitsukawa, H. Tomita, K. Furuya, M. Sato, K. Oka, T. Tanaka, F. Takada, T. Yamamoto, Y. Kato, Y. Tayama, K. Shiba, and S. Ohnuki. Radiation hardening and embrittlement due to He production in F82H steel irradiated at 250 °C in JMTR. *Journal of Nuclear Materials*, 343(1–3):285–296, 2005.

[150] S. Mandal, P. V. Sivaprasad, S. Venugopal, and K. P. N. Murthy. Constitutive flow behaviour of austenitic stainless steels under hot deformation: artificial neural network modelling to understand, evaluate and predict. *Modelling and Simulation in Materials Science and Engineering*, 14:1053–1070, 2006.

[151] M. J. Peet, H. S. Salman, and H. K. D. H. Bhadeshia. Prediction of thermal conductivity of steel. *In Preparation.*

[152] D. J. C. MacKay. Bayesian non-linear modelling with neural networks. In H. Cerjak and H. K. D. H. Bhadeshia, editors, *Mathematical Modelling of Weld Phenomena 3*, pages 359–389. The Institute of Materials, London, 1997.